Density Functional Calculations of Magnesium-Amide
-a cluster approach

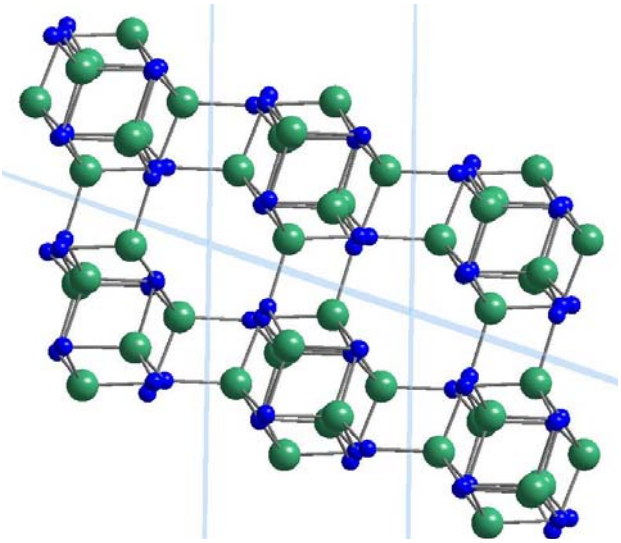

Thorleif A. Tollefsen Seip

Center for Materials Science and Nanotechnology
Department of Physics, University of Oslo

May 2008

Thesis presented for the degree of Master of Science

Preface

The work on this thesis started in the spring of 2007 at the Center for Materials Science and Nanotechnology at the University of Oslo. The autumn of 2007 was spent at Leiden University, before the work was finished in the spring of 2008 in Oslo. All the density functional theory calculations were performed at the Norwegian Metacenter for Computational Science.

First and foremost I would like to thank my supervisor, Dr. Ole Martin Løvvik, for excellent supervision and enthusiasm during the course of the whole project. His encouragement, advice and exceptional promptness in responding to my questions has been invaluable during the work. I am also deeply grateful for the scientific input and general support of Dr. Roar A. Olsen, my supervisor during the stay at Leiden University. Our many and long discussions helped immensely in making my stay a valuable and pleasant one.

I would also like to thank my fellow students at the University of Oslo and the members of the group for theoretical chemistry at Leiden University for helpful input and support. Last but not least, I would like to thank my wife, Ingri, and my daughters, Sara, Tale and Noor, for being who they are.

Thorleif A. Tollefsen Seip
May 2008

Summary

If a future hydrogen society is to be established, a highly efficient solid-state hydrogen storage material must be found. The metal-N-H system, which is one of the new promising candidates, has been given considerable attention after Chen et al.[1] in 2002 found that lithium-nitride reversibly absorbs a large amount of hydrogen and form a mixture of lithium-hydride and lithium-amide. This thesis presents density functional theory calculations performed on $Mg(NH_2)_2$ (magnesium-amide).

$Mg(NH_2)_2$ is confirmed having a tetragonal unit cell which belongs to the space group $I4_1/acd$. The cations in $Mg(NH_2)_2$ (i.e. Mg^{2+}) are tetrahedrally coordinated by the anions (i.e. NH_2^-) and the MgN_4 tetrahedra share all four corners with other MgN_4 tetrahedra, thus forming an open, three dimensional network. Furthermore, the crystal structure was found to be organized in weakly connected branches, where the branches point in the $[1\bar{1}0]$ or the $[\bar{1}10]$ directions, and where each branch is separated from the other branches by planes in the (112) and $(11\bar{2})$ orientations.

Density of states calculations showed that $Mg(NH_2)_2$ is an insulator with a GGA band gap of approximately 3.1 eV. The bonds within the anions (N-H) are primarily covalent, while ionic Mg-N bonds hold $Mg(NH_2)_2$ together.

Six different surfaces and their corresponding surface energies have been calculated. The (110) surface proved to have the lowest surface energy, closely followed by the (012) and (112) surfaces. However, special symmetry properties and small structural changes during ionic relaxation of the (112) slab, indicates that the corresponding surface may be even more frequently found in a real crystal, despite the slightly higher surface energy compared to the (110) surface.

The first reported cluster calculations on complex hydrides in a plane wave code are to our knowledge included in the thesis. A combination of bulk, slab and cluster calculations provided new and important insights about $Mg(NH_2)_2$. Comparison of the density of states calculated from bulk, slab and cluster showed that occupied states in the band gap probably are one of the main reasons for why complex hydrides with nano-particle structure have better kinetics than complex hydrides with larger particles (in addition to the increased surface area).

Calculations of the activation energy involved in the removal of NH_3 and H_2 showed that it is energetically easier to remove NH_3 than H_2 from $Mg(NH_2)_2$, confirming a general trend for metal-N-H systems.

Contents

Chapter 1

1 Introduction

This chapter will first say something about the background for why the development of a new energy system is so important in today's society. Then some of the most important renewable energy resources, and the technologies involved in harvesting the energy delivered from them in a useful way will be presented. The main part of the chapter will be about hydrogen storage systems, with the main focus on metal-N-H systems, a new and very promising group of complex hydrides.

1.1 Global warming

During the last century the average global air temperature near the Earth`s surface has increased by approximately 0.74 ˚C [2] (see figure 1.1). This temperature increase is called global warming. There is no complete agreement among scientist on what causes global warming, but the Intergovernmental Panel on Climate Chang (IPCC) have concluded that *"most of the observed increase in globally averaged temperatures since the mid-20th century is very likely due to the observed increase in anthropogenic greenhouse gas concentrations"*[2]. This means that there is an increased greenhouse effect, i.e. the process in

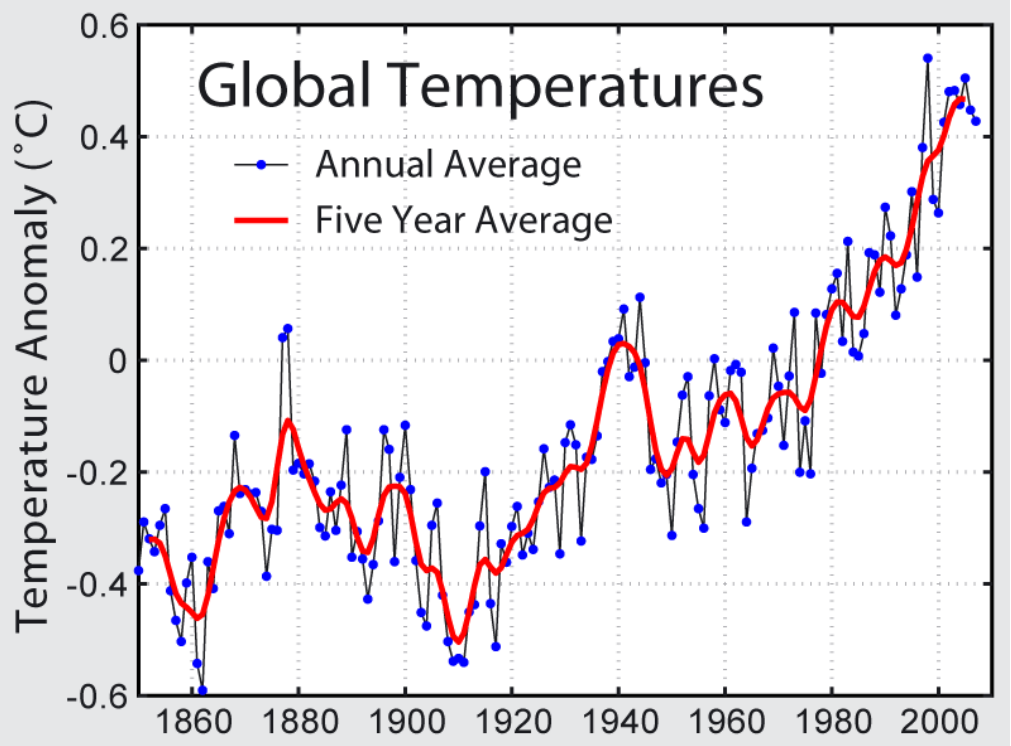

Figure 1.1: Global average air temperatures for the last 150 years[3].

which the emission of infrared radiation by the atmosphere warms a planet's surface. Furthermore, IPCC predicts that the global surface temperature will increase by 1.1 to 6.4 ˚C between 1990 and 2100[2] which clearly will lead to major changes on earth, including: sea level rise, increased intensity of extreme weather events, glacier retreat, change in agricultural yields and species extinctions. All of these changes would be serious enough alone, and if they all come at the same time, it can lead to dramatic changes to life on earth.

The major greenhouse gases on Earth are water vapor, carbon dioxide (CO_2), methane (CH_4) and ozone. The atmospheric concentration of CO_2, the greenhouse gas which contributes most to global warming[4], has increased by 31% since 1750[5]. Figure 1.2 shows the variations in concentration of CO_2 in the atmosphere during the last 4000 years as measured from ice cores. Throughout most of the record, the large changes can be related to glacial/interglacial cycles within the current ice age[3]. However, since the beginning of the industrial revolution (around 1800), burning of fossil fuels has caused a dramatic increase of CO_2 in the atmosphere, reaching levels that probably are unprecented in the last 20 million years[6]. And given that our main energy supply comes from burning of fossil fuels, the CO_2 level is expected to increase further and thereby accelerate global warming. To decelerate this process, and hopefully prevent further irreversible damage to on the environment, we must

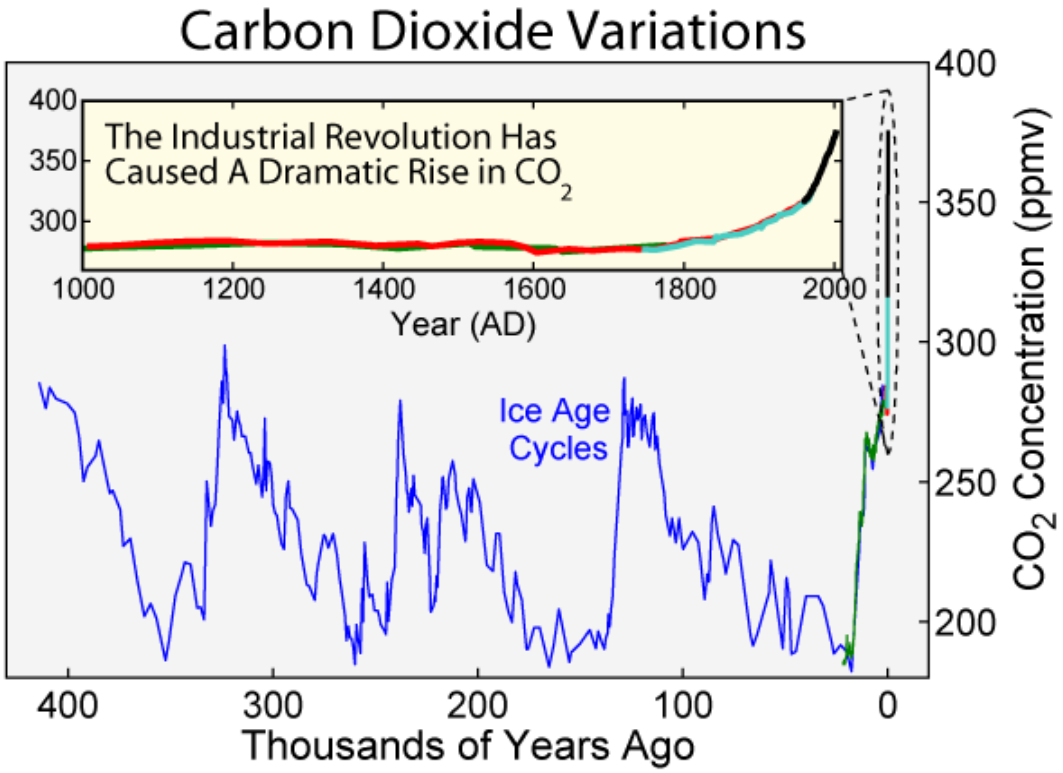

Figure 1.2: The variation in concentration of CO_2 in the atmosphere during the last 4000 years as measured from ice cores[3].

develop new solutions for both energy consumption and supply. In principle there are three different approaches to alleviating these problems, namely[7]:

(i) Preventing the cause of global warming from escaping into the atmosphere (i.e. CO_2 sequestration), known as the 'clean fossil hydrogen' option;
(ii) a drastic efficiency increase in energy usage;

(iii) a transition from fossil fuels to sustainable, CO_2 neutral ones.

The "clean fossil hydrogen" option can only be realized by separating, removing and storing the carbon or the CO_2 extracted from the reformed primary fuel. The secondary hydrogen energy carrier can then be used in highly efficient conversion units; hydrogen obtained in this way can be seen as a bridge to the last, sustainable option (iii)[7]. The second alternative, an increase in energy efficiency, has been facilitated enormously by new technology developed over the last few decades. Examples include better construction materials and insulating foams for houses; multipane windows, high efficiency heating systems, combined heat and power stations, more efficient engines, motor oils with better lubricity and lower viscosity, better fuels, more aerodynamic shapes of automobiles, larger aeroplanes, better turbines etc.[7]. However, part of the progress made has not been translated into a reduction of energy usage but rather into an increase in consumer comfort. The last option, namely, the transition from the present fossil fuel era into a renewable and sustainable future energy world, is the ultimate one[7]. The central idea is that all the energy will be produced from renewable and "clean" energy resources.

1.2 Renewable energy resources

There are many renewable energy resources, and common for the majority of them are that they are directly or indirectly powered by the sun. This means that they are constantly replenished and never will run out. In this section a short introduction to some of the most common renewable energy resources and technologies will be presented, namely, direct solar energy, biomass energy, wind energy and hydropower, where the last three have their origin from indirect solar energy.

1.2.1 Direct Solar Energy

Heat and light from the sun provides an abundant source of energy that can be harnessed in many ways. There are many technologies developed to take advantage of direct solar energy, and some of the most important ones are solar collector systems and photovoltaic systems.

A solar collector is a device that converts solar radiation energy into heat in a useful form. The solar collector captures the sun's radiation over a large area and focuses it into a small area. There are three principal types; flat plate collector, which is feasible for low and moderate temperatures (less than 100 ˚C); single focusing collectors and double focusing collectors, which both are suitable for providing high temperatures. The main application of the first collector is heating of hot water in residential buildings. The two last collectors, which supply very high temperatures, can be used to generate steam or to start chemical reactions to produce a portable fuel such as hydrogen[8].

A photovoltaic cell, or solar cell, converts solar radiation energy directly into electrical energy. The solar cell is made of a thin semiconductor wafer, usually silicon, which is specially treated to form an electric field, positive on one side and negative on the other. The positive side contains positively charged holes (missing electrons), while the negative side have extra electrons. When the positive and negative semiconductors are brought together, a junction is created. This junction will produce a movement of electrons when solar radiation strikes the solar cell. If electrical conductors are attached to the positive and negative sides,

forming an electrical circuit, electricity is generated from the solar cell. This electricity can then be used for many supposes, examples include lighting of residential and business buildings.

These kinds of technologies have been used for decades, and there still is intensive research in the further development of the devices. The main obstacle with direct solar energy is the intensity variation with time. Seasonal, daily and weather variations make solar radiation a difficult all-energy solution. However, this variation decreases substantially with the latitude. So if new methods for solar energy storage are developed, the energy can be harvested in e.g. large solar collector plants located in low latitude regions, stored and then transported to regions where it is needed. This means that direct solar energy has the potential of being one of the major energy resources in a future sustainable energy system.

1.2.2 Biomass energy

Biomass energy or “bioenergy” has been used for centuries. Bioenergy is obtained when biomass, i.e. the organic matter of plants, is used to produce electricity, fuels, chemicals, heat, etc. The main benefit of the use of bioenergy is that it has the potential to greatly reduce greenhouse gas emissions[9]. Burning biomass releases about the same amount of CO_2 as burning fossil fuels[9]. But, while fossil fuels release CO_2 captured by photosynthesis millions of years ago (an essentially "new" greenhouse gas), biomass releases carbon dioxide that is largely balanced by the carbon dioxide captured in its own growth (depending on how much energy was used to grow, harvest, and produce the fuel). The CO_2 release from biomass burning is thus favorable[9].

Bioenergy is already used as fuel for transport. More and more car manufactures are producing cars that can use ethanol (made from corn) or biodiesel (made from soybeans) as fuel. This can clearly help reduce the growth of the manmade CO_2 emission, but also some new problems are introduced; agriculture land is needed in the production of biofuel. This reduces the amount of available agricultural land for food production and as a result the food prices increase. The consequences of this can already be observed in the developing countries, where the increased food price has put many people into even deeper poverty. In figure 1.3 a “humoristic” biofuel-cartoon which casts light on the problem is shown.

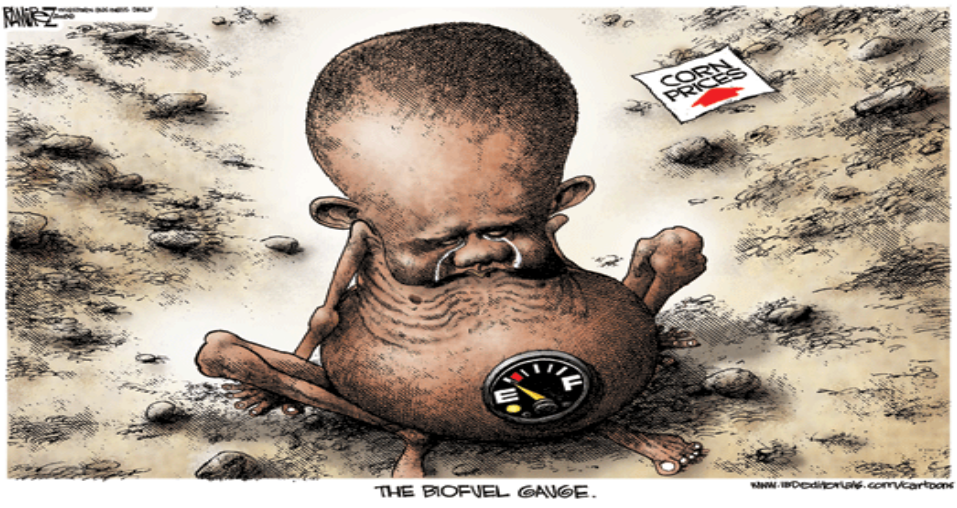

Figure 1.3: A “humoristic” biofuel-cartoon enlightening problems connected to bioenergy[10].

1.2.3 Wind Energy

Wind energy has been used for centuries. In old Holland windmills were used for pumping water or grinding grain. Today we use modern wind turbines which use wind energy to generate electricity. Wind turbines can be used as stand-alone applications, or they can be connected to a utility power grid or even combined with a photovoltaic cell[9]. For stand-alone applications of wind turbines, the energy is often used for water pumping or communication[9]. It is also popular among homeowners and farmers, who live in windy areas, to use them for generating electricity. In utility-scale sources of wind energy, a large number of wind turbines are usually built together, forming a wind plant. This is common among several electricity providers, also in Norway.

The use of a large number of wind turbines around the world will obviously reduce the manmade CO_2 emission, but also some negative environmental issues are involved. One is that the wind turbines have a massive impact on the landscape where they are located. Another is that white-tailed eagles who live in areas with wind turbines often fly into their propeller like blades and become badly injured, often resulting in death. This is clearly a problem with an already endangered animal species.

1.2.4 Hydropower

In Norway we are blessed with hydropower. This is one of the oldest sources of energy and was used thousands of years ago to turn paddle wheels for purposes such as grinding grain. Hydropower exploits the energy from solar radiation that heats water on the ocean surfaces, causing it to evaporate. This water vapor condenses into clouds and then falls back onto the surface in different altitudes. The water above sea level flows back into the oceans through rivers. By making dams to store the water, it is possible to store and control this energy. When energy is needed water is released and electricity can be generated.

Hydropower is a very “good” energy resource since it is a renewable, “clean” energy system with built in storage possibilities. In the U.S. it accounted for 7% of the total electricity generation in 2005[11]. However, there are limited possibilities for building new hydropower plants, since they only can be built in certain landscapes (preferably a region with a natural lake and a connecting water fall). An additional aspect with hydropower plants is that they have massive impact on the surrounding nature, making rivers partly dry, leading to damages on wild life. Nevertheless, there certainly are good arguments for including hydropower in a new sustainable and renewable energy system also.

1.3 Future energy system

A future sustainable energy system will most likely harvest energy from several resources, including those discussed in the last sections. Independent of which of these resources that mainly will be used, a key ingredient is storage of energy. At present, energy buffering is mainly provided by fossil fuel-generated electricity. This is not possible when renewable sources represent more than 30% of the total energy resources[7]. It is therefore necessary to look for new energy carriers. In this context hydrogen is one of the most attractive candidates, since it can be integrated in a clean hydrogen-water-hydrogen closed material loop, and it

offers interesting storage and distribution possibilities[7]. It can also be linked to the other clean energy carrier, electricity, through electrolysis and fuel cells.

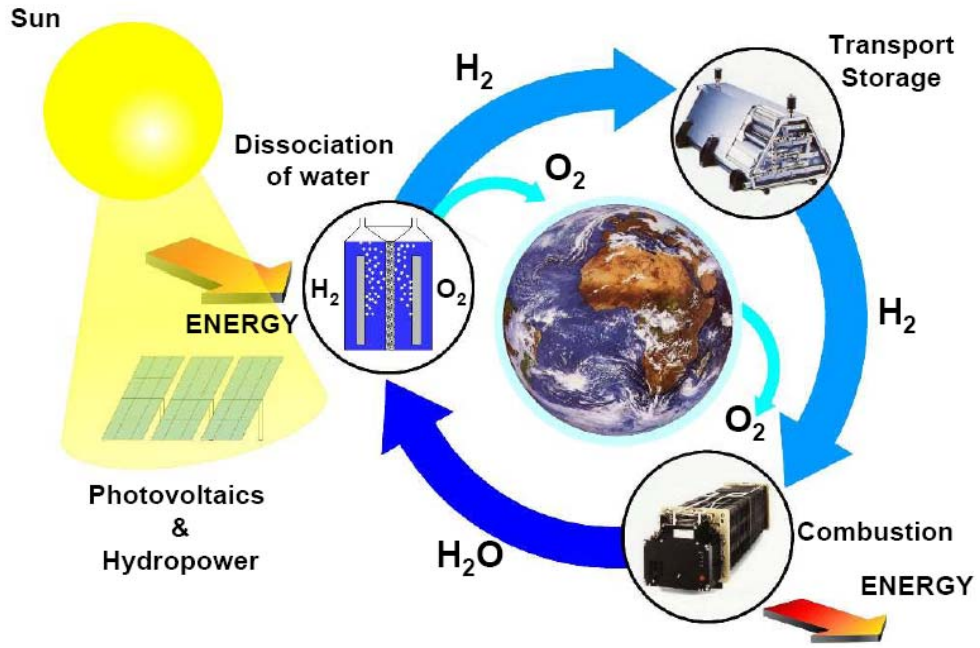

Figure 1.3: An energy system based on hydrogen as an energy carrier[12]

Figure 1.3 shows schematically an energy system based on hydrogen as an energy carrier. It consists of the following parts:

- Solar cells, hydropower, wind turbines and other renewable energy sources are used in production of electricity.
- This electricity is used in electrolysis through splitting of water to produce hydrogen (and oxygen).
- The hydrogen is stored.
- The hydrogen is then used as fuel for fuel cells which produce energy. Fuel cells run on H_2 and O_2, and the only waste is H_2O.

All of these parts involve material challenges. In this thesis we are working with a possible future hydrogen storage material, so the focus of the next section will be hydrogen storage materials.

1.4 Hydrogen storage

It is very challenging to find good solutions for hydrogen storage. At ambient temperature and atmospheric pressure, 1 kg of H_2 gas has a volume of 11 m^3[13]. Knowing that a normal car needs 5 kg of hydrogen to drive 500 km, reveals that storage of hydrogen under high density is required. However, work must be applied to increase the hydrogen density; either to compress the gas; to cool the gas; or to reduce the repulsion initiated by the interaction of hydrogen with another material[13]. Furthermore, a hydrogen storage system should be easily reversible. The last criterion excludes all covalent hydrogen-carbon compounds because of the high release temperature for hydrogen (above 800°C[13]).

In general there are two important properties that have to be realized if the requirements for a society based on hydrogen as an energy carrier are to be met[14]:

(i) A hydrogen storage system for stationary applications.
(ii) A hydrogen storage system for mobile applications.

A hydrogen storage system for stationary applications has much smaller requirements when it comes to volume and weight, than systems for mobile applications. For stationary applications it is possible to use systems based on multiple step chemical reactions for the hydrogenation/dehydrogenation cycle. The temperature and pressure can be quite high, and the kinetics slow, since it is possible to compensate for this by extra capacity. In mobile applications the restrictions for temperature, pressure and kinetics are much stricter (see table 1.1). The six known methods that have the potential of meeting these requirements are[15]:

(i) High pressure gas cylinders (up to 800 bar).
(ii) Liquid hydrogen in cryogenic tanks (at 21 K).
(iii) Adsorbed hydrogen on materials with a large specific surface area (at T < 273K).
(iv) Through oxidation of reactive metals, e.g. Li, Na, Mg, Al, Zn with water.
(v) Absorbed on interstitial sites in a host metal (at ambient pressure and temperature).
(vi) Chemically bonded in covalent and ionic compounds (at ambient temperature).

These methods will now be briefly described, with the main focus on metal and complex hydrides.

Property	Target
Gravimetric storage density	> 6.5%
Volumetric storage density	> 70 kg/m^3
Dehydrogenation kinetics	< 3 hours
Hydrogenation kinetics	< 5 hours
Hydrogenation pressure	< 5MPa
Equilibrium pressure	~ 0.1 MPa at ambient temperature
Enthalpic effects	As low as possible
Safety	As high as possible, i.e. no ignition on exposure to air/water
Cycle stability	> 500

Table 1.1: Requirements for reversible hydrogen storage materials for mobile applications[16]. Values should be considered as approximate. Variations depend on target application, user philosophy, system requirements and technology already reached.

1.4.1 High pressure gas cylinders

High pressure gas cylinders are the most common way to store hydrogen. The new composite cylinders can store hydrogen with a volumetric density up to 36 kg/m^3[15]. Although there is relatively simple technology involved in the construction of the cylinders, and the storage in these systems is reversible, there are some substantial drawbacks including rather low hydrogen density combined with a very high pressure.

1.4.2 Liquid hydrogen

Liquid hydrogen has a volumetric density of 71 kg/ m^3[15], which is almost twice as much as for hydrogen stored under high pressure. Despite the high volumetric density, storage of hydrogen in liquid form is not preferable, since it has to be stored in cryogenic tanks at a very low temperature (21.2 K[15]). A large amount of energy is thus needed in the liquification process for hydrogen and the low temperature leads to an unavoidable and continuously boil-off of hydrogen. This clearly limits the use of liquid hydrogen systems to applications where costs are a minor issue, and where the hydrogen is consumed in a relatively short time, e.g. space technology[15].

1.4.3 Physisorption

Physisorption of hydrogen is characterized by Van der Waals bonds between gas molecules (H_2) and the surface atoms of a solid. The amount of adsorbed hydrogen stored in physisorption is proportional to the specific surface area of the adsorbent, or the storage system[15]. Systems or materials with big surface area are therefore preferred, e.g. nanotubes. Hydrogen is stored under rather low temperatures in these systems (< 273K). Advantages with physisorption includes the low operating pressure (easy to release hydrogen), the relatively low cost of the materials involved and the simple design of the storage system[15]. Disadvantages include a rather small amount of adsorbed hydrogen (only a maximum of 3 mass% on single-walled carbon nanotubes at 77K[13]), and the low temperatures or the high pressure needed.

1.4.4 Chemical reactions

Hydrogen can be generated by reacting metals and chemical compounds with water[15]. One example is when sodium reacts with water. Then Na is transformed to NaOH at the same time as H_2 is produced. This reaction has a gravimetric hydrogen density of 3 mass%[15], but it is not directly reversible. This, in addition to control of the thermal reduction process in order to produce the Na from LiOH are all challenging problems involved in this storage method. Also other metals or intermetallic compounds can be used. Examples include Li (gravimetric hydrogen density of 6.3 mass%[15]) and $NaBH_4$ (gravimetric hydrogen density of 4 mass%[17]).

1.4.5 Interstitial metal hydrides

Metals, intermetallic compounds and alloys generally react with hydrogen and mainly form solid metal-hydrogen compounds[15]. The electropositive elements are the most reactive, i.e., scandium, yttrium, the lanthanides, the actinides and members of the titanium and vanadium groups. In general metal hydrides consist of one or more transition metals and hydrogen. These hydrides primarily have metallic properties, and are therefore good conductors and have a metallic or graphite-like appearance.

Metal hydrides have many different compositions. The simplest compounds, binary hydrides (i.e. MH, MH_2 and MH_3), have large deviations from ideal stoichiometry and are called

interstitial metal hydrides since their lattice structure is that of a typical metal with hydrogen atoms in the interstitial sites[13]. More interesting are the ternary hydrides, which have the form AB_xH_n. These hydrides can be tailored with a variation of the elements. A is usually a rare earth or alkaline earth metal, and tends to form a stable hydride. B, often a transition metal, only forms unstable hydrides. There have been found some well defined ratios of A:B, where x = 0.5, 1, 2, 5[13], where hydrides with a hydrogen metal ratio up to two is formed. This means that metal hydrides have a very high volumetric density of hydrogen present in the host lattice. One of the highest volumetric densities found in a metal hydride is 115 kg H_2/m^3 in $LaNi_5$[13]. Even higher volumetric densities are found, but then the compounds are ionic or covalent, and hence belong to the complex hydride group which will be discussed in the next section.

Although metal hydrides are efficient at storing large amounts of hydrogen in a safe and compact way, only the hydrides consisting of transition metals are reversible at ambient temperature and atmospheric pressure. This means that the gravimetric hydrogen density is limited to less than 3 mass%[13], which is far to low for mobile applications. In spite of this, metal hydrides may be a good candidate for stationary applications, since they have smaller requirements when it comes to weight and volume than mobile applications.

1.4.6 Complex hydrides

The main difference between metal and complex hydrides is that complex hydrides are transformed to ionic or covalent compounds upon hydrogen adsorption. Complex hydrides usually consist of metals from group 1, 2 and 3, e.g. Li, Mg and Al[13]. Hydrogen is often located in the corners of a tetrahedron (there are many exceptions) with e.g. Al in the center. A cation, e.g. Na, compensates for the negative charge of the anion, $[AlH_4]^-$. The hydride complexes of borane, the tetra-hydro-borates $M(BH_4)$, and the tetra-hydro-aluminates $M(AlH_4)$ are known to be stable storage materials which only decompose at elevated temperatures[15]. More detailed studies of $NaAlH_4$[18],where titanium has been used as a catalyst, have revealed improved kinetics of this system. Bogdanović et al.[18] found that $NaAlH_4$ reversible release 4.2 mass% hydrogen through two steps. The second step occurs at approximately 100 ˚C[16], which makes sodium alanate the only known complex hydride with favorable thermodynamics and acceptable gravimetric storage capacity for use in combination with a PEM fuel cell system. A PEM fuel cell system operates at a temperature level of approximately 90 ˚C[16].

There are several interesting complex hydrides, including $LiBH_4$, which has one of the highest gravimetric hydrogen densities known today (18 mass%[15]). But common for them all are the slow kinetics. A new and very remarkable group of complex hydrides, the metal-N-H systems, will be discussed in the next section.

1.5 Metal-N-H systems

A very interesting group of complex hydrides are metal-N-H systems. Studies of such systems as hydrogen storage materials was initiated when Chen et al.[1] unintentionally found that a mixture of metallic lithium and carbon nanotubes pre-treated in a purified N_2 atmosphere could absorb a large amount of hydrogen. The hydrogenated solid-state sample was identified to contain $LiNH_2$, LiH and unreacted carbon nanotubes. Further investigation showed that the

N_2 treated Li-C mixture actually was composed of Li_3N and carbon nanotubes. And, according to Chen`s report, 9.3 mass% of hydrogen was reversibly stored in Li_3N by the following two-step reaction:

$$Li_3N + 2H_2 \leftrightarrow Li_2NH + LiH + H_2 \leftrightarrow LiNH_2 + 2LiH \quad (1.1)$$

However, the standard enthalpy change of the first step is -148 kJ/mol H_2[19], which means that a temperature of more than 430 ˚C is needed for a complete reversible hydrogen storage cycle. The second reaction has a much lower enthalpy change, -44.5kJ/mol H_2 [19]. The hydrogen storing capacity is still rather large, 6.3 mass%, but the release temperature for hydrogen is high[1]. Despite this, the metal-N-H systems are undoubtedly promising alternatives for new high performance hydrogen storage materials. A number of studies have therefore been devoted to these systems. This section will threat the thermodynamics and kinetics of some of these systems (table 1.2 shows some of the possible chemical reactions between amides and hydrides.) The systems where $Mg(NH_2)_2$ are involved will get a more thorough description, since this is the material investigated in this thesis.

1.5.1 Binary systems

Several binary metal-N-H systems have been investigated, including Li-N-H, Mg-N-H and Ca-N-H. All of them have high hydrogen content, but all of them are also thermodynamically very stable, and therefore unsuited for practical applications. The hydrogen desorption process from $LiNH_2$-2LiH and $LiNH_2$-LiH is, as already mentioned, highly endothermic [1]. The operation temperature at 1.0 bar equilibrium desorption pressure is therefore above 250 ˚C, which is too high for practical applications.

The Mg-N-H system has milder thermodynamics[20, 21]. During reaction B-4 (see table 1.2), Hu et al.[20] saw that a reaction between $Mg(NH_2)_2$ and MgH_2 at a feed ratio of 1:2 by means of ball milling resulted in the release of a stoichiometric amount of H_2 (7.4 mass%) and the formation of Mg_3N. MgNH was found in an intermediate step of the reaction. Hu et al. also did some thermodynamical calculations which showed that the hydrogen release reaction was mildly endothermic. Although the endothermic reaction enthalpy predicted a thermodynamical reversible hydrogen release, the reaction enthalpy was so low, that the operation condition for hydrogen uptake reactions would be unpractical.

1.5.2 Ternary systems

It is possible to improve the thermodynamical properties of metal-N-H systems by compositional alternation [22]. Li-B-N-H, Mg-Ca-N-H and Li-Mg-N-H are all new ternary systems which have been developed since 2004. In 2005 Pinkerton et al.[23] reported that 11.9 mass% of hydrogen can be desorbed from a reaction of a mixture of $LiNH_2$ and $LiBH_4$ (reaction T-1 in table 1.2). But the overall reaction was exothermic and, hence, not feasible under normal conditions.

Liu et al.[24] checked the hydrogen desorption properties of a Mg-Ca-N-H system in 2007 (reaction T-2 in table 1.2). They found that 3.9 mass% of pure H_2 gas was released during ball milling. More interesting, the average heat desorption was measured to be 28 kJ/mol H_2, implying that it could be a low temperature hydrogen storage system. But the kinetic barrier

for both dehydrogenation and hydrogenation was very high, which makes the system unpractical for normal applications.

System		Reaction	Mass%	Ref.
Binary	B-1	$LiNH_2 + 2LiH \leftrightarrow Li_3N + 2H_2$	9.3	[1]
	B-2	$LiNH_2 + LiH \leftrightarrow Li_2NH + H_2$	6.5	[1, 25]
	B-3	$Mg(NH_2)_2 + MgH_2 \rightarrow 2MgNH + H_2$	4.8	[21]
	B-4	$Mg(NH_2)_2 + 2MgH_2 \rightarrow Mg_3N_2 + 4H_2$	7.4	[20]
Ternary	T-1	$2LiNH_2 + LiBH_4 \rightarrow Li_3BN_2 + 4H_2$	11.9	[23]
	T-2	$Mg(NH_2)_2 + CaH_2 \rightarrow MgCa(NH)_2 + 2H_2$	3.9	[24]
	T-3	$Mg(NH_2)_2 + 2LiH \leftrightarrow Li_2Mg(NH)_2 + 2H_2$	5.6	[26, 27]
	T-4	$2LiNH_2 + MgH_2 \leftrightarrow Li_2Mg(NH)_2 + 2H_2$	5.4	[28]
	T-5	$8LiH + 3Mg(NH_2)_2 \leftrightarrow Mg_3N_2 + 4Li_2NH + 8H_2$	6.9	[29]
Multinary	M-1	$NaNH_2 + LiAlH_4 \rightarrow NaH + LiAlNH + 2H_2$	5.0	[30]
	M-2	$3Mg(NH_2)_2 + 3LiAlH_4 \rightarrow Mg_3N_2 + Li_3AlN_2 + 2AlN + 12H_2$	8.5	[31]

Table 1.2: An overview over chemical reactions between various amides and hydrides[22] in addition to the corresponding theoretical hydrogen capacity in mass%.

A system consisting of Li-Mg-N-H considerably improves the thermodynamic properties for the binary Li-N-H and Mg-N-H systems. $Li_2Mg(NH_2)$ can be formed from both reaction T-3 [32] and T-4[28] (see table 1.2). Since $Mg(NH_2)_2 + 2LiH$ is thermodynamical more favorable than $2LiNH_2 + MgH_2$[33], reaction T-3 is the most probable one[32]. Lately, there has been done a lot of research on these systems, where different $Mg(NH_2)_2$ and LiH ratios have been tested. Ichikawa et al. is one of the groups which has worked intensively with this. They have looked at many different metal-N-H systems and based on this work they are of the opinion that a system based on $Mg(NH_2)_2$ and LiH[29] is most promising for hydrogen storage in mobile applications. Their main focus have been on reaction T-5 (see table 1.2), since they think this LiH:$Mg(NH_2)_2$ ratio is most suitable when it comes to hydrogen storage[29]. This reaction includes the decomposition from $Mg(NH_2)_2$ to Mg_3N_2 through MgNH, leading to a hydrogen capacity up to 6.9 mass%[34]. Leng et al.[34] found that this mixture desorbs more than 5 mass% at 150 ˚C during ball milling. They also confirmed the reversibility of the reaction by repeating the dehydrogenation after a hydrogenation under 10Mpa at 200 ˚C.

One of the major problems with the Li-Mg-N-H systems, and metal-N-H systems in general, is that NH_3 often is included as one of the decomposition products. This is a serious problem since most fuel cells will be poisoned by only small amounts of NH_3[35]. Another problem is that if the decomposition of metal-N-H system involves loss of nitrogen, this induces a change in the chemical composition of the material, which, consequently, will degrade the cycling hydrogen storage capacity. During investigation of the equilibrium concentration of NH_3 in the Li-Mg-N-H system, Lie et al.[35] found that the dominant source for NH_3 formations stems from $Mg(NH_2)_2$.

The ternary systems are still object for serious investigation, since there are still many new systems to be tested, in addition to the fact that only a small compositional change within a given ternary system can induce considerable variations in the reaction path. These variations enable a broad scope for material optimization and engineering[22].

1.5.3 Multinary systems

Multinary systems, materials containing more than two metal or metalloid elements, are also good candidate for new high-performance hydrogen storage materials. These systems have a more complicated chemical process than binary and ternary systems, making them a bit more intricate to examine. Two of the systems investigated so far are the $NaNH_2$-$LiAlH_4$ system[30] and the $Mg(NH_2)_2$-$LiAlH_4$ system[31]. For the $Mg(NH_2)_2$-$LiAlH_4$ system Liu et al.[31] observed that M-2 (see table 1.2) was a complex reaction, involving several steps. But since the system possesses a high hydrogen content of 8.5 mass%, where 6.2 mass% could be released by ball milling near ambient temperature, and in addition has good hydrogen reversibility[31], it could be a potential candidate for on-board hydrogen storage. So further investigation of this and other multinary systems should be and are being performed.

1.5.4 This thesis

Although $Mg(NH_2)_2$ as a binary system not is promising for hydrogen storage in mobile applications (see chapter 1.5.1), it can be when it is combined with other metal-N-H systems, especially LiH, and form a ternary or multinary system (see chapter 1.5.2 and 1.5.3). To improve the knowledge and understand the underlying physics of these ternary/multinary systems, thorough knowledge about each component constituting these systems is important. This thesis seeks to further understand the properties of $Mg(NH_2)_2$ and an analysis of the crystal structure, the electronic density of states and six selected surfaces of $Mg(NH_2)_2$ were performed using density functional theory. The main focus has been on a new method for doing DFT calculations on complex hydrides in a plane wave code, so called cluster calculations. Here, the building of a suitable cluster for further calculations was given considerable attention. Also some further calculations were performed on the clusters, among them calculations of the activation energy involved in the removal of H_2 or NH_3 from the clusters.

Earlier studies of $Mg(NH_2)_2$ involve structure studies performed by Jacobs et al.[36] (using single crystal X-ray diffraction), Sørby et al.[37] (using high resolution powder neutron and synchrotron X-ray diffraction) and Velikokhatnyi et al.[38] (using density functional theory). Jacobs et al. and Sørby et al. found that $Mg(NH_2)_2$ had a tetragonal crystal structure belonging to space group $I4_1/acd$ (further discussed in chapter 3). Velikokhatnyi et al. calculated the electronic structure, structural parameters, vibrational spectra and the enthalpies of formation for $Mg(NH_2)_2$ and found good agreement between their calculated and Jacobs et al.`s structural parameters (also further discussed in chapter 3). The enthalpy of formation for $Mg(NH_2)_2$ has also been obtained experimentally by Hu et al.[20], and there were good agreement between their and Velikokhatnyi et al.'s calculated results. Furthermore, at least to our knowledge, there are no previously reported surface studies of $Mg(NH_2)_2$. Neither have there been performed any cluster calculations on this system.

Chapter 2

2 Computational methods

During the last decade, computer simulations based on a quantum-mechanical description of the interaction between electrons and atomic nuclei have strongly influenced the development of material science[39]. This chapter will give an introduction to density functional theory (DFT), a theory which allows detailed investigation of many particle systems. The methodology part of Gustav Karlberg's Ph. D. thesis[40] has been used as a guideline for this part of the chapter. Two modern DFT software's, VASP[41] and ADF[42], will also be presented.

2.1 Density functional Theory

Density functional theory (DFT) is an important theory developed by Hohenberg, Kohn and Sham in the 1960`s[43, 44]. The theory allows investigations of many particle systems with great computational advantage compared to quantum mechanics, in which use of state-of-the-art computers only give solutions for the Schrödinger equation for systems consisting of a small number of atoms and molecules. This section will show the procedures and approximations involved in going from traditional quantum mechanics to DFT.

2.1.1 The Born-Oppenheimer approximation

In classical quantum mechanics the time dependent Schrödinger equation [45] for a many particle problem can be written:

$$\hat{H}\Psi = i\hbar \frac{\delta \Psi}{\delta t} \qquad (2.1)$$

where Ψ is the wave function. $\hat{H}$ is the systems Hamiltonian, which in atomic units reads:

$$\hat{H} = -\frac{1}{2M_I}\sum_I \nabla_I^2 + \frac{1}{2}\sum_{I\neq J}\frac{Z_I Z_J}{|\vec{R}_I - \vec{R}_J|} - \frac{1}{2}\sum_i \nabla_i^2 + \frac{1}{2}\sum_{i\neq j}\frac{1}{|\vec{r}_i - \vec{r}_j|} - \sum_{i,I}\frac{Z_I}{|\vec{r}_i - \vec{R}_I|} \qquad (2.2)$$

where the nuclei with mass M_I and charge Z_I are denoted by upper case subscripts, and the electrons with lower case subscripts. The first term represents the kinetic energy of the nuclei and the second term represents the nucleus-nucleus interaction. The last three terms represent the kinetic energy of the electrons, the electron-electron interaction and the electron-nucleus interaction, respectively.

The first major simplification of the Hamiltonian for a many particle system was done by Born and Oppenheimer[46]. Due to the great difference in mass between the electrons and the nuclei, they regarded the kinetic energy term for the nuclei as small[1], which means that on the time scale of the electronic motion, the nuclei will appear to be fixed. As a consequence of this, the time-dependent Schrödinger equation can be separated into the electronic structure problem and the nuclear motion problem.

For the electronic structure problem, the time independent Schrödinger equation reads:

$$\hat{H}_{BO}\Phi = E\Phi \qquad (2.3)$$

where Φ is the N-electron spin dependent wave function $\Phi(\vec{r}_1 s_1, \ldots, \vec{r}_N s_N)$, while $\hat{H}_{BO}$ is the Born-Oppenheimer Hamiltonian:

$$\hat{H}_{BO} = \frac{1}{2}\sum_{I\neq J}\frac{Z_I Z_J}{|\vec{R}_I - \vec{R}_J|} - \frac{1}{2}\sum_i \nabla_i^2 + \frac{1}{2}\sum_{i\neq j}\frac{1}{|\vec{r}_i - \vec{r}_j|} - \sum_{i,I}\frac{Z_I}{|\vec{r}_i - \vec{R}_I|} \qquad (2.4)$$

which in short can be written:

$$\hat{H}_{BO} = E_{II} + \hat{T}_e + \hat{V}_{\text{int}} + \hat{V}_{ext} \qquad (2.5)$$

Here, E_{II} represents the nucleus-nucleus interaction, T_e the kinetic energy of the electrons, V_{int} the electron-electron interaction and V_{ext} the electron-nucleus interaction. It is also important to remember that the electrons obey the Pauli exclusion principle, which gives a symmetry requirement on the electronic wave function. Another consequence of the Born-Oppenheimer approximation is that the nuclei are treated as classical particles. This means that the many particle problem has been reduced to an interacting electron gas, moving in the static external potential V_{ext} setup by the ions.

2.1.2 The Hohenberg-Kohn theorems

DFT is, as the name suggests, a theory that focuses not on the electronic wave function, but on the electronic density. The major advantage from a computational point of view is that the electronic density depends only on the three variables of space, while the wave function for an N electron system depends on $3N$ variables.

The connection between the density and the wave function was showed by Hohenberg and Kohn and stated in the Hohenberg-Kohn theorems[43]. They can be written[47]:

(i) The external potential V_{ext} and hence the total energy E[n], is a unique functional[2] of the electron density $n(\vec{r})$.

[1] The kinetic energy is proportional to 1/M.
[2] A functional is a function that takes functions as its argument.

(ii) The ground state energy can be obtained variationally; the density that minimizes the total energy is the exact ground state density.

The first theorem shows that the Hamiltonian is fully determined by the ground state density, which means that all the physical properties of the system are completely determined by the ground state density. The second theorem demonstrates that the energy functional can be used to find the ground state density. Importantly, the excited states need to be determined in a different way, since DFT is a ground state theory.

2.1.3 The Kohn-Sham equations

The use of density as the basic variable in a quantum mechanical many particle problem was justified by the Hohenberg-Kohn theorems in 1964. In 1965 Kohn and Sham[44] gave the guidelines for a practical implementation of these theorems. Taking the Hohenberg-Kohn theorems as a starting point, they claimed that for an electronic structure problem, any electron system giving rise to the same electron density as the system under investigation, can be used to find the physical properties of the system. *"In particular, a system with non-interacting electrons may be used if it can be shown to have the same ground state electronic density as the interacting system"*[40]. Kohn and Sham therefore introduced a system of non-interacting electrons[3] moving in an effective potential. This formed the Kohn-Sham equations, a system of coupled single particle Schrödinger like equations:

$$\left(-\frac{1}{2}\nabla^2 + V_{KS}(\vec{r})\right)\Psi\ (\vec{r}) = \varepsilon_i \Psi_i(\vec{r}) \qquad (2.6)$$

Here $\Psi_i(\vec{r})$ are the single particle orbitals, which must be mutually orthogonal. The Kohn-Sham equations are non-linear, since the effective potential, $V_{KS}(\vec{r})$, depends on the density. By using an iterative scheme, the equations can be solved in a self consistent way. The effective potential V_{KS} for a given $n(\vec{r})$ is determined with help from the variational property of the energy. The energy functional is given by:

$$E_{KS}\left[n(\vec{r})\right] = T_0\left[n(\vec{r})\right] + \int d\vec{r} V_{ext}(\vec{r}) n(\vec{r}) + E_H\left[n(\vec{r})\right] + E_{XC}\left[n(\vec{r})\right] + E_{II} \qquad (2.7)$$

where T_0, E_H and E_{II} are the kinetic energy contribution, the electron-electron interaction and the nucleus-nucleus interaction, respectively. The second term represents the nucleus-electron interaction. Importantly, the exchange and correlation energy, E_{XC}, is a term that represents all the many-particle interactions.

Kohn and Sham gave a recipe for how to perform the calculations for many particle systems, as well as they separated the manageable parts from the difficult part, the exchange and correlation energy, E_{XC}. The exchange part of E_{XC} is a consequence of the exchange symmetry between identical fermions, while the correlation part is a consequence of the coupling of electrons caused by Coulomb interactions. There exist no exact solutions for E_{XC}, so it has to be approximated. There are several ways of doing this. Two of the most popular methods are the local density approximation (LDA)[43] and the generalized gradient approximation

[3] The non-interacting electrons are quasi particles with no physical meaning.

(GGA)[48]. In LDA, the actual exchange-correlation energy at a certain point $\vec{r}$, is replaced with the well known results of a homogeneous electron gas with the same density $n(\vec{r})$. Despite the crude approximation done in LDA, the approximation works surprisingly well. However, there are some well known errors[49] in the use of LDA: Band gaps in semiconductors and insulators are systematically underestimated, Van der Waals forces and hydrogen bonds are poorly described and there is a problem with overbinding resulting in incorrect energies and lattice parameters. Improvements of LDA can be made by including information on the gradient of the density at each point, which is the basis of GGA. GGA corrects for most of the errors done by LDA, but underestimation of the band gap is still present.

2.1.4 Basis sets

Hohenberg, Kohn and Sham's reformulation of the time independent Schrödinger equation was a great step towards an efficient method for solving the electron structure problem of condensed matter. Nevertheless, when a suitable approximation for the exchange-correlation energy is found, the numerical problem of solving the Kohn-Sham equations still remains a demanding task.

An important part of the solution process is to find an appropriate basis set for the single particle wavefunctions, $\Psi_i(\vec{r})$. It is important that the basis set is chosen so that it gives the desired accuracy, while it at the same time is sufficiently small to be computationally cheap. Depending on the localization and periodicity of the electron system under study, different basis sets could be of interest. For crystal structures, there are four types of basis sets that predominantly are used to span out the electron density[49], i.e.: linear combinations of atomic orbitals (LCAO); linear augmented plane waves (LAPWs); plane waves(PWs); or projector augmented waves (PAW).

In LCAO calculations, atomic orbitals are expressed as products of angular momentum eigenfunctions and radial orbitals[49]. The radial functions are either represented numerically, or in terms of linear combinations of Slater-type or Gaussian type orbitals. LCAO are efficient for systems with localized functions, and usually give the best results for calculations performed on molecules or molecular solids, which are systems where the atomic region is the most important region. On the other hand, in many systems the interstitial region is very vital, since this is where the actual binding occurs. Then it would be advisable to use a plane wave basis set.

In LAPWs calculations, atomic wave functions are used in the atomic region and plane waves are used in the interstitial region. Here, it is important that the wave functions and their derivatives are continuous at the boundary of the two regions.

PWs, have several advantages[49], including convergence with respect to the completeness of the basis set is easily checked by extending the cut-off energy (i.e. the highest kinetic energy in the PWs basis) and that the forces on atoms and stresses on the unit cell may be calculated directly via the Hellmann-Feynman theorem. A plane wave is a solution of the Schrödinger equation for a free electron. Furthermore, any wavefunction can be described with a linear combination of them. However, since a plane wave basis set is $\vec{k}$-dependent[4], one has to

[4] $\vec{k}$ is the wave number in the Brillouin zone.

choose a new basis set for each $\vec{k}$ that is included in the calculations[50]. The number of $\vec{k}$ should be as small as possible to prevent unnecessary computational time, but large enough to assure accurate enough sampling of the first Brillouin zone. Another drawback with PWs is that in order to achieve convergence within a system where plane waves are used as basis, a pseudo-potential has to be used[49]. In pseudo-potentials, the effect of the ion potential and the core electrons are replaced by an effective ionic potential acting on the valence electrons only, which reduce the computational costs greatly, since the number of electrons needed to be treated has decreased. For systems with periodic boundary conditions, LAPWs or PWs is recommended since these basis sets describe the interstitial region of the investigated system very well.

A combination of LAPWs and PWs was suggested by Blöchl in 1994[51]. This method is called the Projector Augmented Wave (PAW) method and it is a formal generalization of the pseudo-potential and augmented wave methods. The PAW method is based on a transformation between the full all-electron solution of the Kohn-Sham equation and the pseudo-wavefunction. If this transformation is known, the pseudo-Hamiltonian can be diagonalized by using a small plane wave basis, and then transform the solutions to the all-electron solutions.

2.2 The Vienna Ab-initio Simulation Package

The Vienna *Ab-initio*[5] Simulation Package, VASP[41], is a modern DFT software for performing quantum-mechanical simulations using pseudo-potentials or the projector-augmented wave method and a plane wave basis set. This section will first give a short presentation of the main structure of VASP, the software used in the majority of the calculations done in this thesis. At the end some introductory tests performed on $Mg(NH_2)_2$ and a detailed description of the parameters used in VASP during this thesis will be specified.

2.2.1 In- and OUTPUT files

Common for all VASP calculations are that various INPUT files have to be specified. The INPUT files are:

INCAR Specification of the calculation which needs to be performed and the algorithms used for the calculation.

POSCAR Dimensions of the unit cell and the positions of the atoms.

POTCAR Specifies the potential of the various elements in the unit cell.

KPOINTS Defines the $\vec{k}$-points to be included in the numerical integration over the Brillouin zone.

The best DFT calculations in VASP are performed when the most suitable potentials and the proper numerical algorithms are chosen for the problem of interest. It is also important that the $\vec{k}$-space mesh is dense enough to give the desired accuracy, but small enough to prevent

[5] *Ab-initio* means from first principles only (no experimental data is needed).

unnecessary computational time. All of these parameters and various other details are specified in the INPUT files.

When a calculation is done, a number of OUTPUT files will be returned from VASP. Some of them are:

OUTCAR Main OUTPUT file. Contains information about $\vec{k}$-points, energies, forces and atomic positions for each iteration the program does.

DOSCAR The density of states and the Fermi level.

CHGCAR The charge density in e/V_{cell}.

CONTCAR New positions of the atoms after ionic relaxation. For static jobs CONTCAR is identically to POSCAR.

There are several more OUTPUT files available from VASP, depending on which input parameters specified in the INPUT files.

2.2.2 The main structure

The approach implemented in VASP is based on the (finite-temperature) local-density approximation with the free energy as variational quantity and an exact evaluation of the instantaneous electronic ground state at each time step[41]. Efficient matrix diagonalisation schemes and efficient Pulay/Broyden charge density mixing are used[41]. For the description of the interaction between ions and electrons two choices are available[41]:

(i) ultra-soft Vanderbilt pseudopotentials (US-PP);
(ii) or the projector-augmented wave (PAW) method.

Both these alternatives ensure that the size of the basis set can be kept very small even for transition metals and first row elements like carbon and oxygen[41]. Generally not more than 100 plane waves (PW) per atom are required to describe bulk materials, in most cases even 50 PWs per atom will be sufficient for a reliable description[41]. In this thesis the PAW method was used, since it gives accurate results and at the same time is highly efficient. Another feature in VASP is that forces and the full stress tensor can be calculated, which in turn can be used to relax atoms into their instantaneous ground-state. Here several different algorithms are available in VASP. The two used in this thesis are:

(i) Conjugate gradient algorithm;
(ii) Residual vector minimization method – direct inversion in iterative space (RMM-DIIS)[52].

(i) is well suited for difficult relaxation problems, while (ii) is usually the best choice when the initial structure is close to a local minimum[41]. Both these algorithms use an iterative matrix-digitalization scheme. Here the input wavefunctions and charge density are independent quantities. The charge density is used to set up a Hamiltonian. The wavefunctions are then optimized iteratively to get as close as possible to the exact wavefunctions of this Hamiltonian. The new wavefunctions are then used in the calculations

of a new charge density, which combined with the old charge density makes a new charge density that will be used to set up a new Hamiltonian. This cycle is then repeated until the required break criterion is reached. The last scheme, (ii), is probably among the fastest schemes currently available[41].

2.2.3 Computational details and initial calculations in VASP

The majority of the calculations in this thesis have been performed using VASP[2, 8, 9] employing the projector augmented wave(PAW) method[53], using the Perdew-Burke-Emzerhof (PBE) functional[54] at the generalized gradient approximation[55] level. The PAW-PBE potential at the GGA level has been used as an approximation of the exchange and correlation energy, since this potential has shown to give reliable results for many materials, including complex hydrides. Furthermore, the standard version pseudo-potentials with the valence configurations $2s^2 2p^0$ for Mg, $2s^2 2p^3$ for N and $1s^1$ for H were used. The self-consistency of the electron density was defined to be reached when the total energy of two consecutive runs differed by less than 0.01 meV. The single-particle orbitals were smeared by a Gaussian convolution with a width of 0.01 eV in most of the cases (a width of 0.2 eV was also used (see chapter 5.3.1), but the difference in the calculated total energy of the system was very small between the two widths).

Cut-off energy (eV)	Total energy (eV)
250	-1112.4642
300	-1116.3223
350	-1120.3836
400	-1123.7360
450	-1124.7086
500	-1124.9261
550	-1125.0182
600	-1125.1652
650	-1125.3320
700	-1125.4301
750	-1125.4838
800	-1125.5267
850	-1125.5304
900	-1125.5303

Table 2.1: The total energy of the unit cell of $Mg(NH_2)_2$ as a function of cut-off energy

To assure desired accuracy in the calculations, and to prevent unnecessary computational time, some preliminary tests were performed on $Mg(NH_2)_2$, where the experimental structure from Ref.[37] was used as input structure. At first, a cut-off energy test was carried out. Here, the total energy of the system was calculated for increasing cut-off energies. From table 2.1 it is possible to see that for a cut-off energy of 850 eV for the plane wave expansion, the total energy of the system has converged within 1 meV. This means that the error in the total energy calculations for $Mg(NH_2)_2$ is less than 1 meV if a cut-off energy of 850 eV is used. This cut-off energy has therefore been used in all further calculations performed in VASP during this thesis.

A similar test was also performed for the size of the $\vec{k}$-point mesh, now with total energy as a function of number of $\vec{k}$-points instead of cut-off energy. Here, both an equal number of $\vec{k}$-points in every direction, in addition to an equal number of $\vec{k}$-points in the x- and y- direction, with a smaller number of $\vec{k}$-points in the y-direction have been tested (since $Mg(NH_2)_2$ has a tetragonal unit cell, see chapter 3). From table 2.2 it is possible to see that an error of less than 1 meV is obtained in the total energy for $Mg(NH_2)_2$ if a $\vec{k}$-point mesh of 2 x 2 x 1 is used, which, thus, is used in all the bulk calculations done in this thesis.

During the slab calculations, the same number of $\vec{k}$-points as used in the bulk calculations were specified in the plane of the slabs, while only one $\vec{k}$-point was needed in the direction perpendicular to the slabs, since the band dispersion in this direction is zero due to the vacuum layer.

In the cluster calculations vacuum layers were inserted in all directions. This means that only a $\vec{k}$-point mesh of 1 x 1 x 1 was needed, since the band dispersion in all directions are zero.

$\vec{k}$-point mesh	# of irreducible $\vec{k}$-points	Total energy (eV)
1 x 1 x 1	1	-1125.5513
2 x 2 x 1	3	-1125.6107
2 x 2 x 2	6	-1125.6105
4 x 4 x 2	12	-1125.6105
4 x 4 x 4	18	-1125.6106
6 x 6 x 4	30	-1125.6106

Table 2.2: Corresponding $\vec{k}$-points mesh, number of irreducible $\vec{k}$–points and total energy of the unit cell.

The ionic relaxations in VASP were performed by the residual minimization method - direct inversion in iterative subspace(RMM-DIIS)[52] (see chapter 2.2.2). This is an implementation of the quasi-Newton algorithm and both the atomic positions as well as the cell parameters were optimized for the bulk structure. The ionic relaxation of the slabs was more difficult, so here the conjugate-gradient algorithm was first used on the initial structure, before the quasi-Newton algorithm was used to give the final structure. For the slabs, only the atomic positions were optimized. During the ionic relaxation of the clusters two different software's, Amsterdam Density Functional[42] and VASP, had to be used (see chapter 5.2.1 for a detailed description of the procedure). Also here, only the atomic positions were optimized. Furthermore, the criterion for relaxation for bulk, slab and clusters was that the forces between two atoms in the unit cell were less than 0.05 eV/Å.

2.3 Amsterdam Density Functional

Amsterdam Density Functional (ADF)[42, 56] also is a DFT software for first-principle electronic structure calculations. ADF supports a wide variety of exchange correlation functionals[56] and uses a Localized Combination of Atomic Orbitals (LCAO) (see Chapter 2.1.4), more specifically Slater-type orbitals(STO), as a basis set. This means that ADF may treat the atomic region better than VASP, which uses PWs as a basis set. Since ADF has only been used for intermediate cluster calculations in this thesis (see chapter 5.2.1), a description

of the structure of the software will not be given. Interested readers are referred to Ref. [13]. Here, only the most important parameters used during the intermediate calculations will be presented.

2.3.1 Computational details in the ADF calculations

The calculations in ADF were performed using the Perdew-Burke-Emzerhof (PBE) functional[54] at the generalized gradient approximation[55] level. For both total energy calculations and ionic relaxation a triple zeta plus one polarization (TZP) basis set[42, 56] with no frozen core was used to assure the desired accuracy. Furthermore, the general accuracy parameter in ADF[42, 56] was set to 4.0 based on initial convergence tests of the total energy of the clusters. The criterion for relaxation of the clusters was the same as in the VASP calculations, which means that the forces between two atoms in the unit cell were less than 0.05 eV/Å.

2.4 Computer facilities

All calculations in both VASP and ADF during the course of this thesis were performed at *njord*, one of the most powerful super-computers in Norway. *Njord* is a distributed shared memory system which consists of IBM p575+ nodes interconnected with a high-bandwidth low-latency switch network[57]. It has 59 shared memory compute nodes with eight dual-core power5+ processors[57]. 55 compute nodes have 32 GB memory, while four compute nodes have 128 GB memory[57]. The 128 GB nodes were used in all relaxations of slabs and clusters in VASP during this thesis due to the large memory needed in these calculations. The other calculations in VASP and all the calculations in ADF were performed with the 32 GB nodes.

Chapter 3

3 Calculation of the bulk- and the electronic- structure of $Mg(NH_2)_2$

This chapter will treat the bulk calculations performed on $Mg(NH_2)_2$. To begin with I will establish a knowledge of $Mg(NH_2)_2$'s bulk structure, comparing it to experimental and previously calculated structures. I will then give a brief analysis of the thermodynamics, the density of states and the chemical bonds in $Mg(NH_2)_2$.

3.1 Bulk structure

The relaxed bulk structure of $Mg(NH_2)_2$ was found by ionic relaxation of the experimental bulk structure of $Mg(ND_2)_2$ found by Sørby et al.[37], whom had used the structure model reported by Jacobs et al.[36] in 1969 as a starting point for their work. Figure 3.1 and 3.2 shows one unit cell of the relaxed $Mg(NH_2)_2$ bulk structure viewed from the [100] direction. Here, the green spheres represent Mg atoms, the blue spheres represent N atoms, while the red spheres represent H atoms. This representation of the atoms is used throughout this thesis. Furthermore, usually only the N-H bonds are visualized in figures of the different slabs and clusters in this thesis, since visualizing of too many bonds makes it difficult to observe the symmetry properties in the different figures. The N-H bonds were drawn when the interatomic distance between a N and a H atom was in the range from 0.6 Å to 1.2 Å. For some selected figures though, bonds between other atoms were also drawn, since this in some situations helped visualize the symmetry properties of the atomic structure more thoroughly. In figure 3.2 the tetrahedral configuration of amides around Mg is showed. From this figure it is clear that the cations in $Mg(NH_2)_2$ (i.e. Mg^{2+}) are tetrahedrally coordinated by the anions (i.e. NH_2^-) and that the MgN_4 tetrahedra share all four corners with other MgN_4 tetrahedra, thus forming an open, three dimensional network[37]. The unit cell is tetragonal (space group: $I4_1/acd$[37]) and large, consisting of 224 atoms. This means that the calculations done on $Mg(NH_2)_2$ were computationally demanding in both time and memory consumption.

To further explore some of the symmetry properties of the relaxed bulk structure of $Mg(NH_2)_2$, selected parts of the bulk structure are shown in figure 3.3 and 3.4. In figure 3.3 the bulk structure is viewed from the $[11\bar{1}]$ direction such that a side view of the (112) planes is obtained. This figure shows that two and two atom layers periodically curve upwards and downwards, and that the neighboring layers (both above and underneath) always curves in the opposite direction. This curving creates an increased distance between every second layer of atoms in the (112) plane (note that the distance not is increased in the intersection between upward and downward curving). This means that the chemical bonds between every second layer of atoms in the (112) plane probably are weak, indicating that a surface constructed from a (112) plane most likely will have low surface energy, since only weak bonds have to be broken in the creation. Surfaces will be further discussed in chapter 4, where the (112)

surface proved to be one of $Mg(NH_2)_2$'s most stable surfaces. In figure 3.4 the bulk structure is viewed from the $[1\bar{1}0]$ direction, giving a side view of both the (112) and $(11\bar{2})$ planes. Comparison between this figure and figure 3.3 shows that the bulk structure of $Mg(NH_2)_2$ are organized in weakly connected branches, where the branches point in the $[1\bar{1}0]$ or the $[\bar{1}10]$ direction, and each branch is separated from the other branches by the (112) and the $(11\bar{2})$ planes. This means that the atoms belonging to one branch probably are more strongly bonded to each other than surface atoms on neighboring branches are. This is due to longer interatomic distance between atoms belonging to neighboring branches than atoms belonging to the same branch. The symmetry properties of $Mg(NH_2)_2$'s structure will be further discussed in chapter 4, 5 and 6.

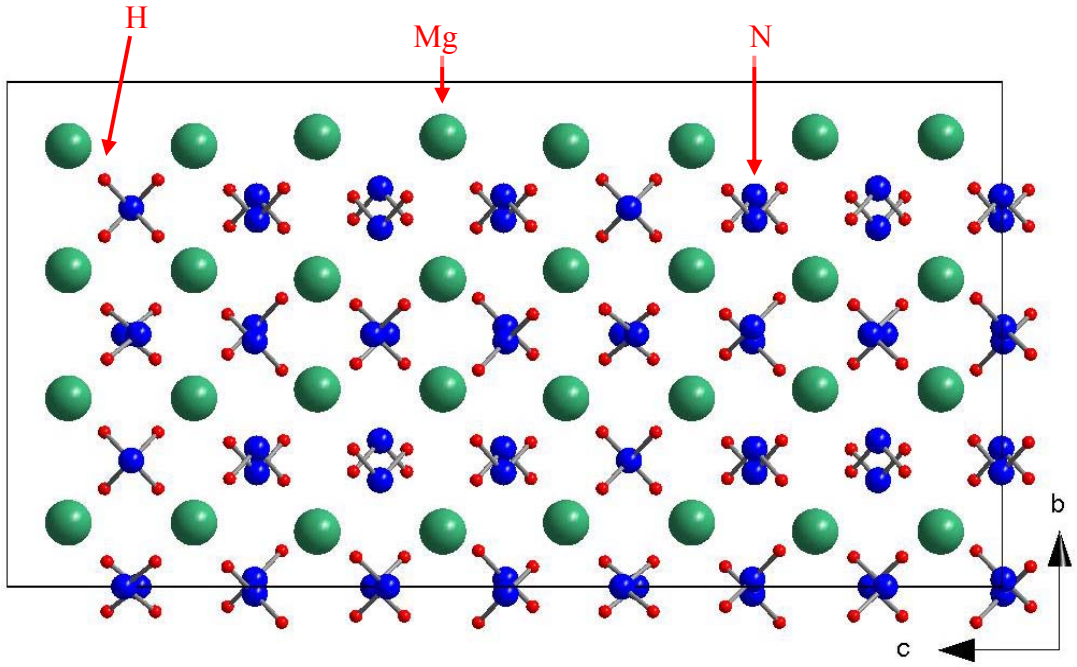

Figure 3.1: One unit cell of the relaxed $Mg(NH_2)_2$ bulk structure.

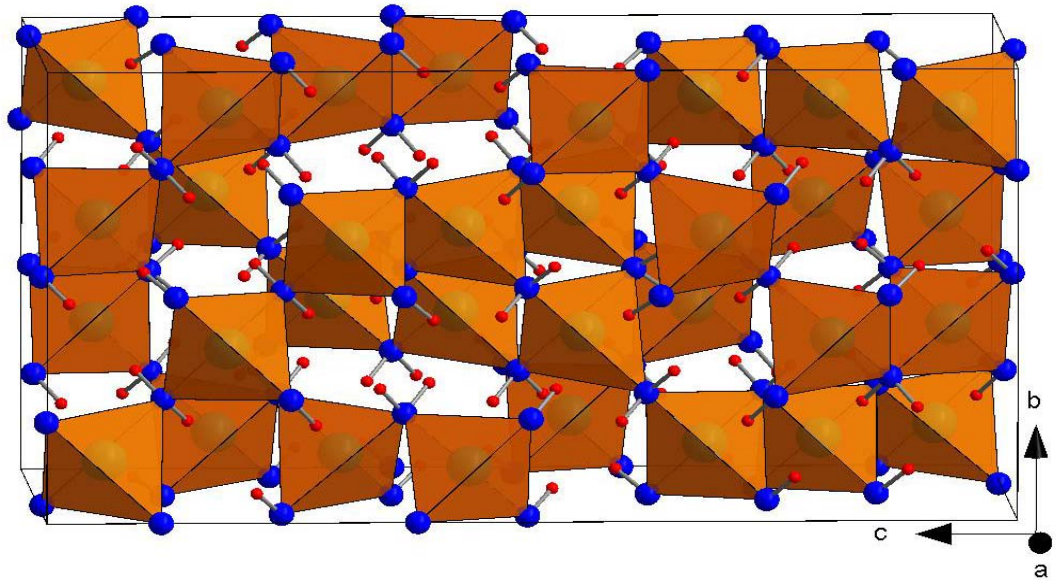

Figur 3.2: One unit cell of the relaxed $Mg(NH_2)_2$ bulk structure visualizing the tetrahedral configuration of amide units around the magnesium ions.

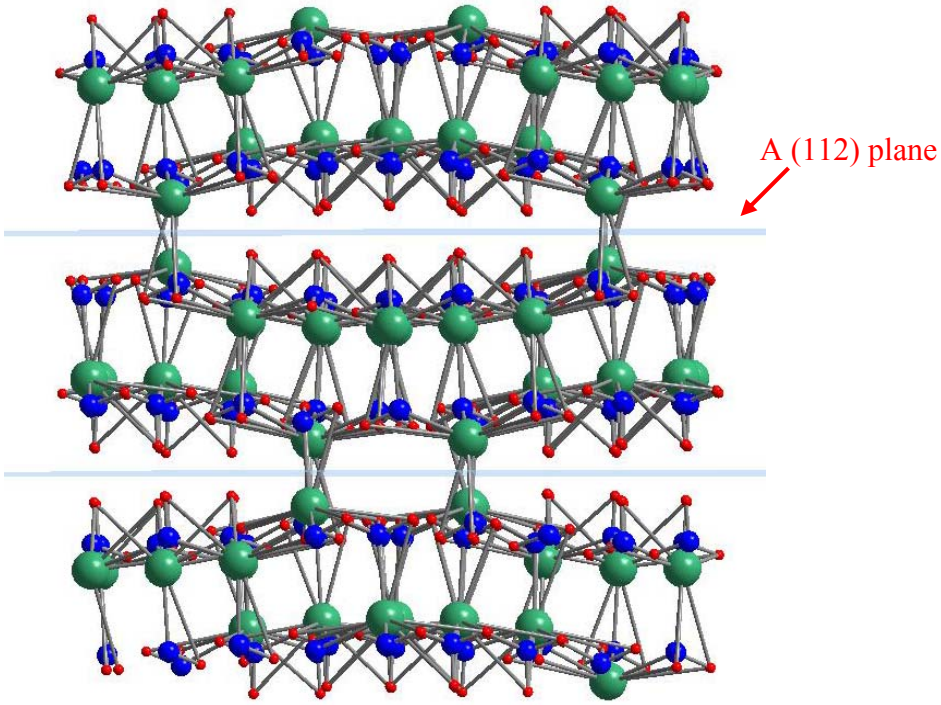

Figure 3.3: A chosen part of the bulk structure of $Mg(NH_2)_2$ viewed from the $[11\bar{1}]$ direction. Here, the Mg-N and Mg-H bonds are drawn in addition to the N-H bonds (The Mg-N and the Mg-H bonds were drawn for interatomic distances between 1.4 and 2.8 Å, while N-H bonds were drawn for interatomic distances between 0.6 and 1.2 Å). Notice the increased distance between every second atom layer.

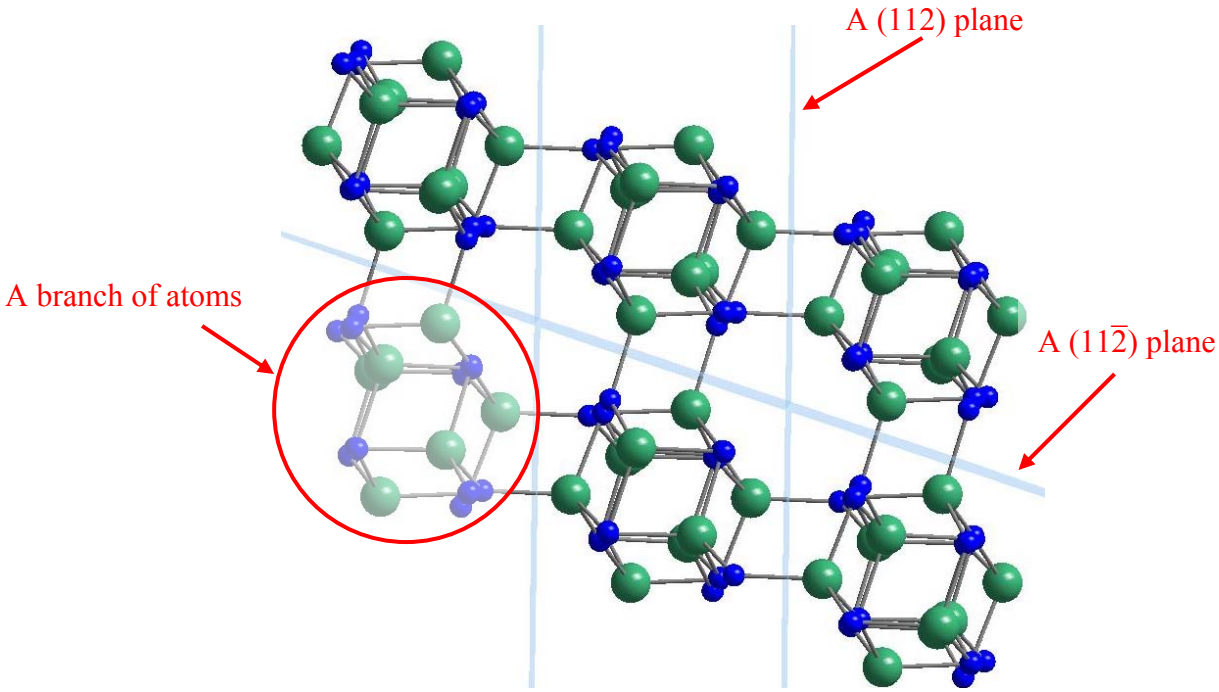

Figure 3.4: A chosen part of the bulk structure of $Mg(NH_2)_2$ viewed from the $[1\bar{1}0]$ direction. H atoms are not drawn, since this makes it easier to observe the symmetry properties. The Mg-N bonds are drawn for interatomic Mg-N distances from 1.4 Å to 2.8Å. It is easier to visualize the weakly connected branches when figure 3.3 and 3.4 are compared to each other.

3.1.1 Comparison between calculated and previously found bulk structures

In Table 3.1 the lattice constants found experimentally[36, 37] and by the present calculations are given in addition to the lattice parameters calculated by Velikokhatnyi et al.[38]. They also used DFT and VASP in their calculations, but with a different potential and a different cut-off energy for the plane wave expansion (see next sections). Table 3.1 also includes our and Velikokhatnyi et al.'s[38] calculated energy per formula unit. The calculated values for the *a*/*b*-axis and the *c*-axis are respectively 1.1% and 1.8% larger than the experimental values found by Sørby et al.[37]. There are several possible explanations for these differences: In chapter 2.1.3 we told that GGA corrects for most of the errors done by LDA. This is unfortunately not completely true, and underbinding is sometimes present; the Van der Waals forces are improperly described in DFT calculations; DFT is a ground state theory, which means that the calculations are performed at 0 K, while the experimental crystal axis were determined by high-resolution neutron and synchrotron X-ray diffraction at 295 K. Underbinding and improperly description of the Van der Waals forces clearly leads to enlarged lattice constants from our calculations compared to the experimentally obtained lattice constants. On the other hand, the temperature difference between the calculations and the experiment would obviously lead to reduced lattice constants from our calculations compared to the experimentally obtained lattice constants. This shows that there are several uncertainties involved in the calculations of the lattice constants, and that some of them cancel each other, thus giving results in good agreement with the experimentally obtained ones. Another possible explanation for the difference in the calculated and experimentally obtained lattice constants is that the calculations were performed on $Mg(NH_2)_2$, while the experimental structure was found for $Mg(ND_2)_2$. However, since it is commonly agreed upon that a hydride and its deuterated counterpart have almost identical structures, this is probably the case here too. Here it should be mentioned that the deuterium in the experimental structure found by Sørby et al. is for the sake of simplicity referred to as hydrogen in the remainder of this thesis, both in the text and in the tables.

The calculated lattice parameters are approximately 0.5% larger than those previously calculated [38], while the calculated energy per formula unit is 0.2% higher than that calculated by Velikokhatnyi et al.[38]. These differences may also stem from different reasons: The calculations were done with different cut-off energies; both ours and Velikokhatnyi et al.'s calculations were done within DFT using the GGA, but with different functionals, PBE and PW-91, respectively; Velikokhatnyi et al. used a different experimental structure as starting point for their relaxations, the structure found by Jacobs et al.[36]. Although the crystal axis Jacobs et al. obtained for $Mg(NH_2)_2$ is in agreement with Sørby et al., the H-N-H angles and the different interatomic distances have notable differences compared to Sørby et al.(see next section). And DFT calculations within the GGA approximation performed by Løvvik et al.[58] on a number of hydrides showed that different starting points gave variations in the size of the calculated lattice constants. This means that there are several possible explanations for the relatively small difference between our and Velikokhatnyi et al.'s calculated lattice constants.

Table 3.3 shows a comparison of the measured[36, 37] and calculated[38] interatomic distances. It is clear that our results are in very good agreement with those found by Sørby et al.[37], while Velikokhatnyi et al.'s[38] results exhibit notable differences compared to both Jacobs et al.[36] and Sørby et al.'s results. E.g. all the N-H distances calculated by us fall in the range between 0.95 and 1.07 Å. This is exactly the same as obtained by Sørby et al. These

results are somewhat longer than those reported by Jacobs et al. (0.87-0.94Å), while Velikokhatnyi et al.'s results deviate from all these results (1.02-1.03Å).

	Exp. (Jacobs)[36]	Exp. (Sørby)[37]	Calc. (this work)	Calc. (Veli.)[38]
$Mg(NH_2)_2$				
a(Å)	10.37	10.376	10.494	10.445
b(Å)	10.37	10.376	10.494	10.445
c(Å)	20.15	20.062	20.426	20.312
V(Å^3)	2167	2160	2249	2216
E/*Z*(eV)			-35.551	-35.622
Mg(32g)				
X	-	0.373	0.373	-
Y	-	0.105	0.109	-
Z	-	0.188	0.188	-
N1(16e)				
X	-	0.289	0.289	-
Y	-	0.750	0.750	-
Z	-	0.375	0.375	-
N2(16d)				
X	-	0.000	0.000	-
Y	-	0.000	0.000	-
Z	-	0.381	0.382	-
N3(32g)				
X	-	0.228	0.226	-
Y	-	0.488	0.486	-
Z	-	0.248	0.251	-
H1(32g)				
X	-	0.229	0.228	-
Y	-	0.813	0.806	-
Z	-	0.403	0.402	-
H2(32g)				
X	-	0.058	0.058	-
Y	-	0.953	0.951	-
Z	-	0.351	0.351	-
H3(32g)				
X	-	0.287	0.286	-
Y	-	0.434	0.430	-
Z	-	0.225	0.224	-
H4(32g)				
X	-	0.286	0.289	-
Y	-	0.537	0.539	-
Z	-	0.276	0.278	-

Table 3.1: Calculated and experimental crystal parameters for $Mg(NH_2)_2$ in addition to calculated energy pr. unit cell.

The H-N-H angles found by Jacobs et al.[36] had a rather large spread (104˚-130˚), while the spread in Sørby et al.`s[37] angles was much smaller (101˚-107˚) (see table 3.2). The angles found in our and Velikokhatnyi et al.`s[38] models were much more homogeneous (102.5˚-102.7˚ and 102.5˚-102.9˚, respectively). The geometry of a covalent unit such as amide ions is expected to be well defined and rather insensitive to chemical environment[37], so the

calculated angles probably gives a more accurate picture of the real structure at 0K than those found by experiments.

All in all, the differences between our calculated and Sørby et al.`s[37] lattice parameters, interatomic distances and H-N-H angles are small. The differences between the calculated and previously calculated[38] lattice parameters, energy per unit cell and H-N-H angles are even smaller, while the difference in the interatomic distances are notable. Since Velikokhatnyi et al.[38] used a rather low cut-off energy in their calculations, 520 eV compared to our 850 eV, we believe that our model resembles the real structure of $Mg(NH_2)_2$ better. The initial cut-off energy test presented in chapter 2 showed that for a cut-off energy of 550 eV, the total energy of the unit cell had only converged within 90 meV. This will obviously affect the accuracy of other calculated properties, including the interatomic distances. Therefore, it seems reasonable to use our calculated bulk structure for further calculations, as well as a basis for building of slabs and clusters.

Atoms	Angles (˚)			
	Exp. (Jacobs)[36]	Exp. (Sørby)[37]	Calc. (this work)	Calc. (Veli.)[38]
H_1-N_1-H_1	110.7	107.5	102.7	102.9
H_2-N_2-H_2	129.6	104.7	102.6	102.5
H_3-N_3-H_4	104.1	101.0	102.5	102.6

Table 3.2: Experimental and calculated H-N-H angles

Atoms	Distanses (Å)			
	Exp. (Jacobs)[36]	Exp. (Sørby)[37]	Calc. (this work)	Calc. (Veli.)[38]
Mg-N (min)	2.08	2.00	2.00	2.08
Mg-N (max)	2.09	2.17	2.17	2.10
Mg-H (min)	2.41	2.51	2.52	2.59
Mg-H (max)	2.63	2.68	2.68	2.64
Mg-Mg (min)	3.49	3.42	3.42	3.51
Mg-Mg (max)	3.51	3.47	3.47	3.53
N-H (min)	0.87	0.95	0.95	1.02
N-H (max)	0.94	1.07	1.07	1.03
H-H (min)	1.44	1.48	1.48	1.59
H-H (max)	2.35	2.19	2.19	2.31

Table 3.3: Selected experimental and calculated interatomic distances in $Mg(NH_2)_2$

3.2 Thermodynamics

The main thermodynamic parameter used to identify and classify hydrogen storage materials is the enthalpy of formation, which can be used to determine the heat of the overall hydrogen reaction. This heat affects the temperature of the reversible hydrogenation/dehydrogenation cycle. The difference in formation enthalpy before and after dehydrogenation is a measurement of the heat of the reaction. In this thesis we have focused on surface and cluster calculations, and therefore not prioritized these kinds of calculations.

As described in chapter 1, $Mg(NH_2)_2$ decomposes in two steps. The reactions are[59]:

$$3Mg(NH_2)_2 \rightarrow 3MgNH + 3NH_3 \rightarrow Mg_3N_2 + 4NH_3 \qquad (3.1)$$

To our knowledge, the crystal structure of MgNH is unknown. It is therefore not yet possible to calculate the enthalpy for each step of this reaction. But the average enthalpy of formation for $Mg(NH_2)_2$ per NH_3 was calculated by us. In VASP the enthalpy of formation, ΔH, is calculated by taking the difference in total electronic energy of the products and the reactants:

$$\Delta H = \sum_{products} E_p - \sum_{reactants} E_r \qquad (3.2)$$

This means that the enthalpy of formation for $Mg(NH_2)_2$ per NH_3 is:

$$\Delta H_{NH_3} = \left[3E\left(Mg(NH_2)_2\right) - E\left(Mg_3N_2\right) - 4E\left(NH_3\right)\right]/4 \qquad (3.3)$$

Here $E(Mg(NH_2)_2$ is the total electronic energy per unit of the relaxed bulk structure (-35.551 eV), $E(Mg)$ is the total electronic energy per unit for a Mg_3N_2 crystal (-8.399 eV), while $E(NH_3)$ is the total electronic energy per unit of NH_3 gas (-19.552 eV). From equation 3.3 the average enthalpy of formation for $Mg(NH_2)_2$ per NH_3 is calculated to be -483.5 kJ/mol. As far as we know, ΔH_{NH3} has never been reported before, neither by experiments nor calculations, so it is not possible to check if this value is in agreement with other results.

On the other hand, the enthalpy of formation for $Mg(NH_2)_2$ per H_2, ΔH_{H2}, has earlier been calculated by Velikokhatnyi et al.[38] from the following reaction:

$$Mg(NH_2)_2 \rightarrow Mg + N_2 + 2H_2 \qquad (3.4)$$

This was also done in this thesis by using equation 3.2. ΔH_{H2} was calculated to be -369.1 kJ/mol, which was in good agreement with the results obtained by Velikokhatnyi et al.[38] (-371.0 kJ/mol). ΔH_{H2} has also been obtained experimentally by Hu et al.[20]. However, since we did not consider the zero-point energy or the temperature dependent vibrational energy in our calculations, no direct comparison is possible. On the other hand, this was done by Velikokhatnyi et al. and their result was in good agreement with the experimentally obtained value, so we expect this to be the case for our result to.

3.3 Density of states

The electronic structure of a material contains important information about the characteristics of the material. By knowing the band structure of the electrons and the number of valence electrons in the unit cell, it is possible to determine whether the material is a metal, semi-conductor or an insulator. This section will give the results of the calculations of $Mg(NH_2)_2$'s density of states (DOS). The DOS, which is a measurement of the number of accessible electronic states at each energy level of the system, gives valuable information about the electronic band structure, the size of the band gap and the overlap between different bands.

The total and local density of states for $Mg(NH_2)_2$ are plotted in figure 3.3. For the Wigner-Seitz radii the atomic covalent radii of 1.30, 0.75 and 0.37 Å have been used for Mg, N and H respectively. Furthermore, the single particle orbitals were smeared by a Gaussian convolution with a width of 0.01 eV since this give an accurate description of the DOS (more detailed than with larger widths). The bottom picture shows the total DOS, while the other three plots show the local DOS for the different elements. Both the total and local DOS are plotted relative to the Fermi level, which in the ground state means that states with positive energy are unoccupied, while states with negative energy are occupied. The plot is very similar to that calculated by Velikokhatnyi et al.[38], validating the accuracy of our calculation of the DOS for $Mg(NH_2)_2$.

The DOS consists of three bands below the Fermi level, where none of the elements contribute to all three bonds in any significant way. The lower band is almost only populated by H *s* electrons and N *p* electrons, with a very small contribution of Mg *p* and *d* electrons. The mid band is only populated with Mg *s*, *p* and *d* electrons, while the upper band is mainly populated of Mg *s*, *p* and *d* electrons. There is also a major contribution of N *p* electrons, in addition to some N *s* and H *s* electrons, in the upper band. Between the upper valence band and the conduction band, there is a band gap of approximately 3.05 eV. This indicates that $Mg(NH_2)_2$ is a insulator, especially since DFT at the GGA level is known for notoriously underestimating the band gap[49], meaning that the actual band gap is probably larger. In the conduction band Mg once more contributes with all three kinds of electrons. N *p* electrons and H *s* electrons also populate the conduction band to some extent.

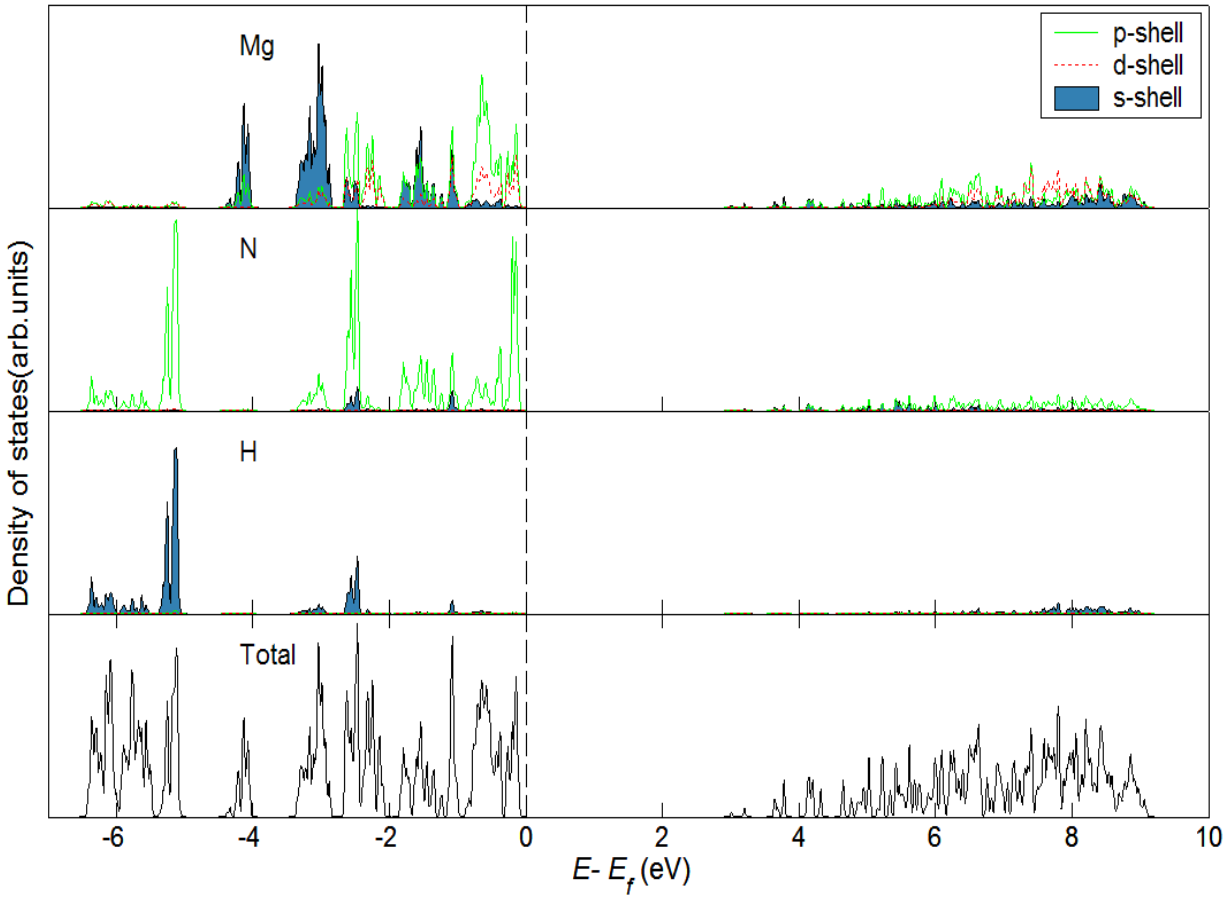

Figure 3.3: Total and local density of states for Mg(NH2)2

From the DOS it is also possible to observe a good correlation between the electronic states for N and H. There is a very low degree of correlation between the electronic states for Mg and H, while the overlap between the electronic states for Mg and N is better. This indicates that the material is held together by a bonding between the Mg and N atoms.

3.3.1 Charge density

When an accurate energy calculation is done in VASP, one can specify the parameters in the INCAR file, so that the CHGCAR file is included in the outfiles. The CHGCAR file contains the lattice vectors, atomic coordinates, the total valence charge density, and the PAW one-centre occupancies[41]. CHGCAR can be used to visualise the valence charge density in the unit cell, which can be a useful tool in the determination of the type of chemical bonds in the investigated material.

Figure 3.4 shows the valence charge density of $Mg(NH_2)_2$ in a chosen section of the unit cell. The figure shows that there is a high valence charge density around and between N and H, indicating covalent N-H bonds. There is a very low valence charge density around Mg. This, combined with the high valence charge density around the amide ions further indicates that there are ionic Mg-N bonds.

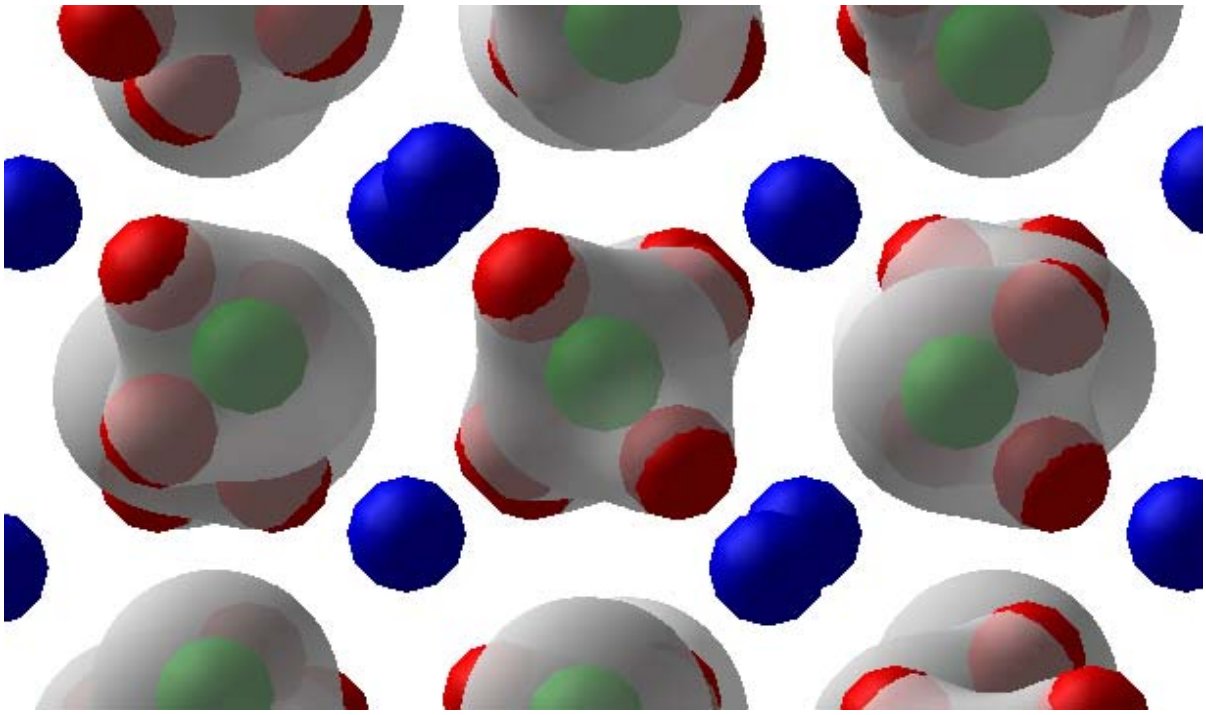

Figure 3.4: The charge density of $Mg(NH_2)_2$

Chapter 4

4 Surface calculations

This chapter presents the surface calculations done on $Mg(NH_2)_2$ during this thesis. First a brief description of the method used to do surface calculations in a plane wave code will be given, before the investigated surfaces will be discussed. At the end the calculated surface energies and the corresponding number of broken Mg-N bonds will be presented.

4.1 Surfaces

One of the most important issues in current hydride research is the understanding of the hydrogenation kinetics for the different hydrides. To describe this by theoretical tools, it is crucial to know the properties of various surfaces of the hydrides. And for hydrides with a nano-particle structure, like $Mg(NH_2)_2$, knowledge about the surface properties is even more important. Each nano-particle has many different surface facets, and by finding the surfaces that are most probable, essential information about the surface structure of the nano-particles can be gained. The most probable surfaces are the surfaces with the lowest surface energies.

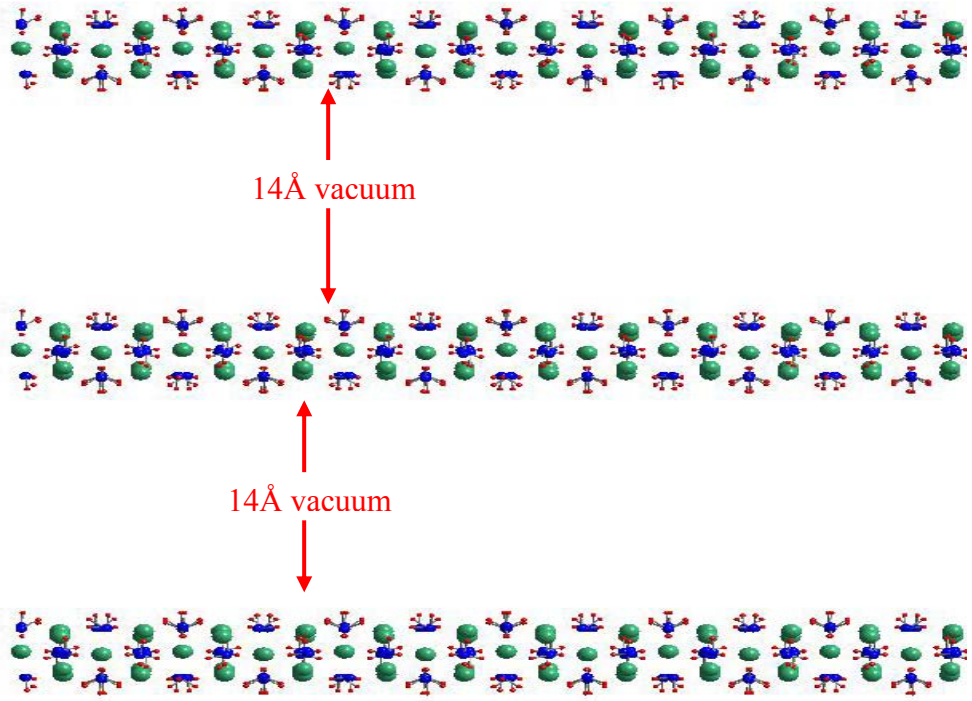

Figure 4.1: Illustration of how vacuum layers are inserted in the (110) planes of the unit cell of a 3 layer (110) slab. The structure is continuous in the other directions, i.e. in and out of the picture, and to the left and right hand side of the picture.

4.2 Initial surface calculations

To perform surface calculations in a plane wave code, where the unit cell ideally is repeated an infinite number of times in all directions, one has to insert a vacuum layer with the preferred orientation into the unit cell (see figure 4.1 for illustration). It is important that this vacuum layer is thick enough to prevent electronic interactions between the slabs, but small enough to avoid unnecessary computational time. To find a proper thickness, some initial surface calculations were performed. Figure 4.2 shows the energy per formula of $Mg(NH_2)_2$ as a function of the vacuum layer for four different two layer slabs. The difference in energy per unit for a vacuum layer from 8 Å to 10 Å is within 10 meV. To assure desired accuracy (within 5 meV) in the calculations, a vacuum layer of 14 Å was used in all further surface calculations.

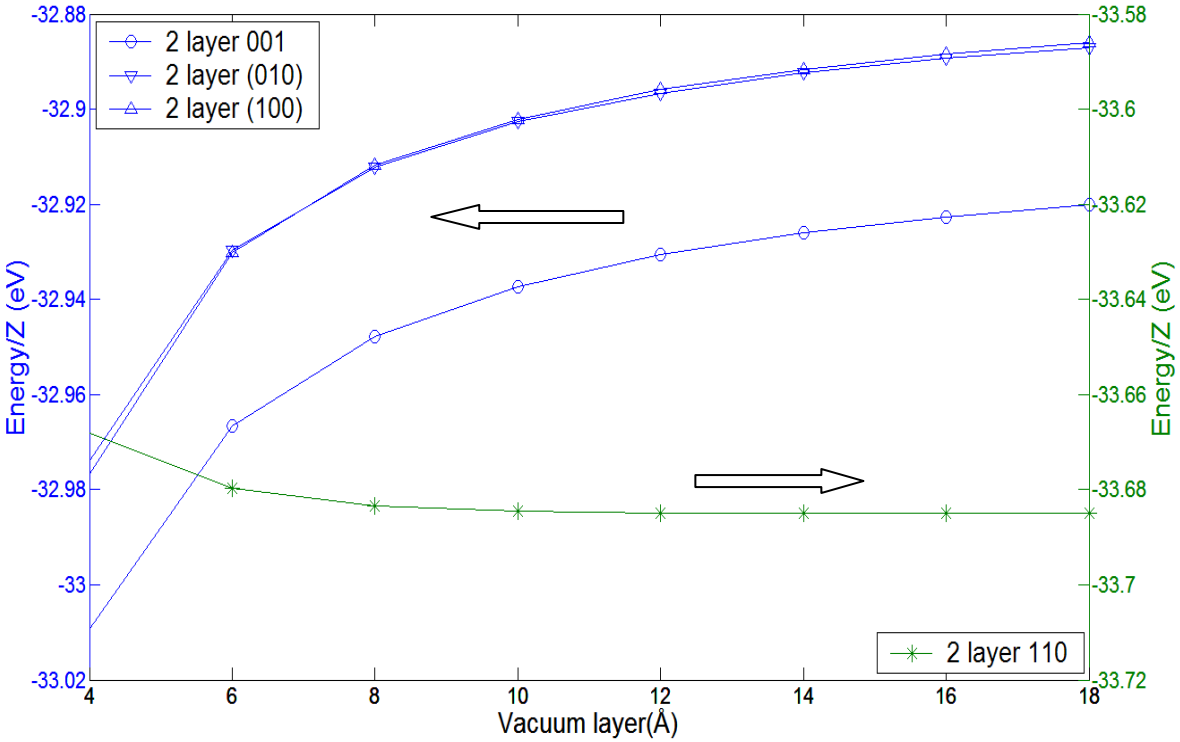

Figure 4.2: Energy per formula unit of $Mg(NH_2)_2$ as a function of vacuum layer on two different energy scales.

4.3 The investigated surfaces

Before starting with the actual surface calculations, we had to determine which surfaces to look at, and how many layers of atoms the slabs should consist of.

When a vacuum layer is inserted in the preferred plane of the unit cell, two surfaces are created. These two surfaces can either have the same structure, or different structures. In this thesis the calculations have been performed on four slabs where the two surfaces have different composition, the (100), (010), (001) and (112) slabs, and two slabs where the two surfaces have equal composition, the (110) and (012) slabs. It is here worth mentioning that the NH_2 units were always kept intact when the slabs were constructed, since we assumed

that a very high energy was needed for splitting these units (this was later confirmed during the cluster calculations (see chapter 6)). This means that only Mg-N bonds were broken during the construction of the slabs.

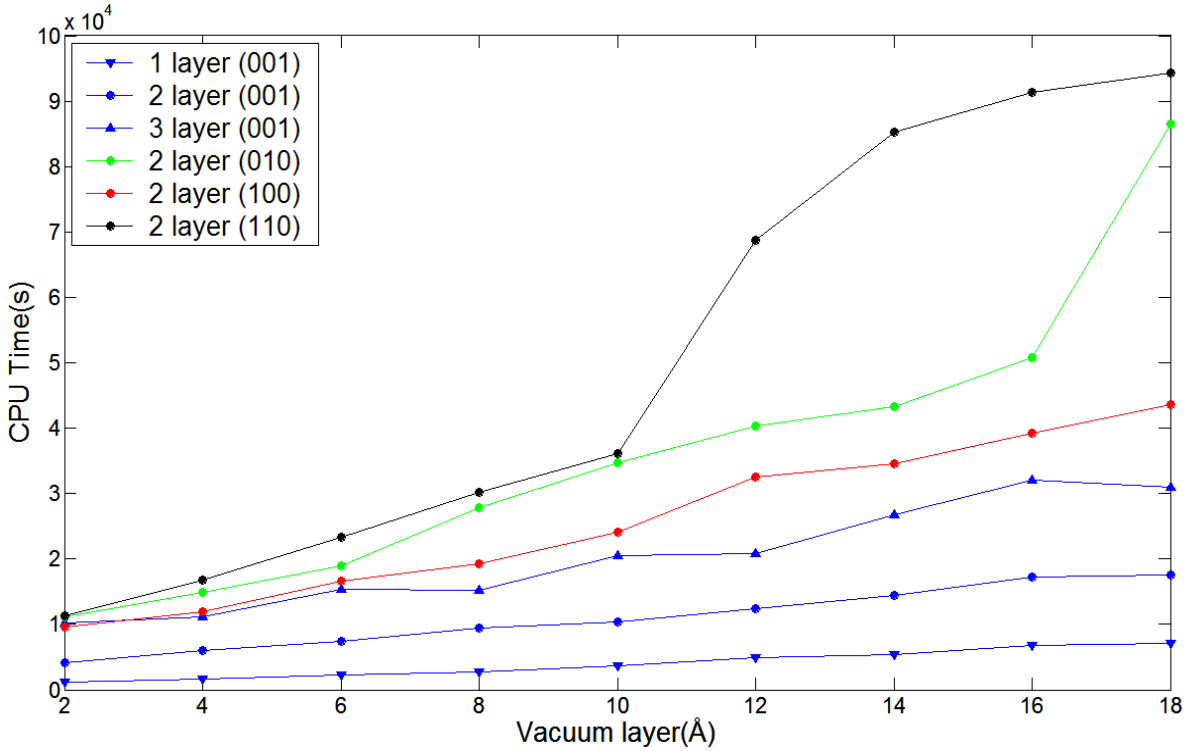

Figure 4.3: CPU time for total energy calculations as a function of the size of the vacuum layer for different slabs

Another important aspect to bear in mind during the construction of the slabs is how many atom layers they should consist of. By one atom layer, we mean a layer where a stoichiometric amount of both Mg atoms and amide ions is included. There are some advantages with a thick slab compared to a thin slab. One is that the increased number of atomic layers between the surfaces reassures that there will be no electronic interaction between the two surfaces on one slab. But a thicker slab also means that the calculations are more demanding, both with respect to time and memory. Figure 4.3. shows the CPU time for total energy calculations as a function of the size of the vacuum layer for different slabs. It shows that the CPU time for total energy calculations from a 1 layer (001) slab to 3 layer (001) slab increases from approximately 80 minutes to approximately 430 minutes, which is quite a severe increase. Despite this, 3 layer slabs have been used in all major surface calculations in this thesis to assure the desired accuracy in the results. So, when a slab is referred to in the remainder of this thesis, it is always a 3 layer slab if nothing else is mentioned. It is also worth mentioning that the surface calculations performed would most likely have had an even higher accuracy if we had used thicker slabs. But after several attempts on doing calculations on 4, 5 and even 6 layer slabs, in which none of them would run, we had to conclude that the computer facilities used during the work with this thesis were not powerful enough to do this kind of calculations on $Mg(NH_2)_2$. The limitation for the calculations seemed to be the memory consumption.

4.3.1 The slabs

In the three layer (100) slab there was inserted a vacuum layer in the [100] direction of the unit cell. This creates two (100) surfaces, one Mg rich and one amide (NH_2) rich. The initial unit cell of the (100) slab is shown in figure 4.4. Since one unit cell is relatively large, consisting of 168 atoms, it is computationally heavy to perform calculations on this slab.

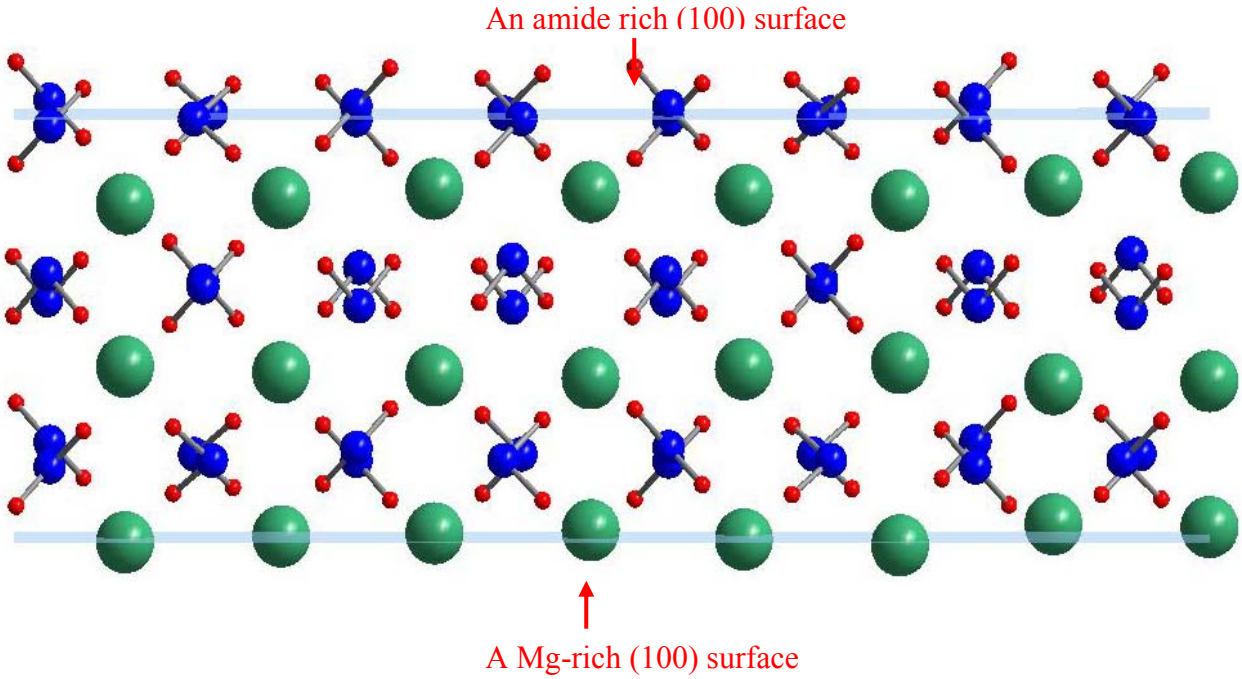

Figure 4.4: One unit of the initial 3-layer (100) slab viewed from the [010] direction.

The (010) slab was built in the same way as the (100) slab, but with the inserted vacuum layer in the [010] direction instead of the [100] direction. $Mg(NH_2)_2$ has a tetragonal unit cell, meaning that the (100) and (010) slabs are identical. This was confirmed from the total energy calculations performed on the initial (100) and (010) slabs. From figure 4.2 it is possible to see that the energy per unit of the initial (100) and (010) slabs were almost identical for different sizes of the vacuum layer. Because of this, only the (100) slab is further treated in this thesis, something which has saved valuable calculation time.

The (001) slab also has one Mg rich and one amide rich (001) surface. Here the vacuum layer was inserted in the [001] direction. This means that the vacuum layer was inserted in the *c*-direction of the unit cell of the bulk structure (see figure 3.1), and since $Mg(NH_2)_2$ has a tetragonal unit cell where the *c*-axis is almost twice as long as the *a*/*b* axis, inserting a vacuum layer in the [001] direction, strongly reduces the number of atoms in one unit cell for the (001) slab compared to the (100) and (010) slabs. Actually, the number of atoms in a 3 layer (001) slab unit cell is half of the number of atoms in a 3 layer (100)/(010) slab. This reduces the computational time significantly. From figure 4.3 it is possible to see that the CPU time for a total energy calculation on the 2 layer (100) slab is approximately 720 minutes, while it is reduced to approximately 240 minutes for a 2 layer (001) slab.

The composition of the (112) slab is somewhat different than that of the other slabs. As with the (100), (010) and (001) slabs, the two surfaces have different composition. But here the

two surfaces consist of a rather dense mix of both Mg atoms and amide ions compared to the homogeneous Mg/amide surfaces of the three first slabs. Moreover, two and two layers of atoms in the slab periodically curve upwards and downwards (see chapter 3.1 and figure 3.3). This curving indicates that two and two layers of atoms in the (112) orientation are more strongly bonded to each other than other neighboring atom layers. Because of this, a slab should ideally be constructed of an even number of atom layers since this makes it possible to construct the slab without breaking the strong bonds between every second layer. Nevertheless, since the computer facilities used in this thesis not were powerful enough for relaxing a 4-layer slab, and it in a 2-layer slab is a risk for electronic interaction between the two surface layers in the same slab, a 3-layer (112) slab has been used in the calculations. The slab was built by inserting a vacuum layer in the $[11\bar{1}]$ direction of the unit cell of the bulk structure.

Both the (110) and (012) slabs have two equal surfaces, both consisting of Mg atoms and amide ions. They were made by inserting a vacuum layer in the [110] and [021] direction of the unit cell of the bulk structure, respectively. From a computational point of view the (012) slab has an advantage compared to the (110) slab: One unit cell of a 3-layer (012) slab consist of 84 atoms, while one unit cell of the (110) slab consist of 168 atoms, making the calculations less expensive for the (012) slab.

4.4 Relaxation of the slabs

Relaxation of the slabs was done by ionic relaxation of the initial slabs. The structure and energy changes during relaxation give a good indication of which surfaces are the most stable and therefore the most frequently found surfaces in a real structure. The surfaces with the smallest structural changes are probably the most stable ones, since they resemble the experimental bulk structure the most.

Table 4.1 shows the change in structure and energy during relaxation. The (100) and (001) slabs, which both have one Mg rich surface and one amide rich surface, go through major structural and energy changes during relaxation. It is also clear that the (001) slab goes through smaller structural and energy changes than the (100) slab during relaxation. For the (100) slab the energy change during relaxation is 0.80 eV, while it is “only” 0.53 eV for the (001) slab. The average displacement of the atoms is 5.60 Å for the (100) slab, while it is reduced to 2.71 Å for the (001) slab. The reasons for this will be further discussed later in this chapter. Figure 4.5 shows the initial and relaxed (001) slab. From this figure it looks like Mg tends to withdraw from the surface and move into to the “bulk” of the slab during relaxation, while the amide ions move outwards, trying to cover the Mg atoms. It also looks like the H atoms on the surface amides have a tendency of pointing out of the surface. The (100) slab shows a similar tendency during relaxation, but with more severe changes.

The structure and energy changes for the (110) and (012) slabs, which both have surfaces that consist of Mg atoms and amide ions, are much smaller than the changes for the (001) and (110) slabs. The changes for the (110) slab are especially small during relaxation; The total energy change per formula unit is 0.46 eV, while the average displacement of the atoms is 0.83 Å. But the (012) also shows the same tendency. Figure 4.6 shows the initial and the relaxed (110) slab. Here too, it seems clear that Mg withdraws from the surface and moves into the “bulk” of the slab during relaxation, while the amide ions move outwards, with H pointing outwards, trying to cover the Mg atoms.

Slab	E_i(eV)	E_r(eV)	|ΔE|(eV)	Dr_{max}(Å)	Dr_{av}(Å)
(100)	-33.32	-34.12	0.80	5.60	3.72
(001)	-33.80	-34.33	0.53	2.71	2.37
(110)	-34.29	-34.75	0.46	0.83	0.30
(012)	-33.95	-34.71	0.76	2.07	0.63
(112)	-34.80	-35.00	0.20	0.44	0.11

Table 4.1: Structure and energy change during relaxation of the different slabs

The (112) slab experiences the smallest energy and structural changes during relaxation. Here, the total energy change per formula unit only is 0.20 eV, while the average displacement of an atom is no more than 0.11 Å. The initial and the relaxed (112) slab is shown in figure 4.7. Also, this time, Mg withdraws from the surface and moves into the "bulk" during relaxation, while the amide ions move outwards, with H pointing outwards, although the changes are less pronounced for the (112) slab compared to the other slabs.

In table 4.2 and 4.3 some selected interatomic distances and H-N-H angles are shown for the experimental structure[37], the calculated bulk structure and the different slabs. For the interatomic distances there are no clear trends for the different slabs compared to both experimental and calculated bulk structure. But it seems like the Mg-N and Mg-H distances are reduced for the "good" slabs compared to the "bad" slabs and the experimental and calculated bulk structure. Here, the (110), the (012) and the (112) slabs are so called "good" slabs, because their structure and energy changes was quite small during relaxation. The (100) and the (001) slabs are "bad" slabs, since their structure and energy changes were much more substantial during relaxation. Furthermore, it seems like the Mg-Mg and H-H distances have increased for the "good" slabs compared to the "bad" slabs and the bulk structure, while the N-H distances are much more homogeneous for both "good" and "bad" slabs compared to bulk structure. The reason why these changes in the interatomic distances appear is unclear. But an explanation for the more homogeneous N-H distance could be that the geometry of a covalent unit such as amide ions is expected to be well defined[37], which means that the N-H distances should be rather homogeneous (also mentioned in chapter 3.1.1).

When it comes to the H-N-H angles for the slabs compared to calculated bulk structure, they have a much larger spread (approximately 100˚-105˚) both for "good" and "bad" slabs compared to the bulk (approximately 103˚). This means that the H-N-H angles achieved from the slab calculations is actually closer to the experimental angles (approximately 101˚-108˚) than those obtained from the bulk calculations. This may be a coincidence, but a reasonable explanation could be that since the experimental structure was obtained from powder $Mg(NH_2)_2$, where each particle has many surface facets, the properties of the surface atoms and molecules of the experimental structure are probably better treated in calculations that take surfaces into account, than in calculations that do not. Slab calculations will thus give results that resemble the real structure better than the bulk calculations. Even though this is the case for the H-N-H angles, it was not the case for the different interatomic distances discussed in the last section. This means that the results obtained from different kind of calculations should be well analyzed to check if they are reliable. In the next chapters, another way of doing calculations will be presented, so called cluster calculations. Here, several surface facets will be taken into account during the calculations.

From the experience gained from the energy and structure changes during relaxation it seems like the (112) surface is the most stable surface, and therefore the surface that is most common in real $Mg(NH_2)_2$. It is also clear that the Mg atoms withdraw into the "bulk" of the structure where they are covered by amide ions with H atoms pointing outwards. The reason for these structural changes will be further discussed in chapter 5.

Atoms	Distanses (Å)						
	Exp. (Sørby)[37]	Bulk (this work)	(100)	(001)	(110)	(012)	(112)
Mg-N (min)	2.00	2.00	2.02	2.02	1.98	1.95	1.97
Mg-N (max)	2.17	2.17	2.16	2.18	2.15	2.15	2.16
Mg-H (min)	2.51	2.52	2.49	2.56	2.46	2.49	2.47
Mg-H (max)	2.68	2.68	2.78	2.71	2.66	2.67	2.73
Mg-Mg (min)	3.42	3.42	3.32	3.30	3.55	3.46	3.49
Mg-Mg (max)	3.47	3.47	3.57	3.59	3.65	3.62	3.67
N-H (min)	0.95	0.95	1.02	1.02	1.02	1.02	1.02
N-H (max)	1.07	1.07	1.03	1.03	1.03	1.03	1.04
H-H (min)	1.48	1.48	1.61	1.59	1.59	1.59	1.59
H-H (max)	2.19	2.19	2.29	2.29	2.34	2.33	2.34

Table 4.2: Selected experimental interatomic distances[37] and calculated interatomic distances for bulk and different slabs for $Mg(NH_2)_2$

Atoms	Angles (˚)						
	Exp. (Sørby)[37]	Bulk (this work)	(110)	(001)	(110)	(012)	(112)
H-N-H (min)	101.0	102.5	100.3	100.4	100.8	101.2	101.0
H-N-H (max	107.5	102.7	105.4	104.9	104.9	105.2	104.9

Table 4.3: H-N-H angles for the experimental structure[37], in addition to both the calculated bulk structure and slabs.

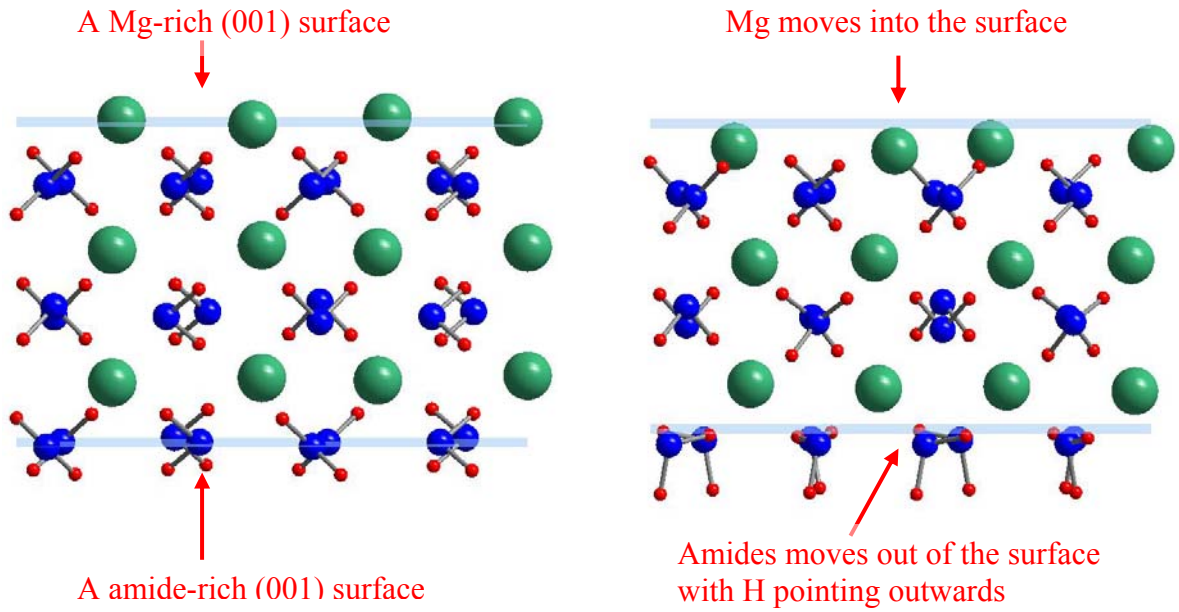

Figure 4.5: One unit cell of the initial (left hand side) and the relaxed (right hand side) (001) slab viewed from the [010] direction.

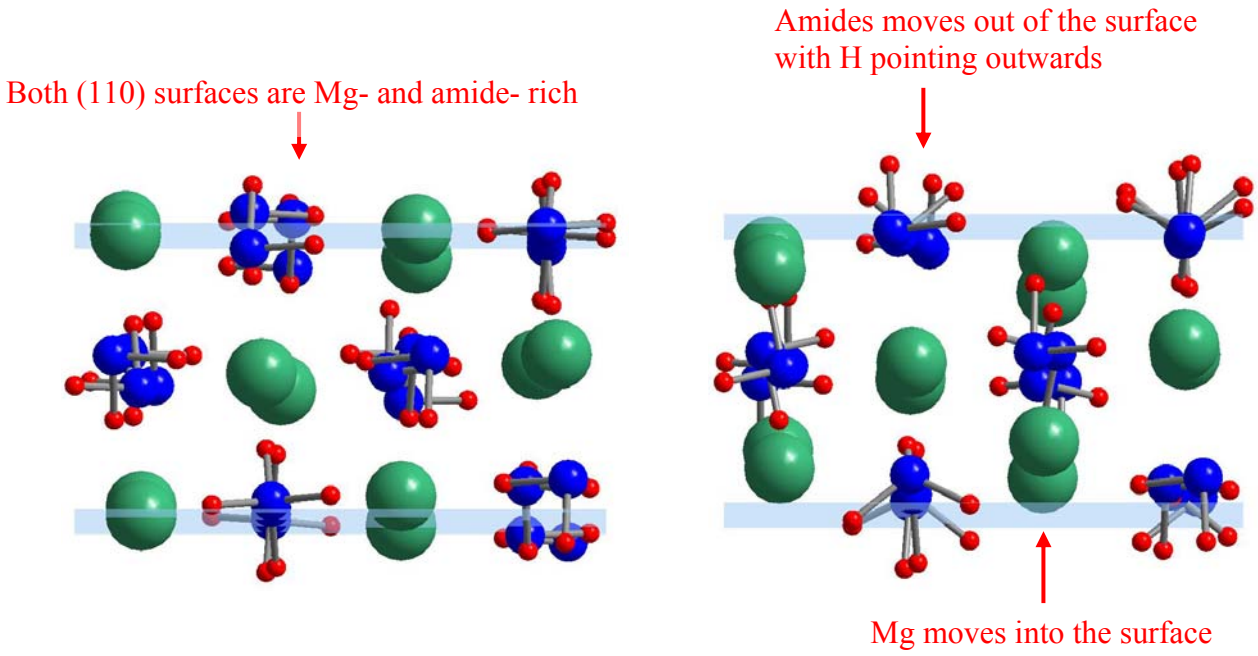

Figure 4.6: One half unit cell of the initial (left hand side) and the relaxed (right hand side) (110) slab viewed from the [001] direction.

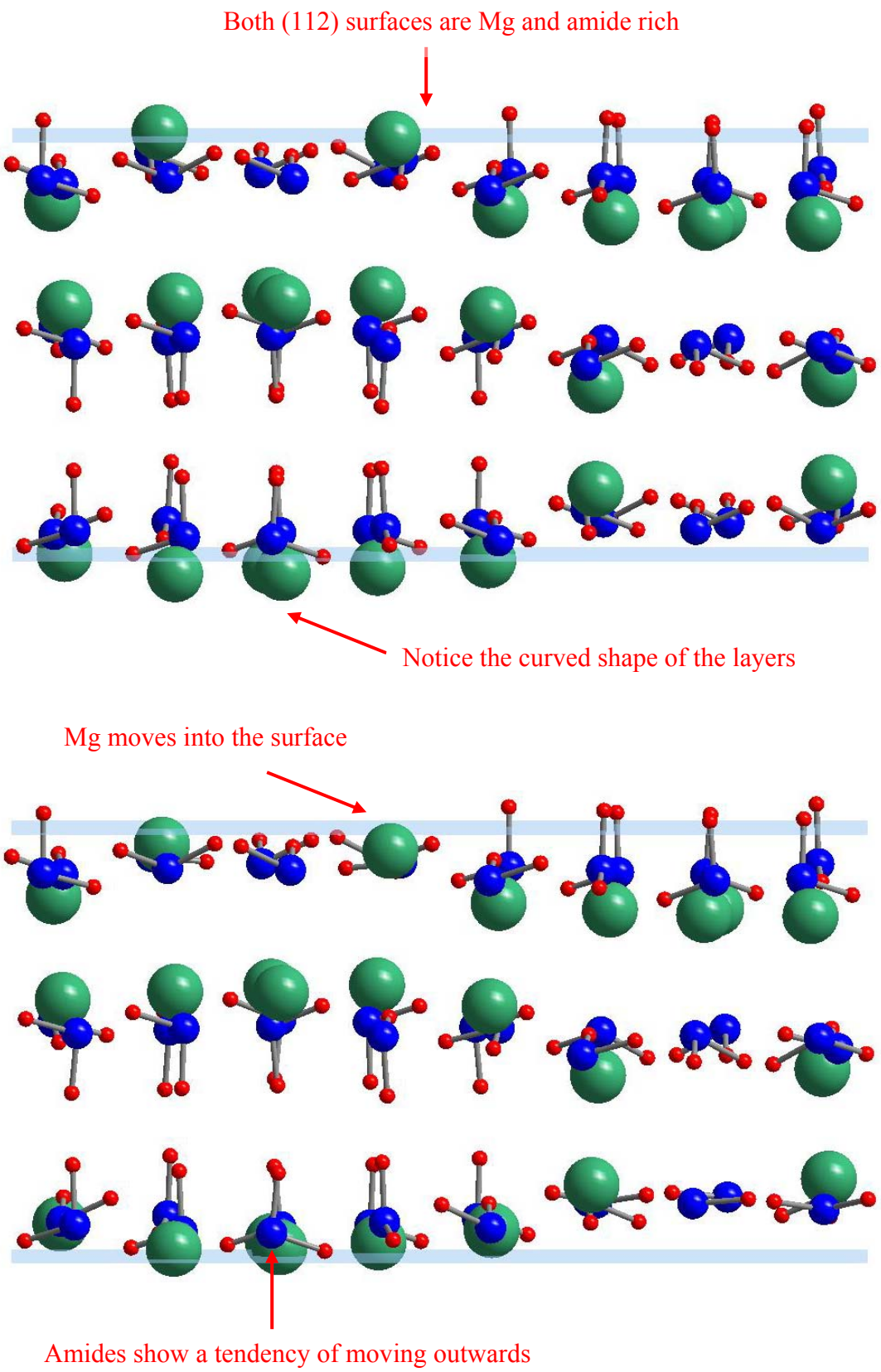

Figure 4.7: One unit cell of the initial (upper) and the relaxed (lower) (112) slab viewed from the [11$\bar{1}$] direction.

.

4.5 The surface energies

The surface energy is defined as half the energy needed to cut a crystal in two, and then separate the two parts at infinite distance. When this is done, two new surfaces are created. There are several ways to determine the surface energy[60, 61]. The intuitive formula for calculating the surface energy reads:

$$E_{surface}(N) = \frac{\left(E_{slab}(N) - NE_{bulk}\right)}{2A} \qquad (4.1)$$

Where $E_{surface}(N)$ is the surface energy, $E_{slab}(N)$ is the energy of a slab consisting of N formula units, E_{bulk} is the energy of one formula unit of the relaxed bulk structure and A is the area of slab surface per slab unit cell. It has been shown by Boettger[62] that the surface energy found from equation 4.1 diverges as N increases, since the bulk energy not necessarily fit exactly to the change in the slab energy as layers are added. A number of alternative ways of calculating the surface energy have thus been suggested[60, 61]. However, all of these methods require that there are energies, $E_{slab}(N)$, available for a number of different slabs (different number of layers) for each surface. And since we were not able to relax slabs consisting of more than three layers (see Chapter 4.3), we had to use equation 4.1 in our surface calculations. The problem with divergence of the surface energy, though, should be of no problem, since our slabs only have consisted of 3-layers (N_{max}= 24).

Table 4.2 shows the calculated surface energies and the number of broken Mg-N bonds during the cleavage of the bulk structure. Here, it is a bit surprising that the (110) surface has the lowest surface energy, although the (112) slab experienced much smaller changes in total energy per formula unit and structure during relaxation (see table 4.1). Furthermore, there is a good connection between surface energy and number of broken Mg-N bonds for all the surfaces, except for the (112) surface, which again has a high surface energy compared to the small number of broken Mg-N bonds. Generally it seems like the smaller the number of broken Mg-N bonds is, the lower surface energy. This is in agreement with the results obtained by Løvvik[63] on $LiAlH_4$, where he found that the most stable surfaces were the surfaces with the smallest number of broken Li-H bonds. A similar result was achieved by Frankcombe et al.[64] on $NaAlH_4$. They tested several different DFT methodologies, and the main tendencies were that there was a correlation between the number of broken Na–H bonds and the surface energies. Our results, in addition to earlier results[63, 64], clearly indicate that the number of bonds broken in the creation of a surface is an important parameter for the stability of the surface.

The reason why the (112) surface has higher surface energy than expected probably stems from several reasons. The first and most obvious one is of course that when the (112) slab was built, one of the surfaces was created by cleaving one of the two layered sheets/branches the bulk structure seems to be built up of. This cleavage probably cost more energy than the cleavage needed to create the other (112) surface (see chapter 4.3.1 for more details). Furthermore, the surface energy is the average of the two cleavage energies, so the first cleavage energy will clearly contribute to an increased surface energy. Another reason is that the surface energy is proportional to the inverse of the area of the created surface, which means that a surface which is densely packed (small area) will have higher surface energy than a surface with a low density of atoms (large area) when they consist of the same number of formula units, N. In this case, the surface area of the (110) slab is approximately one and a

half time larger than the surface area of the (112) slab, and since $N = 24$ in both cases, this clearly contributes to the low surface energy for the (110) surface compared to the (112) surface. If further calculations are performed on $Mg(NH_2)_2$, surface calculations on a (112) slab consisting of an even number of atom layers (only weak bonds broken) would clearly be very interesting.

Based on the surface energies it seems like the (110) surface is the most stable surface in $Mg(NH_2)_2$, and it will therefore probably be most frequently found. But it is closely followed in surface energy by the (012) and (112) surface. The (001) and (100) surfaces have much higher surface energies, and will probably occur much more rarely in real nano-particles of $Mg(NH_2)_2$ than the (110), (012) and (112) surfaces. It should here be mentioned again that all the other properties investigated of the different surfaces indicate that the (112) surface is the most stable one, and that some inconvenient considerations during the building of the (112) slab may have contributed to a higher surface energy than expected.

Surface	$E_{surface}(J/m^2)$	# broken Mg-N bonds per $Å^2$
(001)	1.34	0.061
(100)	1.22	0.059
(110)	0.50	0.049
(012)	0.53	0.052
(112)	0.57	0.022

Table 4.2: The surface energy and the number of broken Mg-N bonds for the various surfaces.

Chapter 5

5 Cluster Calculations

This chapter presents a new way of doing DFT calculations on complex hydrides in a plane-wave code, so called cluster calculations. Some advantages and disadvantages with the method are discussed, and the development of a suitable $Mg(NH_2)_2$ cluster model for further investigations is presented. At the end of the chapter a brief discussion of why the most stable surfaces of $Mg(NH_2)_2$ seem to exist of amide ions with H pointing outwards will be given.

5.1 A cluster approach

From experiments it is known that several complex hydrides, including $Mg(NH_2)_2$, are found as nano-crystalline powders (depending on how they are manufactured) . So far the majority of all DFT calculations done on these systems have been performed by using periodic calculations, either on the bulk structure or by using slab models, or a combination of the two methods. One exception is the calculation done by Marashdeh et al.[65, 66] on Ti-doped $NaAlH_4$, where they used a semi-spherical cluster as a model for a nano-sized $NaAlH_4$ particle. Some of the advantages with cluster calculations compared to bulk and slab calculations are:

(i) The real material exhibits a range of surface facets. The bulk structure has no surfaces, while a slab only has two surfaces. This would probably lead to lack of information in results obtained from bulk and/or slab calculations. A cluster model though, contains both edges and corners and would probably resemble the actual situation more closely than the other methods.

(ii) There are no strict boundary conditions in cluster calculations. This means that it is possible to check if it is energetically favorable to remove atoms or molecules/iones from one specific surface position compared to another. This is obviously not possible in bulk calculations, and only to a small extent in slab calculations.

(iii) It is easier to describe defects. In bulk and slab calculations the lattice constants have to be equal throughout the structure, while it in cluster calculations are possible to present different lattice constants locally in the clusters. This means that it is possible to investigate more types of defects with cluster calculations than with bulk and slab calculations.

Based on the fact that $Mg(NH_2)_2$ can be found as a crystalline powder, we think that a cluster approach will lead to new and important information about the properties of $Mg(NH_2)_2$, and complex hydrides in general. Despite the advantages of this approach, the use of cluster models is not straightforward. One thing is that the calculated properties of the material of interest probably, to some degree, depend on both the size and the shape of the cluster. The cluster model we found most promising (see section 5.3) was quite small, only 1 nm in

diameter, while real nano-particles have a diameter ranging from 60 nm and larger. This is clearly a limitation with cluster models in general and something to bear in mind when analyzing results from cluster calculations. Nevertheless, our ambition is to understand the properties of complex hydrides and similar materials better, so all realistic approaches should be explored. To approach this kind of problems using cluster models is certainly one of the methods which could help provide significant improvements in our knowledge about the properties of complex hydrides.

5.2 The cluster models

Construction of the first cluster models was done simultaneously with the slab calculations. At that moment we had no knowledge about the typical structural changes during relaxation for $Mg(NH_2)_2$, so many of the first models had considerable energy and structure changes during relaxation. Even so, these calculations gave important information about how further cluster calculations most efficiently could be performed in VASP, with support calculations in ADF. This was essential knowledge since it has, as far as we know, never been reported concerning cluster calculations on complex hydrides in a plane-wave code earlier. The cluster calculations performed by Marashdeh et al.[65, 66] were done in ADF which uses a linear combination of atomic orbitals (LCAO) as basis set.

The building of the cluster models used in VASP was done in a similar way as the building of the slab models used in the surface calculations (see figure 5.1 for an illustration). However, this time there was inserted a vacuum layer in all directions, instead of just one. Tests to check the size of the vacuum layers were done in the same way as for the slab calculations (see Chapter 4.2), and a vacuum layer of 12Å was found to give the desired accuracy (the total energy of one formula unit had converged within 5 meV). By using this approach we were able to model a nano-sized particle with approximately no electronic interaction with any of the other nano-sized particles in a plane-wave code. When the cluster calculations were done in ADF, the insertion of a vacuum was not necessary, since ADF, as already mentioned, uses a LCAO basis set, which is localized.

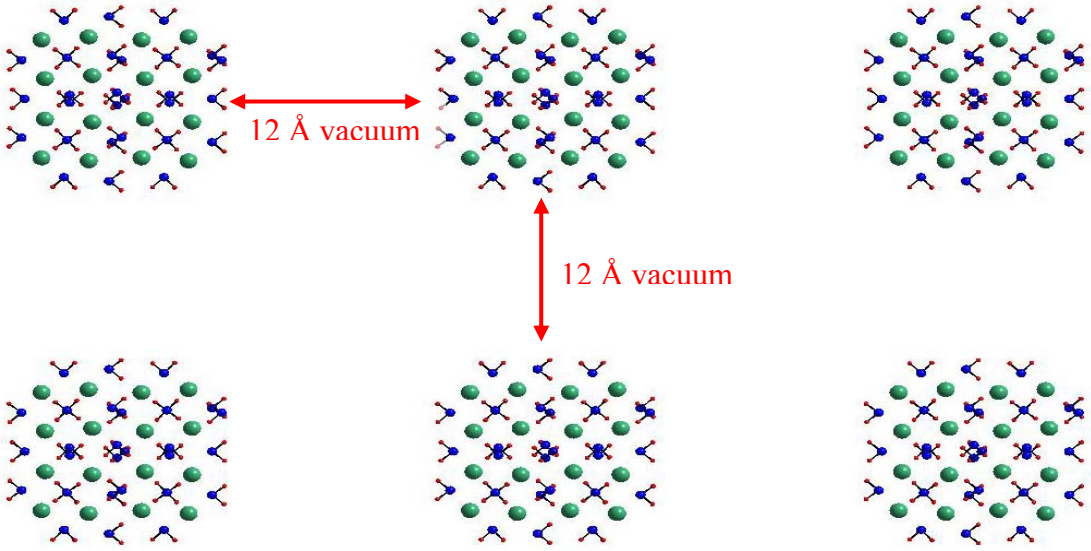

Figure 5.1: Illustration of how vacuum layers are inserted in all directions for cluster calculations in a plane-wave code. A vacuum layer of 12 Å is also inserted in the direction in/out of the picture.

The first clusters investigated had many different shapes and sizes. Most of them had a spherical form, but half spheres and other forms were also tested. Figure 5.2 shows the total energy per formula unit as a function of the cluster shape/size for some of the initial clusters tested. *Z*6Mg means that the cluster consist of 6 formula units of $Mg(NH_2)_2$ with Mg as the center atom in the cluster. This notation is valid for all the clusters mentioned in this thesis. The figure shows that there is no clear connection between size, shape and total energy per unit formula, which is somewhat surprising. Intuitively, we would have expected that larger clusters would have been closer in energy per formula unit to bulk structure than smaller clusters, since the large clusters have a higher fraction of "bulk" structure compared to surface structure compared to the small clusters. This higher fraction of "bulk" structure was therefore expected to give the large clusters properties more similar to the bulk structure than the small clusters. Since this is not the case, there are obviously other properties than the size that greatly influence the properties of a cluster. This will be further discussed in this chapter and the next chapter. However, one thing that is apparent from these first cluster calculations is that the *Z*22N and *Z*30Mg clusters have lower energy per unit formula than the other clusters, even though the reason remains unknown.

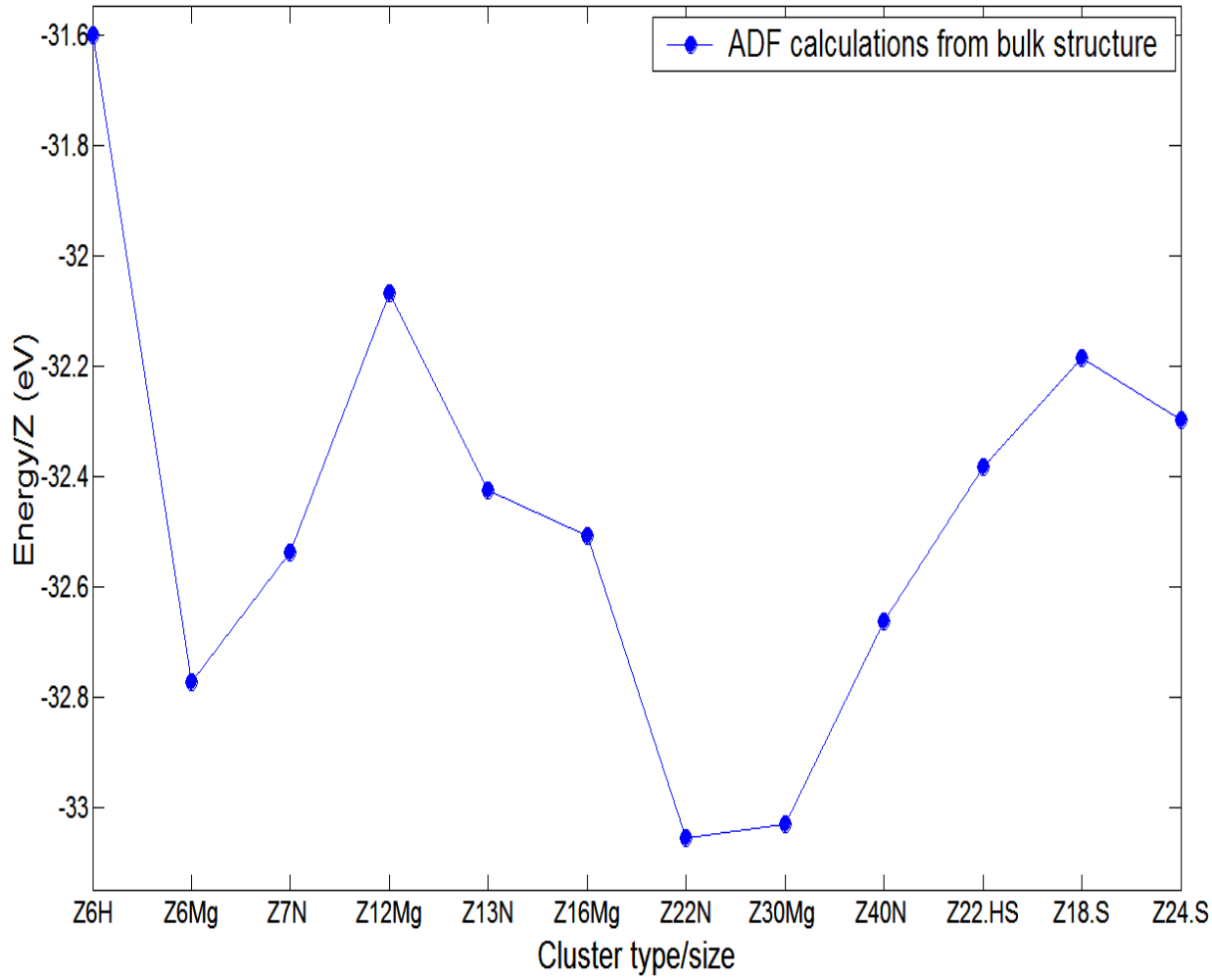

Figure 5.2: Total energy per formula unit for clusters of different size and shape. The notation is as explained in the text. Exceptions are the Z22.HS, the Z18.S and Z24.S, where the first cluster has a half spherical shape and the last two clusters have no clear geometric shape. The two last ones are made in a way such that as much as possible of the (110) and (012) orientations of the bulk structure are present at the surfaces of the clusters.

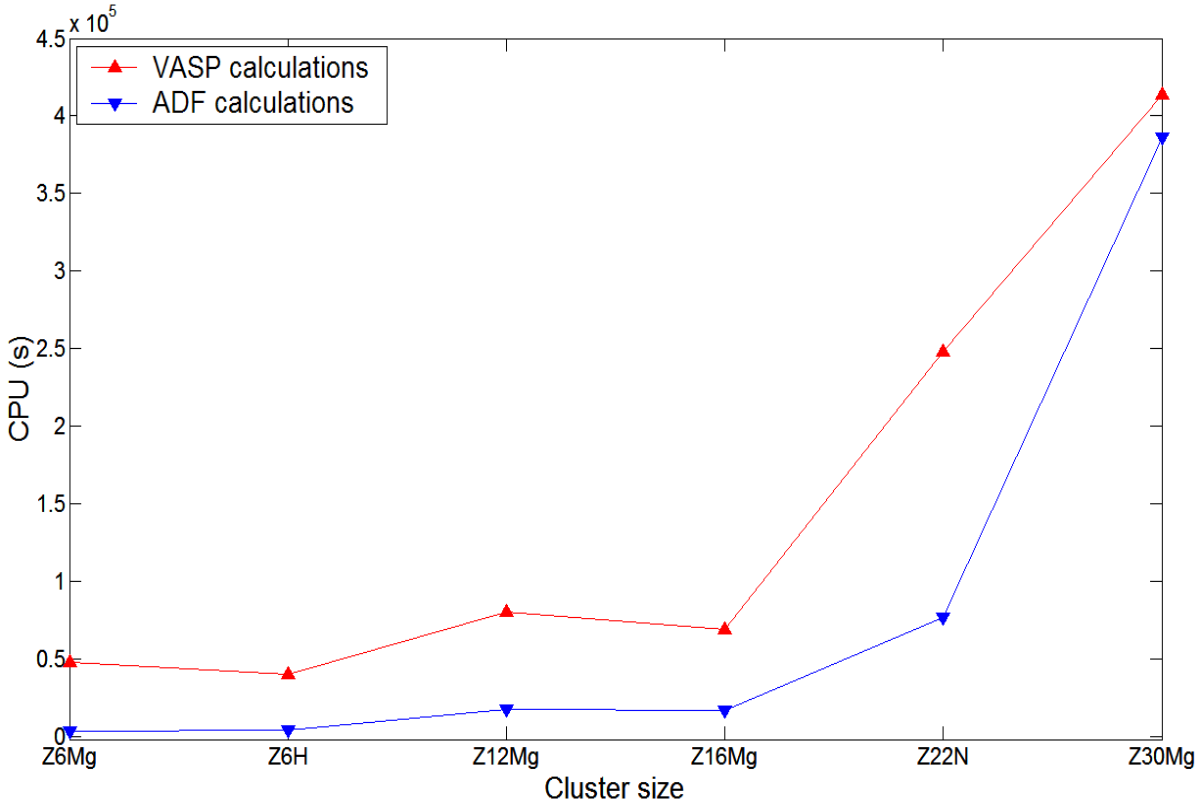

Figure 5.3: The CPU time for total energy calculations as a function of cluster size for calculations done in both VASP and ADF

Figure 5.3. shows the CPU time for total energy calculations in both VASP and ADF as a function of cluster size. All the calculations have been performed on the same-super computer and with the same number of nodes. From this figure it is obvious that total energy calculations on cluster models are faster in ADF than VASP, but when the cluster size increases, the difference in CPU time decreases. Furthermore, the CPU time is quite low for cluster sizes up to 16 formula units. However, for a *Z*22N cluster the CPU time is 4 times as long for both ADF and VASP as for the *Z*16N cluster. And for the *Z*30Mg cluster the CPU time doubles compared to the CPU time for *Z*22Mg for VASP, while it increases 6 times for ADF. Based on these results it is reasonable that our final cluster model should consist of no more than 15 to 20 formula units, since this will save us valuable calculation time. Here, it is also worth mentioning that the memory consumption during relaxation of the large clusters (consisting of more than 22 formula units), was a substantial problem, and often the main limitation for these types of calculations.

5.2.1 Relaxation of the initial cluster models

The first cluster models relaxed were small, consisting of only 6 formula units. The reason for this was that the CPU time used in the calculations performed on these clusters was small compared to larger clusters. The small clusters gave indications about what kind of structure changes which would occur during relaxation, what kind of calculations that should be performed using which software, and they served as a test to check if ADF and VASP gave agreeable results. The two softwares are expected to do this since they are both based on DFT,

and they both employ the PBE functional at the GGA level (see chapter 2.2.3 and 3.3.1 for further details).

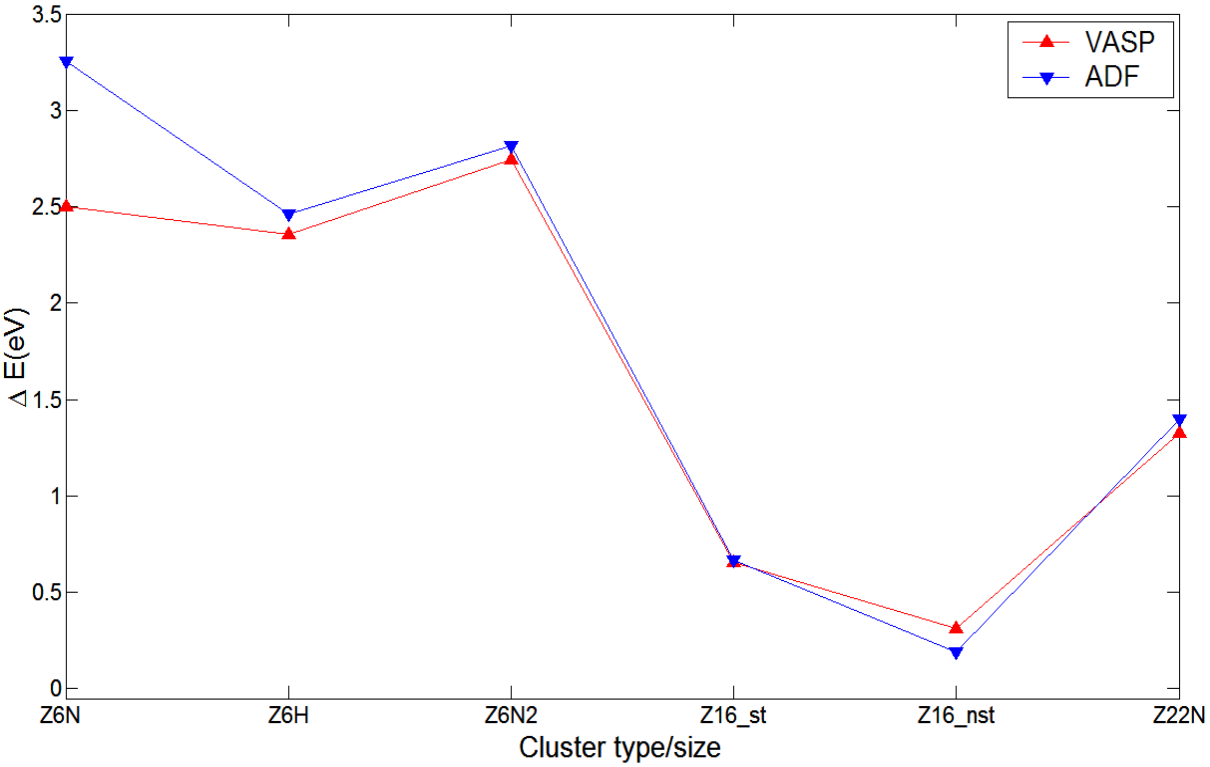

Figure 5.4: Change in total energy per formula unit during relaxation for different clusters in VASP and ADF.

The first important property found during the *Z*6 calculations, was that VASP was unable to relax the initial clusters directly. Both quasi-Newton and conjugate-gradient algorithms were tried during the relaxations in VASP, but none of the methods were able to relax the initial clusters directly. The problem seemed to be that the maximum force between two atoms in the cluster converged at a very high value, approximately 0.5-1.0 eV/Å. The reason for this probably was that the calculations got trapped in local energy minima, and were unable to break "free" from these local minima, and continue against a global minimum. In ADF though, by using the quasi-Newton algorithm, there was no problem relaxing the initial clusters. Furthermore, when the clusters that already had been relaxed in ADF were used as initial clusters in VASP, the relaxation there also went well. Based on this experience all further cluster relaxations done in this thesis were done by the following method: The initial cluster was first relaxed in ADF. Then this cluster was used as an initial cluster in VASP and relaxed again there. This relaxed cluster is the final cluster, and was used in all further calculations and measurements of the cluster. There are several possible explanations for why the initial clusters are relaxed in ADF and not in VASP, and this is an interesting property of DFT software's within the GGA approximation which clearly could be more thoroughly investigated. This was not done in this thesis, since we found the work of developing a good and stable cluster model for $Mg(NH_2)_2$ of more importance. But one obvious reason is certainly that ADF is a molecular code, using a localized basis set (LCAO), which has often proved to give the most reliable results for molecules and molecular-solids ($Mg(NH_2)_2$ is a molecular-solid, see chapter 3.3). VASP, on the other hand, uses a plane wave (PWs) basis

set, where the atomic region is not as well described, but the description of the interstitial region between the atoms is much better. Here, one obvious question arises: *Why use VASP at all in the cluster calculations? ADF clearly handle cluster calculations on $Mg(NH_2)_2$ better than VASP*. The answer to this question is that the use of VASP in the cluster calculations makes it easier to compare the results from the cluster calculations with the results obtained from bulk and slab calculations, since then all the INPUT parameters, except the POSCAR and KPOINT files, are identical. Furthermore, we thought that VASP had the ability to perform nudge elastic band (NEB) calculations (see chapter 6.2 for more details), something not possible in ADF at the time being. NEB calculations gives valuable information about the energy barriers involved in the removal of different elements from the investigated system, something we valued high. Last, but not least, we wanted to check if it was possible to perform cluster calculations in a plane wave code, and if the results provided from these calculations were reliable.

To further check if ADF and VASP give agreeable results, the energy change per formula unit during relaxation has been plotted for several clusters in figure 5.4. The figure shows that the energy change during relaxation is approximately equal for the clusters in both ADF and VASP. The difference in the energy change for the *Z*22N cluster in VASP and ADF is for example within 40 meV, so ADF and VASP provide agreeable results when it comes to the energy change per formula unit during relaxation.

Figure 5.5 shows an initial and a relaxed *Z*6Mg cluster. From these figures it is possible to see the main problem with small clusters; the structural changes are substantial during relaxation. Figure 5.6 shows the initial and relaxed *Z*22N cluster. Also here, the structural changes are considerable during relaxation, so it is clear that bigger is not necessarily better. A closer look at the figures reveals that the structural changes have the same tendency as the structural changes which the slabs had during relaxation (see chapter 4.4). The Mg atoms withdraw into the surface with amide ions covering them. The H atoms on the amides point outwards from the surface.

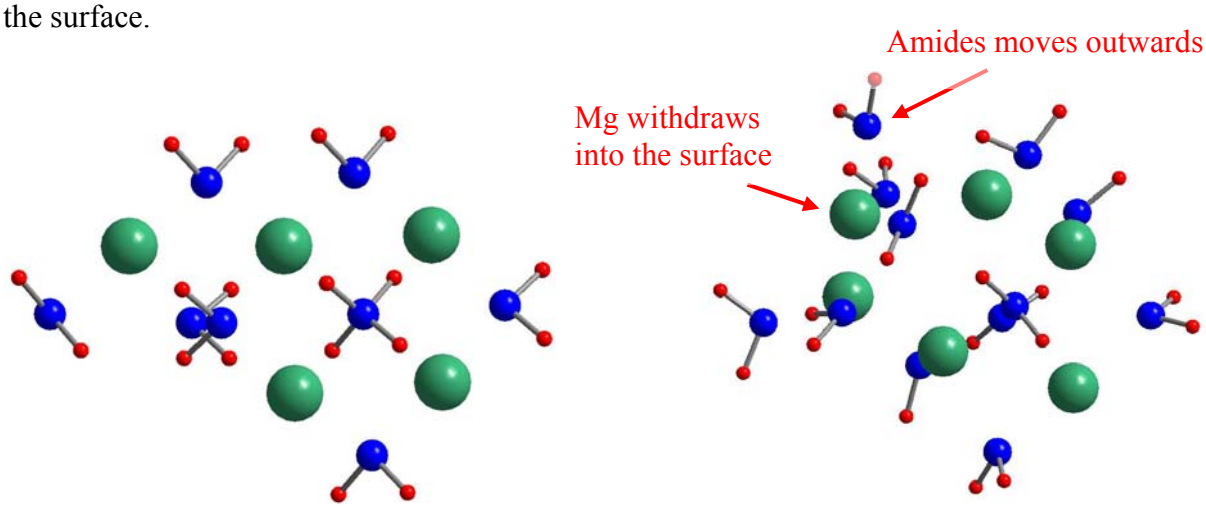

Figure 5.5: The initial, the left hand figure, and the relaxed, the right hand figure, *Z*6Mg cluster.

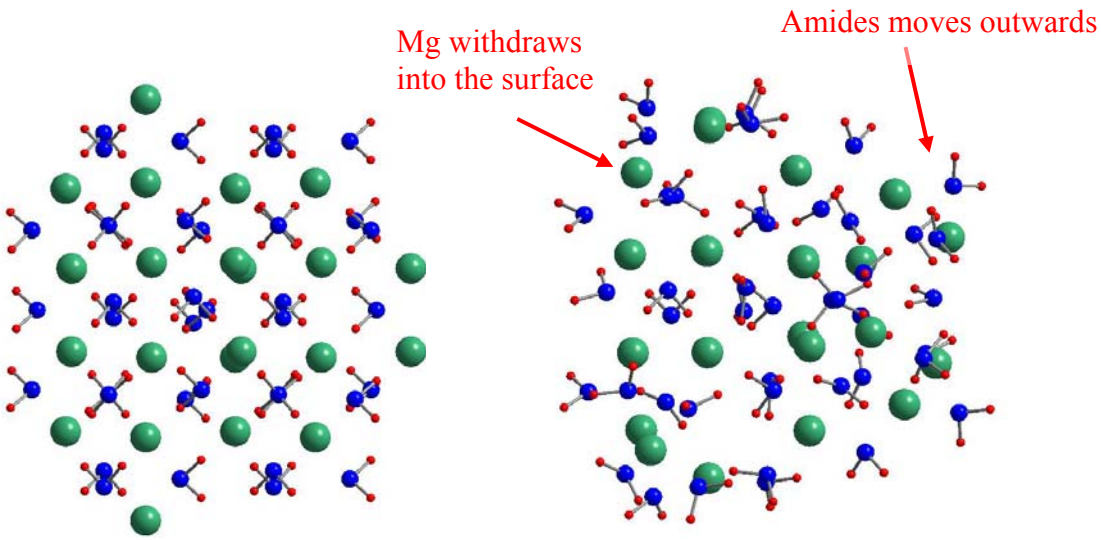

Figure 5.6: The initial, left hand figure, and the relaxed, the right hand figure, *Z*22 cluster.

5.3 The Z16 clusters

As mentioned at the end of the last section: A stable cluster, or a cluster with small structural changes during relaxation, should have Mg atoms that are concealed inside the cluster, while the surfaces of the cluster should consist of amide ions with H atoms pointing outwards. It was not easy to build such a cluster. One problem was not making it to large. To large means that the cluster consists of more than 20 formula units, since these clusters are much more demanding in both time and memory consumption (see chapter 5.2). Another difficulty involved in the construction of a stable cluster was to conserve the symmetry from the bulk structure in the initial cluster. The cluster that met these requirements best was the $Z16_{st}$ cluster, which consisted of 16 formula units $Mg(NH_2)_2$. But there was one problem with the $Z16_{st}$ cluster; it had an uneven distribution of the amides. The initial and relaxed $Z16_{st}$ clusters are shown in figure 5.6. From these figures it is clear that there are considerable structural changes in the upper right hand corner of the cluster, which is exactly where there was an uneven distribution of the amides. The structural change in the rest of the $Z16_{st}$ cluster is quite small, so we are definitely closing in on a good cluster model.

We then built a non-stoichiometric cluster, the $Z16_{nst}$ cluster. In this cluster one of the amides in the $Z16_{st}$ cluster is removed, which makes a more even distribution of the amides. The initial and relaxed $Z16_{nst}$ clusters are shown in figure 5.7. From these figures and table 5.1, where the structural and energy change during relaxation are shown, it is obvious that $Z16_{nst}$ is the most stable cluster when it comes to structural and energy change during relaxation. But there is one problem: $Z16_{nst}$ has a formal charge of +1. This leads to the following question: *Is it possible to obtain reliable results in calculations performed on a charged cluster?* A positive argument is that we only remove neutral atoms from the cluster. Nature does not care about formal charges, so we let the cluster figure out which charge it will have on its own. The use of a charged cluster will be further discussed and tested in this and the next chapter.

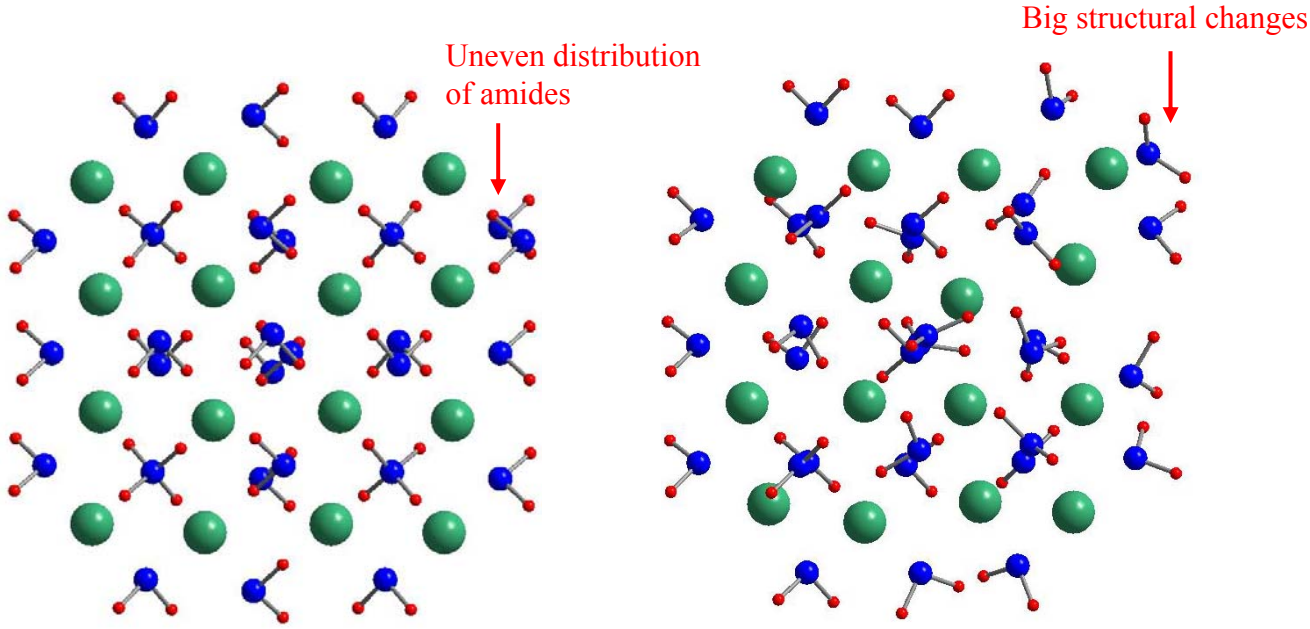

Figure 5.7: The initial (left hand figure) and the relaxed (right hand figure) $Z16_{st}$ cluster.

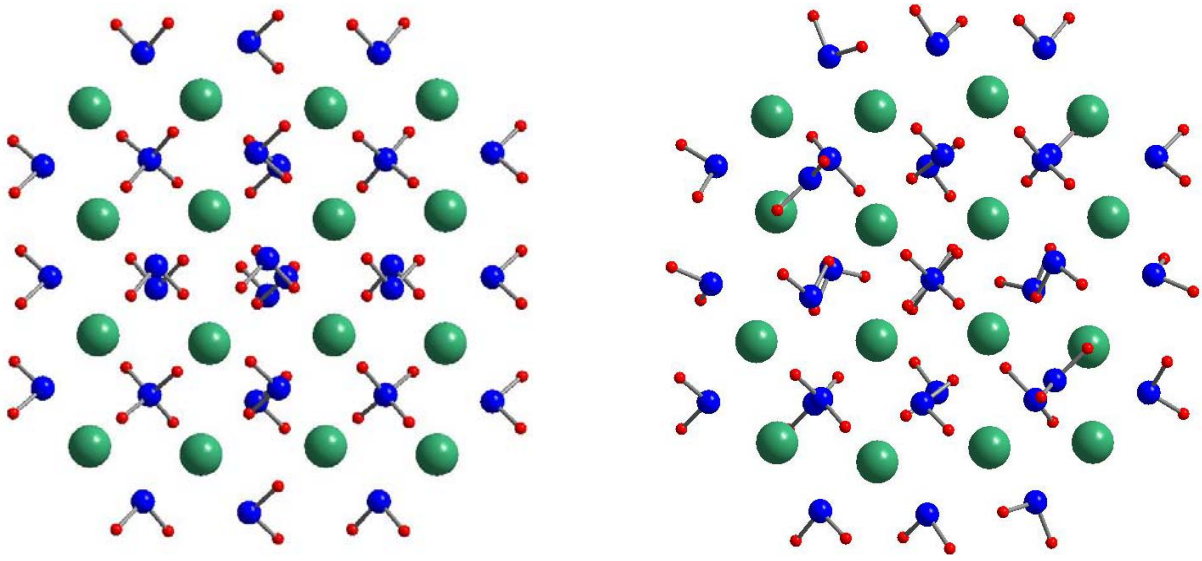

Figure 5.8: The initial (left hand figure) and the relaxed (right hand figure) $Z16_{nst}$ cluster.

Cluster	E_i(eV)	E_r(eV)	|ΔE|(eV)	Dr_{max}(Å)	Dr_{av}(Å)
*Z*6	-33.37	-34.51	1.14	2.69	1.11
$Z16_{st}$	-34.47	-34.95	0.48	3.02	0.63
$Z16_{nst}$	-33.61	-33.84	0.23	1.83	0.44
*Z*22	-33.67	-35.08	1.41	4.49	1.17

Table 5.1: Structural and energy change during relaxation of different clusters.

In table 5.2 and 5.3 some selected interatomic distances and H-N-H angles are shown for the experimental structure[37], the calculated bulk structure, the (110) slab and for the $Z16_{st}$ and the $Z16_{nst}$ clusters. The interatomic Mg-N, Mg-H, Mg-Mg and H-H distances have a larger spread for the clusters than for the bulk and the (110) slab. Furthermore, the N-H distances are more homogeneous for clusters than for the bulk, a result also obtained for the slab calculations. The reason why these changes in the interatomic distances appear is unclear. An explanation for the more homogeneous N-H distance could be that the geometry of a covalent unit such as amide ions is expected to be well defined[37], which means that the N-H distances should be rather homogeneous (also mentioned in chapter 3.3.1 and 4.4). It is also worth mentioning that the interatomic distances in the $Z16_{nst}$ cluster have a smaller spread than the interatomic distances in the $Z16_{st}$ cluster, again showing that the $Z16_{nst}$ cluster is closer in structure to bulk than the $Z16_{nst}$ cluster.

The H-N-H angles for the clusters have an even larger spread than the angles obtained for the (110) slab. This means that the H-N-H angles for the clusters are much closer to the H-N-H angles obtained experimentally by Sørby et al.[37] than those found for the calculated bulk structure and the (110) slab. Especially the H-N-H angles for the $Z16_{nst}$ cluster were close (102˚-108˚, compared to 101˚ to 108˚). Possible reasons for this were discussed in chapter 4.4.

Atoms	Distances (Å)				
	Exp. (Sørby)[37]	Bulk (this work)	(110) slab	$Z16_{st}$	$Z16_{nst}$
Mg-N (min)	2.00	2.00	1.98	1.96	2.01
Mg-N (max)	2.17	2.17	2.15	2.21	2.17
Mg-H (min)	2.51	2.52	2.46	2.44	2.47
Mg-H (max)	2.68	2.68	2.66	2.79	2.72
Mg-Mg (min)	3.42	3.42	3.55	3.21	3.21
Mg-Mg (max)	3.47	3.47	3.65	3.50	3.49
N-H (min)	0.95	0.95	1.02	1.02	1.02
N-H (max)	1.07	1.07	1.03	1.05	1.05
H-H (min)	1.48	1.48	1.59	1.60	1.60
H-H (max)	2.19	2.19	2.29	2.59	2.57

Table 5.2: Selected experimental interatomic distances[37] and calculated interatomic distances for the bulk, the (110) slab and for the $Z16_{st}$ and the $Z16_{nst}$ clusters.

Atoms	Angles (˚)				
	Exp. (Sørby)[37]	Bulk (this work)	(110) slab	$Z16_{st}$	$Z16_{nst}$
H-N-H (min)	101.0	102.5	100.8	102.2	102.2
H-N-H (max	107.5	102.7	104.9	108.7	107.8

Table 5.3: H-N-H angles for the experimental structure[37], in addition to both the calculated bulk structure, the (110) slab and the $Z16_{st}$ and the $Z16_{nst}$ clusters.

5.3.1 Comparison of the density of states for the *Z*16 clusters, the (110) slab and the bulk structure

One method to check if the $Z16_{nst}$ cluster can give reliable results in further calculations is to check if its density of electronic states (DOS) is in agreement with the DOS for the $Z16_{st}$ cluster, the (110) slab and the bulk structure. Figure 5.9 shows the total DOS for all these structures and there are clearly some major differences between them:

(i) The band gap is pushed down in energy for the slab and the clusters compared to the band gap for the bulk structure. The reason for this is that the slab and the clusters have surfaces. These surfaces will be occupied by electrons, which will give the slab and the clusters metallic properties, and therefore push the band gap down in energy.

(ii) There are occupied states in the band gap of the slab and the clusters. These occupied states are probably one of the reasons why complex hydrides with nano-particle structure have better kinetics than complex hydrides with larger particles (in addition to increased surface).

The most important knowledge to be gained from figure 5.9 though is that the DOS for the clusters have the same tendency as the DOS for the 110 slab, and the DOS for the $Z16_{nst}$ cluster is almost identical with the DOS for the $Z16_{st}$ cluster. Based on this and the small structural and energy changes found during relaxation, we consider $Z16_{nst}$ to be a good cluster model for further calculations.

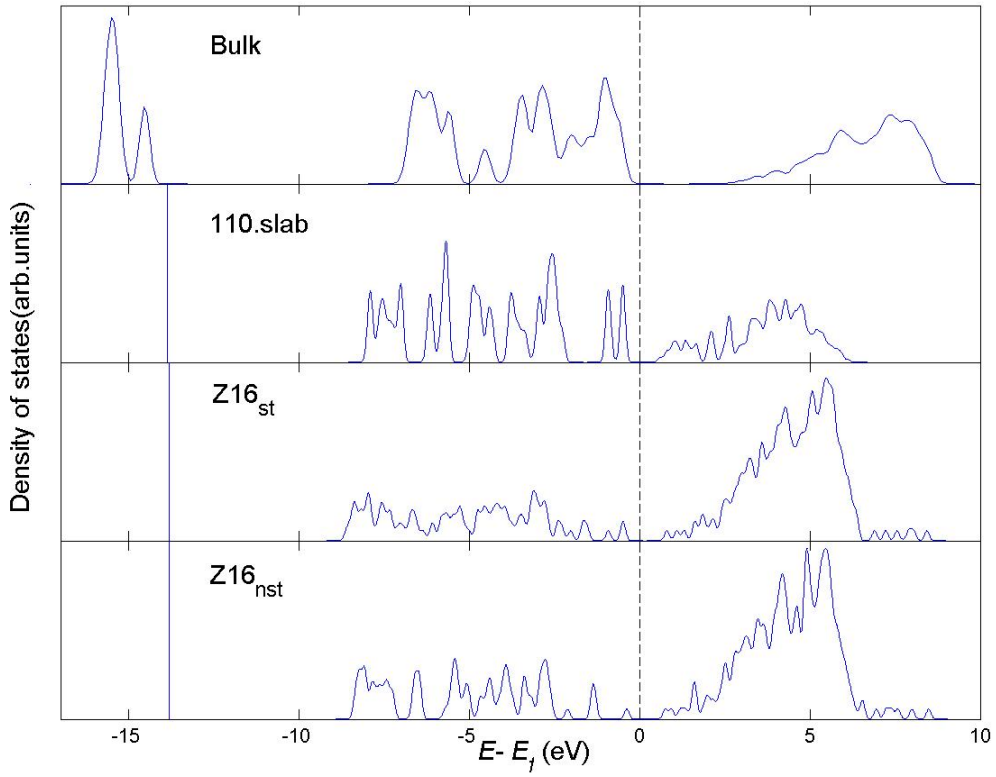

Figure 5.9: Total DOS for the bulk structure, the 110 slab, the $Z16_{st}$ and the $Z16_{nst}$ (the single-particle orbitals were smeared by a Gaussian convolution with a width of 0.2 eV, since this provides more smooth graphs).

5.4 Dangling bonds

Figure 5.10 shows a selected part of the initial and relaxed (110) slab. Here it is clear, as already mentioned, that Mg withdraws from the surface while the amides moves outward covering Mg during the relaxation. Furthermore, H atoms in the surface amides point out of the surface after the relaxation. *Why does this happen?* A possible explanation is that when Mg and N atoms are present on the surface, they will have dangling bonds. A dangling bond occurs when an atom is missing a neighbor to which it would be able to bond. H only makes strong bonds (covalent bonds) with N and this terminates N's dangling bonds. Moreover, if H points out of the surface, the amides are oriented in such a way that only weak bonds (Van der Waals bonds) are broken. Mg's dangling bonds will probably contribute to the Mg-N bonds between surface Mg and N belonging to the first atom layer underneath the surface (see figure 5.10). These bonds are therefore strengthen and the interatomic distance between Mg-N reduced (from table 4.2 and 5.2 it possible to see that the minimal interatomic Mg-N distances for the slabs and clusters are reduced with approximately 0.05Å compared to the bulk structure. An exception is the $Z16_{nst}$ cluster, where the minimal interatomic Mg-N distance approximately is the same as for the bulk structure). The role of dangling bonds on the surface of $Mg(NH_2)_2$ will be further discussed in the next chapter.

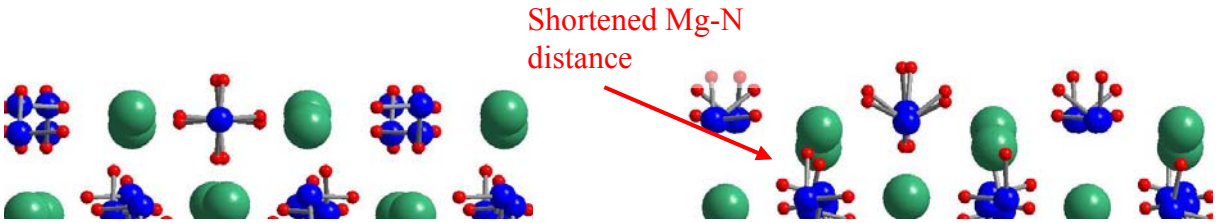

Figure 5.10: A selected part of the initial and relaxed (110) slab.

Chapter 6

6 Decomposition of clusters

In this chapter the energies involved in the removal of H, H_2, NH_2 and NH_3 from three different $Mg(NH_2)_2$ clusters will be presented. These calculations have made it possible to explore one of the advantages in the use of cluster models, i.e. if it is energetically more favorable to remove an atom or molecule from one specific surface position compared to another specific surface position. The activation energies, or the energy barriers, involved in the removal of H_2 and NH_3 molecules from $Mg(NH_2)_2$ have also been examined.

6.1 Decomposition of the $Z16_{nst}$ cluster

H, H_2, NH_2 and NH_3 have been removed from different surface positions of the $Z16_{nst}$ cluster to see if some positions are more energetically favorable than others. Only thermodynamical equilibrium states (local energy minimums) have been considered. This means that when an atom or ion/molecule was removed from the relaxed $Z16_{nst}$ cluster, the new cluster was relaxed again. The new total energy of the cluster, E_{new}, was then added to the energy of free gas of the atom or ion/molecule removed, E_{gas}. The new total energy was then compared to the initial energy of the cluster, $E_{initial}$, to check how large the energy difference ΔE between the two equilibrium states was. This can be expressed in the following equation:

$$\Delta E = E_{initial} - E_{new} - E_{gas} \qquad (6.1)$$

The energies obtained from these calculations are not necessarily very accurate, but we think they will show the main tendencies of the system, e.g. whether a "corner" amide has stronger N-H bonds than a "center" amide (the difference between a "corner" and a "center" amide is shown in figure 6.1). Some reasons for the inaccuracy in these calculations are: the clusters are small compared to the unit cell and the real nano-particles (see chapter 5.1), meaning that some properties can be very specific for the investigated cluster (very local); the initial cluster has a formal charge, which may affect the energy involved in the removal of atoms and molecules. To compensate for some of these errors we also checked the energies involved the removal of different elements from the $Z16_{st}$ cluster and a new cluster, called the $Z16_{nst2}$. The initial $Z16_{nst2}$ has two amide molecules less than the $Z16_{st}$ cluster, meaning that it has a formal charge of -2. These additional calculations gave an indication whether the tendencies we observed for the $Z16_{nst}$ also occurred for clusters without a formal charge, and for clusters with a different formal charge.

6.1.1 Removal of monoatomic hydrogen

First an H atom was removed from two different surface positions: a “corner” position and a “center” position (see figure 6.1). Table 6.1 shows the energy involved in the removal of atoms and molecules from the different clusters. From this table it is clear that it is energetically favorable to remove an H atom from a “corner” amide compared to removing it from a “center” amide. This was the case for all the three clusters. The energy cost was 0.40 eV, 1.06 eV and 1.47 eV smaller when H was removed from a “corner” amide compared to a “center” amide for the $Z16_{st}$, the $Z16_{nst}$ and the $Z16_{nst2}$ clusters, respectively. For all three clusters the H atom was removed from the same amide (same position). The large energy difference involved in the removal of an H atom from the same position from the different clusters probably stems from the difference in the initial formal charge of the clusters. However, other sources of errors also occur. Among them are different magnitudes of structural change compared to bulk structure. Both the $Z16_{st}$ and $Z16_{nst2}$ clusters have more substantial structural changes than the $Z16_{nst}$ cluster (because of a more uneven distribution of the amides, see chapter 5.3 for the $Z16_{st}$ cluster). Therefore, the energies obtained from the calculations performed in the $Z16_{nst}$ cluster probably give the most reliable results. Furthermore, the energy difference for the thermodynamical equilibrium states for the initial clusters and the new clusters plus the energy of 1/2 H_2 gas, i.e. ΔE, was quite large (ranging from 0.59 eV to 1.92 eV, see table 6.1).

The reason why it is easier to remove an H atom from a “corner” amide than a “center” amide most likely is that the “corner” amide is more strongly bonded to Mg than the “center” amide. This is the case since the Mg atom in the “corner” position has more dangling bonds than the Mg atom in the “center” position, making the “corner” Mg-N bond stronger. The strong Mg-N bond will thus weaken the N-H binding, making it easier to remove H from the “corner” amide.

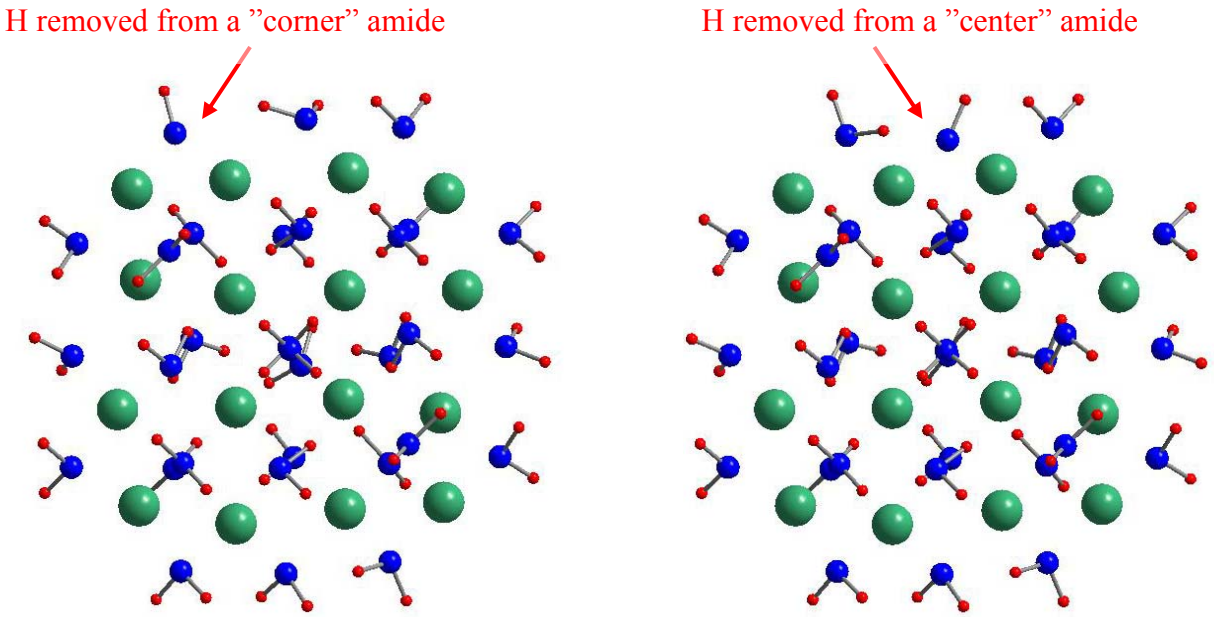

Figure 6.1: The figure on the left hand side shows when a H atom is removed from a ”corner” amide of the $Z16_{nst}$ cluster, while the figure on the right hand side shows when a H atom is removed from a “center” amide of the $Z16_{nst}$ cluster.

6.1.2 Removal of an hydrogen molecule

H_2 was then removed in two different ways from the $Z16_{nst}$ cluster. For H_2.1, the H atoms were removed from two different amides, while for H_2.2 both H atoms were removed from the same amide (see figure 6.2). As expected, H_2.1 was energetically favorable compared to H_2.2 (a difference of 1.12 eV was found, see table 6.1). In the H_2.1 cluster there were two imide molecules left after removal of the H_2 molecule, while there was only one N atom without any H bonds left in the H_2.2 cluster. This difference was not tested for the other clusters, since we assumed that this property is general.

The energy difference for the thermodynamic equilibrium states for the initial clusters and the new clusters plus the energy of H_2 gas, i.e. ΔE, was quite large (from 3.61 eV to 4.80 eV, see table 6.1). So, it is very unlikely that pure H_2 gas will be released from $Mg(NH_2)_2$.

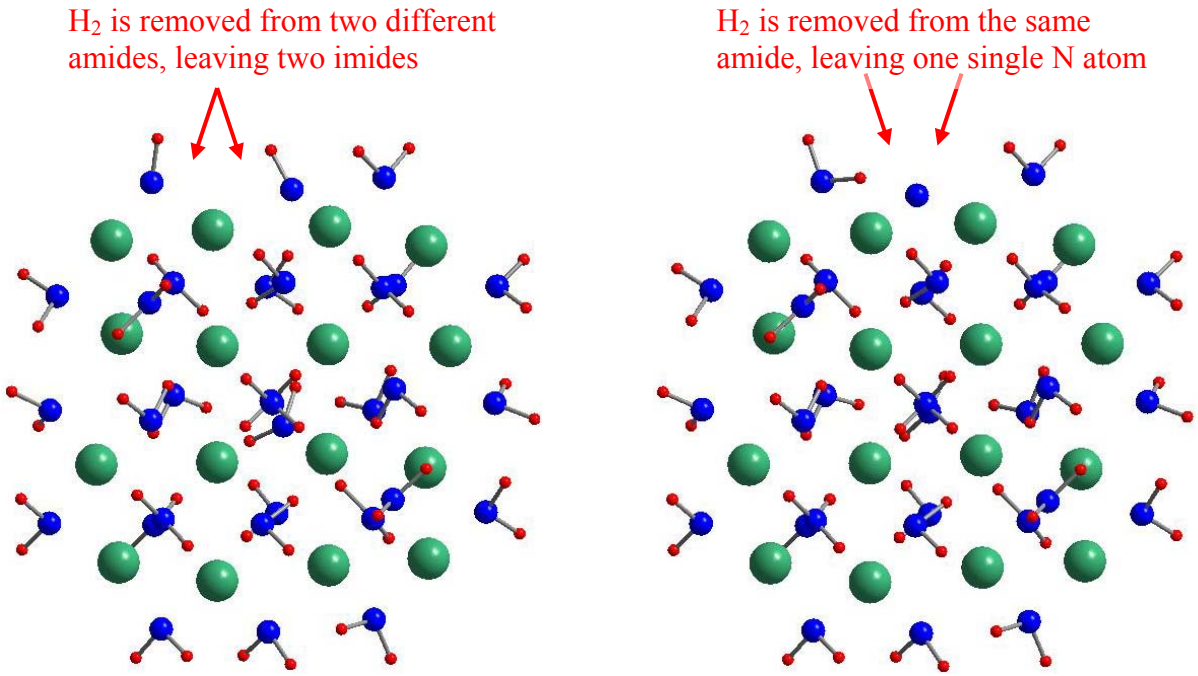

Figure 6.2: The figures shows the two different ways H_2 have been removed from the $Z16_{nst}$ cluster.

6.1.3 Removal of an amide ion

An amide ion was then removed from both a "corner" and a "center" position for the different clusters (see figure 6.3 for the $Z16_{nst}$ cluster). Here it was energetically favorable to remove the "center" amide compared to the "corner" amide. The difference was 0.32 eV, 0.29 eV and 0.62 eV for the $Z16_{st}$, $Z16_{nst}$ and $Z16_{nst2}$, respectively (see table 6.1). This confirms what we already assumed from the experience gained from the removal of monoatomic H: the "corner" amide is more strongly bonded to Mg than the "center" amide.

The energy difference for the thermodynamical equilibrium states for the initial clusters and the new clusters plus the energy of NH_2 gas (from 1.09 eV to 1.71 eV, see table 6.1) was notably smaller than the energies involved in the removal of H_2 gas. The results for the

different clusters were also in better agreement compared with the results obtained from the removal of H and H_2 gas. The reason for this is unclear and further investigations of these properties may be of interest, although it has not been given priority in this thesis. A scheme that shows the lowest energies involved in the removal of H, H_2 and NH_2 from the different clusters is shown in figure 6.5.

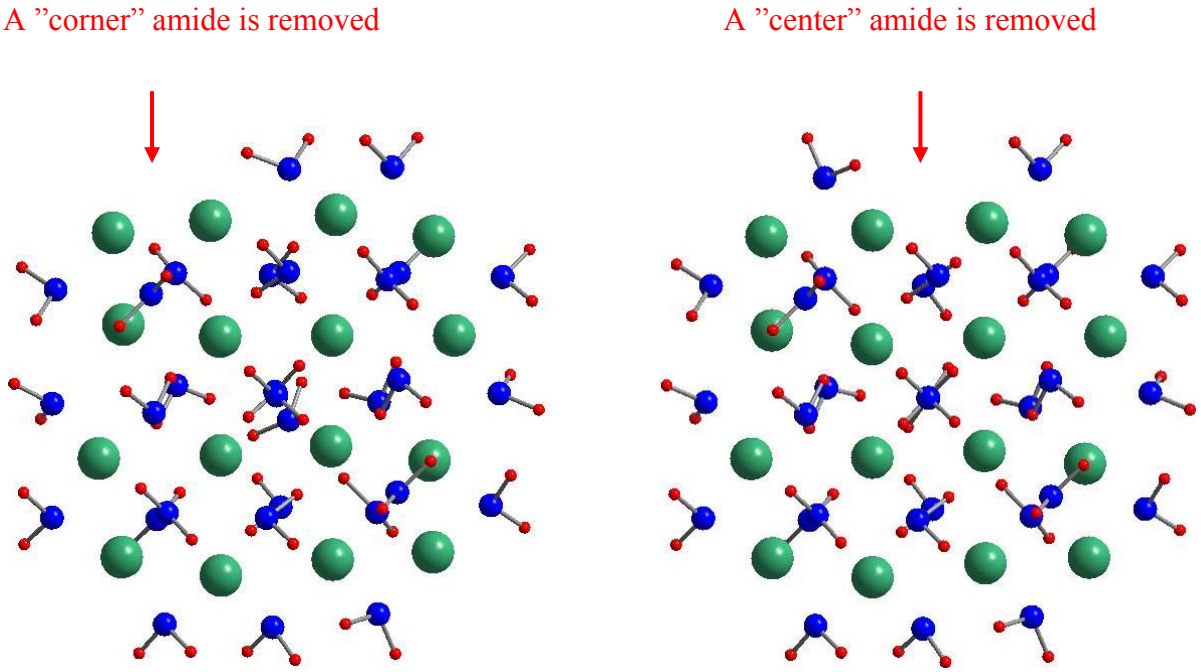

Figure 6.3: The figures show two different ways to remove an amide ion from the $Z16_{nst}$ cluster.

6.1.4 Removal of an ammonia molecule

The last molecule removed from the clusters was ammonia (NH_3). First it was removed from the $Z16_{nst}$ cluster in two different ways: (NH_3.1) Both a “center” amide plus an H atom from a “corner” amide was removed at the same time from the initial cluster and the new cluster was then relaxed; (NH_3.2) an H atom from a “corner” amide was first moved to the “center” amide, constructing one imide ion and one ammonia molecule. This cluster was then relaxed. Then the ammonia molecule was removed, and the cluster was again relaxed. The final relaxed clusters are shown in figure 6.4, and it is clear that the structural differences for the two clusters are very small. In addition, table 6.1 shows that the energy differences involved in the removal of ammonia in these two ways are very small (within 15 meV). This supports the hypothesis that the $Z16_{nst}$ cluster is a good and stable model, where the local minimas are independent of the reaction path. Moreover, this further indicates that the results obtained from calculations on the $Z16_{nst}$ cluster are reliable.

Ammonia was also removed from the other two clusters. For these clusters, ammonia was removed in one step, where both a “center” amide and an H atom from a neighboring “corner” amide was removed at the same time. The reason for why a “center” amide and an H atom from a “corner” amide was removed, and not the opposite, was that this procedure was

expected to be energetically favorable compared to other procedures based on the experience gained from the other decompositions performed on the clusters (see chapter 6.3.1 and 6.3.3).

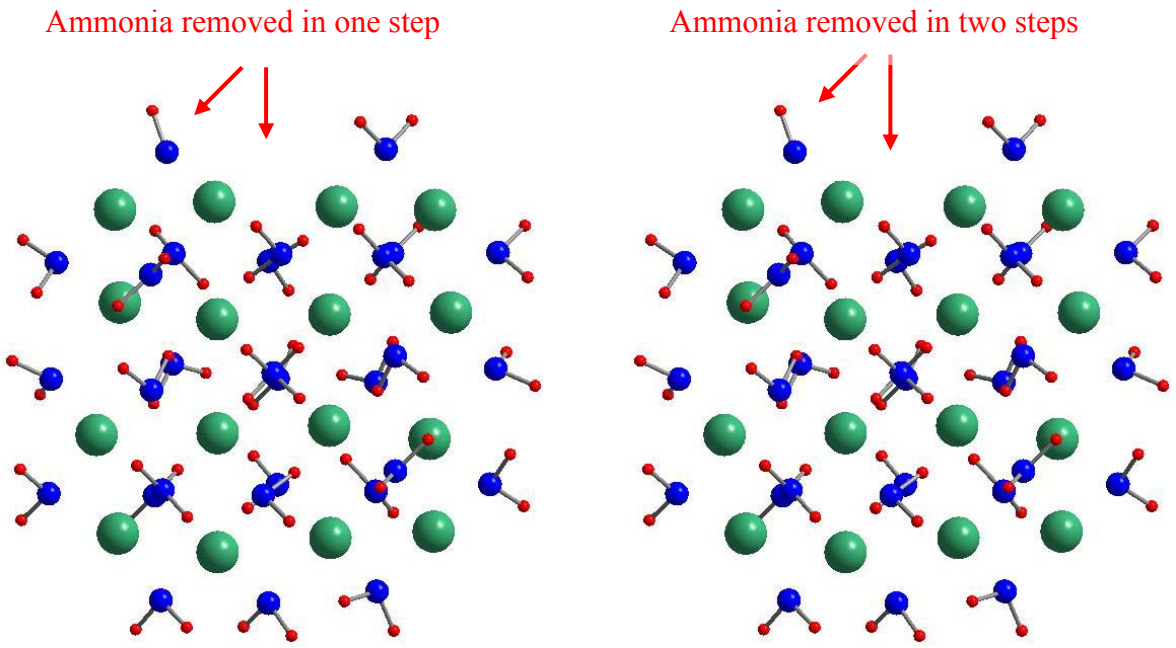

Figure 6.4: The figures shows the final cluster when ammonia has been removed from the $Z16_{nst}$ cluster in one or two steps, the NH_3.1 and the NH_3.2 clusters, respectively.

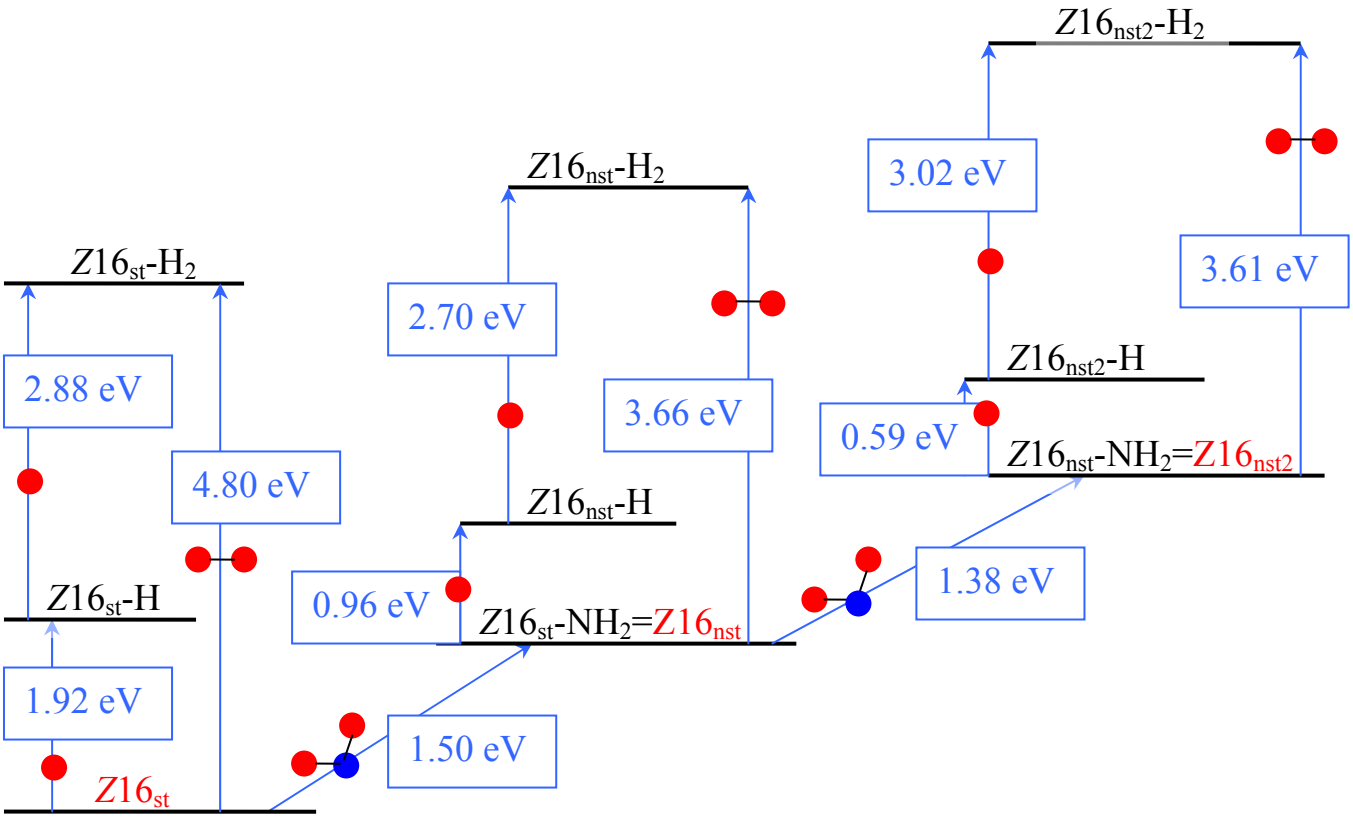

Figure 6.5: A schematic scheme over the lowest energies involved in the removal of H, H_2 and NH_2 from the $Z16_{st}$, the $Z16_{nst}$ and $Z16_{nst2}$ clusters (i.e. ΔE from equation 6.1).

	$Z16_{st}$	$Z16_{nst}$	$Z16_{nst2}$
Total energy (eV)	-559.13	-541.47	-525.96
ΔE (eV) after removal of			
H (corner)	1.92	0.96	0.59
H (center)	2.32	2.02	2.06
H_2.1	4.79	3.66	3.61
H_2.2	-	4.78	-
NH_2 (corner)	2.02	1.38	1.91
NH_2 (asym. corner)	1.49	-	-
NH_2 (center)	1.71	1.09	1.29
NH_2.3 (asym. center)	-	-0.65	-
NH_3.1	2.35	1.78	1.87
NH_3.2	-	1.79	-
NH_3.3	-	-0.06	-

Table 6.1: The energies (ΔE from eq. 6.1) involved in the removal of H, H_2, NH_2 and NH_3 from different surface positions of the $Z16_{st}$, $Z16_{nst}$ and the $Z16_{nst2}$ clusters.

The energy difference for the thermodynamic equilibrium states for the initial clusters and the new clusters plus the energy of NH_3 gas was within the range from 1.78 eV to 2.36 eV (see table 6.1). This means that it is much more difficult to remove pure H, i.e. monoatomic H or H_2, than H bonded to N, i.e. NH_2 and NH_3, from $Mg(NH_2)_2$.

6.1.5 Importance of the amide distribution

The decomposition of the clusters also gave some examples of how important the symmetry of the clusters (especially the distribution of the amides) is for the energy involved in the removal of different atoms/ions/molecules from them. From table 6.1 it is possible to see that the removal of the "corner" amide which contributes to the uneven distribution of the amides for the $Z16_{st}$ cluster (figure 5.7), and construct the $Z16_{nst}$ cluster (figure 5.8), cost less energy (smaller energy difference between the local minima) than removing any of the other "corner" amides of the $Z16_{st}$ cluster (a difference of approximately 0.5 eV). In fact, when the $Z16_{st}$ cluster is viewed from the $[11\bar{1}]$ direction (see figure 6.6), it becomes very clear that the amide ion contributing to the uneven distribution of amides in the $Z16_{st}$ cluster, really destroys the symmetry of the cluster. From this figure (from the (112) and the $(11\bar{2})$ planes) it is also possible to see that the $Z16_{st}$ clusters to some extent follow the natural branch like organization of the bulk structure (see figure 3.3 and 3.4). The main difference is that the Mg atoms which are found on the surface of the natural branches are covered by amides in the $Z16$ clusters, since this has proved to create more stable surfaces and clusters (see chapter 4 and 5).

Moreover, thorough investigations of the $Z16_{nst}$ cluster (also the $Z16_{st}$ and the $Z16_{nst2}$ clusters), showed that one of the "center" amides is more loosely bonded to Mg (longer Mg-amide bond) than the other amides (see figure 6.7). The removal of this amide, NH_2.3 in table 6.1, thus, cost much less energy than removing other "center" amides from the clusters. The total energy of the new cluster plus the energy of NH_2 gas is even lower than the total energy of the initial cluster (this is also the case if the same "center" amide plus a H atom is removed, NH_3.3 in table 6.1). This again shows some of the problems involved in cluster calculation,

especially on a compound with a big unit cell such as $Mg(NH_2)_2$, where a big cluster is needed to include all the symmetry properties of the unit cell. And since there, as already mentioned (see chapter 5.2), is a limit for the size of the cluster, both when it comes to time and memory consumption, this is a problem which is impossible to solve without more powerful computer facilities.

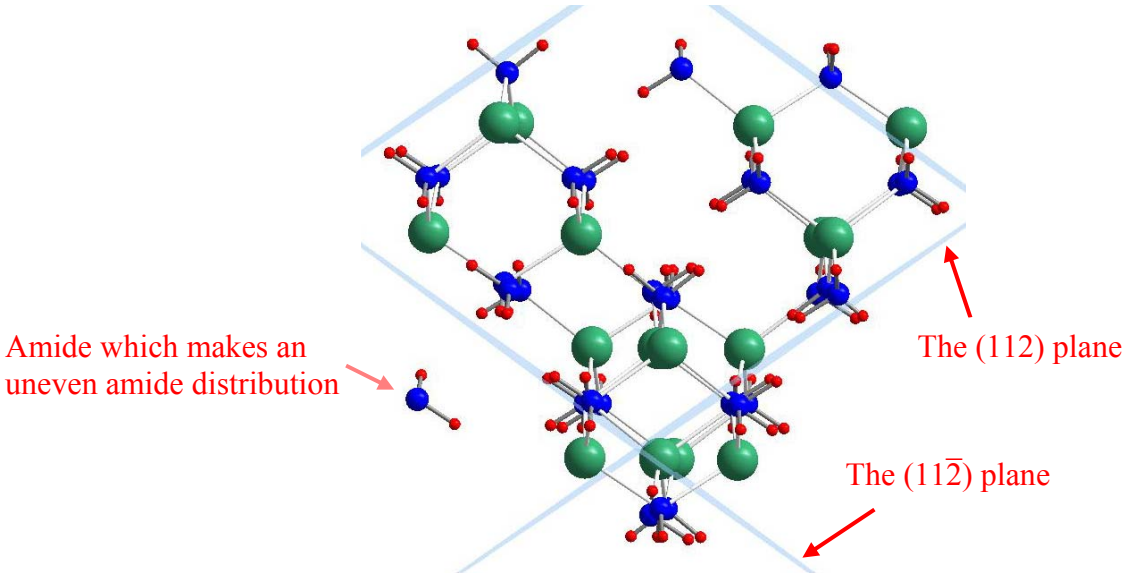

Figure 6.6: The $Z16_{st}$ cluster viewed from the [11$\bar{1}$] direction.

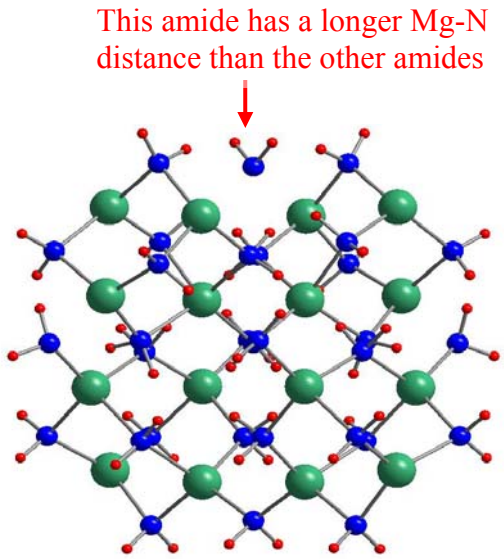

Figure 6.7: A figure of the $Z16_{nst}$ cluster viewed from the [010] direction where the Mg-N bonds also are drawn for an interatomic Mg-N distance between 1.4 and 2.8 Å.

6.2 Energy barriers

The energy barriers involved in the removal of H_2 and NH_3 molecules from $Mg(NH_2)_2$ were also calculated. Ideally we would have performed so called nudge elastic band (NEB) calculations to find these energy barriers. NEB is a method for finding saddle points and minimum energy paths between known reactants and products. The method works by relaxing a number of intermediate images along the reaction path. Each image finds the lowest energy possible, while maintaining equal spacing to neighboring images[41]. But because of some problems with getting NEB to run on *njord*, the super-computer used for the majority of the calculations during this thesis, a simplified method has been used. Here, only a linear reaction path without relaxation of the intermediate images was considered. This simplified model probably gives to high energy barriers, but the main tendencies of the reactions should be clear.

In figure 6.8 both the energy barrier for removal of H_2 and NH_3 from $Mg(NH_2)_2$ is shown. From this figure it is obvious that the activation energy needed to remove H_2 is much higher than the activation energy needed to remove NH_3 from $Mg(NH_2)_2$. This further supports the assumption that it is much harder to remove pure H, than H bonded to N, i.e. NH_2 and NH_3, from $Mg(NH_2)_2$.

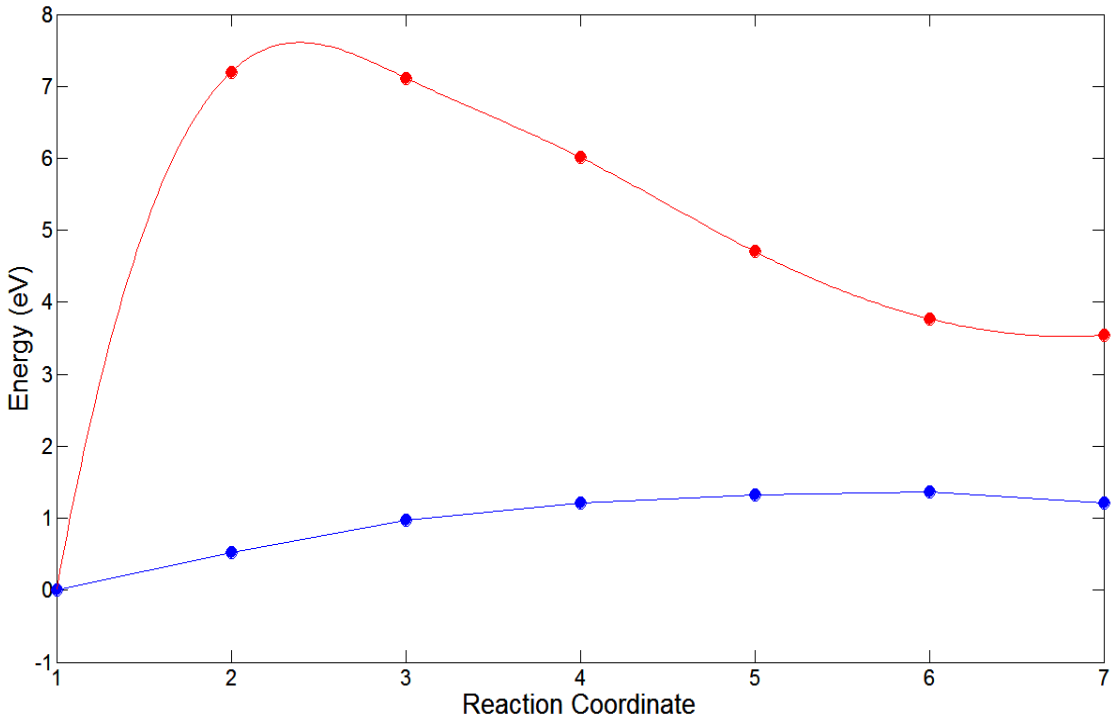

Figure 6.8: The energy barriers involved in the removal of H_2 and NH_3 from $Mg(NH_2)_2$. The red line is for H_2, while the blue line is for NH_3.

6.3 Discussion

The decomposition of the clusters has shown that it is much more difficult to remove pure H, i.e. monoatomic H or H_2, than H bonded to N, i.e. NH_2 and NH_3, from $Mg(NH_2)_2$. This was

further supported by the activation energies found in the removal of H_2 and NH_3 from the $Z16_{nst}$ cluster. Since most fuel cell systems require pure hydrogen to work, this is a major disadvantage with the $Mg(NH_2)_2$ system, and metal-N-H systems in general (see chapter 1.5) if they are to be used for hydrogen storage. However, some fuel cell systems can operate directly on ammonia, among them the solid oxide fuel cell (SOFC)[67]. In the SOFC, the heat required for the endothermic decomposition reactions of ammonia to produce H is supplied directly from the waste heat of the fuel cell, which at the same time helps cool the cell and thus extends its lifetime[67]. But the SOFC is a high temperature fuel cell, and not ideal for mobile applications. Due to this and the low reaction enthalpy found by Hu et al.[20] (see chapter 1.5.1), hydrogen storage in $Mg(NH_2)_2$ as a binary system is not recommendable. On the other hand, if $Mg(NH_2)_2$ is included in a ternary or multinary metal-N-H system, the thermodynamic properties is considerably improved compared to that of the binary $Mg(NH_2)_2$ system (see chapter 1.5.2 and 1.5.3). Furthermore, studies performed by Chen et al.[59] on the ternary $Mg(NH_2)_2$-2LiH system showed that the kinetics of reaction T-3 (see table 1.2), where only pure H is released, was greatly improved when the particle size of the reactants was decreased. This was important information since the decomposition of $Mg(NH_2)_2$-2LiH into ammonia is strongly temperature dependent[35]. At temperatures below approximately 160˚C the ammonia concentration in the system is quite low (mostly pure H is released), but the concentration is rapidly increasing for higher temperatures. An optimization of the thermodynamic and kinetic properties of the $Mg(NH_2)_2$-2LiH system may therefore lead to a hydrogen storage system which can be used in mobile applications in combination with low temperature fuel cells. This optimization probably includes manufacturing of $Mg(NH_2)_2$ and LiH with smaller perticle sizes. Another important part of the optimization is to find the ideal particle size of the hydrides in addition to the ultimate ratio between the particle size of the two hydrides. Here, cluster calculations can contribute to essential information. Since the capacity (both faster and larger memory) of the super-computers rapidly increases, it will soon be possible to do DFT calculations on larger clusters. Given that the particle size of the manufactured hydrides is decreasing (improved technology), means that it probably soon will be possible to do calculations on clusters which have the same size as the real nano-particles. So if future calculations are performed on a system consisting of both a $Mg(NH_2)_2$ and a LiH cluster, crucial information about this systems properties can be obtained, including information about the intersection between the two hydrides, their combined thermodynamical properties, how different ratios between the particle/cluster sizes of the two hydrides affects the thermodynamical properties and the activations energy involved in the removal of H_2 and NH_3 from the combined system and so on. So even if the cluster calculations performed during this thesis have no direct practical consequences, they can certainly serve as a good guideline for further cluster calculations, maybe on a combined system of $Mg(NH_2)_2$ and LiH clusters.

Chapter 7

7 Main conclusions and future recommendations

7.1 Main conclusions

Based on the studies performed during this thesis the following conclusions can be made:

- The cations in $Mg(NH_2)_2$ (i.e. Mg^{2+}) are tetrahedrally coordinated by the anions (i.e. NH_2^-) and the MgN_4 tetrahedra share all four corners with other MgN_4 tetrahedra, thus forming an open, three dimensional network. The unit cell is tetragonal and belongs to the space group $I4_1/acd$. Furthermore, the crystal structure was organized in cluster like branches, where the branches point in the $[1\bar{1}0]$ or the $[\bar{1}10]$ directions, and where each branch is separated from the other branches in the (112) and $(11\bar{2})$ orientations.
- $Mg(NH_2)_2$ is an insulator with a GGA band gap of approximately 3.1 eV. The N-H bonds are covalent, while the material is held together by ionic Mg-N bonds.
- The (110) surface has the lowest surface energy of the six investigated surfaces, and will therefore probably be the one most frequently found in a real crystal. The (012) and (112) surfaces were close in surface energy, and special symmetry properties and small structural changes during relaxation for the (112) surface also indicates that this surface will be frequently found in a real crystal.
- A combination of bulk, slab and cluster calculations in a plane wave code can be used to provide new and important insights of complex hydrides such as $Mg(NH_2)_2$. This type of combined calculations may be crucial for a successful and efficient search for new materials for hydrogen storage.
- The $Z16_{nst}$ cluster (figure 5.8) represents a good model for further cluster calculations on $Mg(NH_2)_2$ and the occupied states in the band gap of the $Z16_{nst}$ cluster are probably one of the reasons why complex hydrides with nano-particle structure have better kinetics than complex hydrides with larger particles (in addition to the increased surface area).
- A “corner” amide has stronger Mg-N bonds than a “center” amide, since the “corner” Mg atom has more dangling bonds than the “center” Mg atom, leading to a stronger Mg-N bond on the “corner”. This strong Mg-N bond leads to a weakened N-H bond within the amide, meaning that it is easier to remove an H atom from a “corner” amide than an H atom from a “center” amide.
- The decomposition of the clusters has shown that it is much more difficult to remove pure H, i.e. monoatomic H or H_2, than H bonded to N, i.e. NH_2 and NH_3, from $Mg(NH_2)_2$.
- The activation energy involved in the removal of NH_3 is much lower than the activation energy involved in the removal of H. This confirms a general feature of metal-nitrogen complex hydrides, which is a substantial problem if these materials are to be used for hydrogen storage in mobile applications, since all known low

temperature fuel cells are poisoned by nitrogen. Another problem is of course the loss of nitrogen, which would change the chemical composition of the material and consequently degrade the cycling hydrogen storage capacity.

7.2 Recommendations

Based on the work performed during this thesis we have the following suggestions for further calculations:

- The Norwegian super-computers are regularly upgraded (faster and more powerful). This means that it in the near future probably will be possible to do calculations on $Mg(NH_2)_2$ slabs consisting of more than 3 layers. This would be of special interest for the (112) slab since the crystal structure of $Mg(NH_2)_2$ is organized in branches of two and two layers of atoms in the (112) orientation. By using a 4, 6, … layered (112) slab, none of these two layered branches have to be destroyed during the construction, which may result in a lowered surface energy for the (112) surface.
- It would be interesting to perform NEB calculations on the $Z16_{nst}$ cluster, because then more reliable results for the activation energy involved in the removal of H and NH_3 can be obtained.
- Perform "branch" calculations on $Mg(NH_2)_2$ and other materials with a branch like structure. "Branch" calculations means that vacuum layers are inserted in two directions of the unit cell, while the structure is continuous in the third direction. Several surface facets can then be investigated, while the periodicity of the material is still taken into account. Moreover, it is much easier to construct the branches than the clusters from already known stable surfaces, since then only four surfaces must be taken into account, compared to at least six for the clusters.
- Continue with cluster calculations in combination with bulk, slab and maybe even "branch" calculations in a plane wave code. This combination would certainly help increase the understanding of complex hydrides and support the development of new complex hydrides for hydrogen storage. It should be mentioned here that for the time being cluster calculations are probably best suited for materials where the unit cell is not too large (up to approximately 200 atoms), since it will then be easier to make a cluster where all the symmetry properties of the material are included, and which at the same time is small enough to be run on today's super-computers.
- The technology involved in the manufacturing of hydrides is rapidly improving (hydrides with smaller and smaller nano-particles can be made). At the same time the super-computers quickly improves (both faster and larger memory), meaning that cluster calculations involving larger and larger clusters can be performed. As a consequence of this, calculations on clusters which have the same size as the real nano-particles can probably soon be performed. These calculations should be done, since they will contribute to important information in the search for new materials for hydrogen storage.
- The most promising metal-N-H systems for hydrogen storage are ternary or multinary. With improved super-computers, calculations on systems consisting of two or more clusters of two or more different hydrides should be performed, since this, among other things, can give valuable information about the interface between the different hydrides and how different ratios between the particle sizes of the different hydrides influence the thermodynamics and kinetics of the systems.

Appendix A

Abbreviations

The following table gives an overview over the most important abbreviations used during this thesis.

Abbreviation	Actual meaning
A green sphere	A magnesium atom
A blue sphere	A nitrogen atom
A red sphere	A hydrogen atom
DFT	Density functional theory
GGA	General gradient approximation
LDA	Local density approximation
PBE	Perdew-Burke- Emzerhof
PAW	Projector augmented wave
LCAO	Linear combination of atomic orbitals
LAPWs	Linear augmented plane waves
PWs	Plane waves
VASP	Vienna ab-initio simulation package
ADF	Amsterdam density functional
DOS	Density of states
Mg	Magnesium
N	Nitrogen
H	Hydrogen
A “good” slab	A slab that experience small structure and energy changes during ionic relaxation
A “bad” slab	A slab that experience substansial structure and energy changes during ionic relaxation
“Bulk” structure	The region of the structure inside a slab or cluster that are not on the surface
A *ZX*N cluster	A cluster consisting of *X* formula units of $Mg(NH_2)_2$ having nitrogen as central atom
The *Z*16$_{st}$ cluster	The stoiciometric cluster consisting of 16 formula units of $Mg(NH_2)_2$ with N as central atom
The *Z*16$_{nst}$ cluster	Same cluster as the *Z*16$_{st}$ cluster, but with one less amide ion, giving a non stoiciometric cluster (formal charge +1)
The *Z*16$_{nst2}$ cluster	Same cluster as the *Z*16$_{st}$ cluster, but with two less amide ions, giving a non stoiciometric cluster (formal charge +2)

Table A.1: An overview over the most important abbreviations used during this thesis.

Bibliography

[1] P. Chen, Z. Xiong, J. Luo, J. Lin and K. L. Tan, Nature **420**, 302 (2002).

[2] Intergovernmental Panel On Climate Change, Synthesis Report. http://www.ipcc.ch/ipccreports/ar4-syr.htm.

[3] R.A.Rohde, Global Warming Art. http://www.globalwarmingart.com/wiki/.

[4] World Data Centre for Greenhouse gases, http://gaw.kishou.go.jp/wdcgg/gas.html.

[5] A. Neftel, E. Moor, H. Oeschger and B. Stauffer, Nature **315**, 45 (1985).

[6] P. N. Pearson and M. R. Palmer, Nature **406**, 695 (2000).

[7] R. Griessen, Science and Technology of Hydrogen in Metals, Lecture notes in a University course, Vrije Universiteit. http://www.nat.vu.nl/CondMat/griessen/

[8] Australien Academy of science, Harnessing direct solar energy - a progress report. http://www.science.org.au/nova/005/005glo.htm.

[9] National Renewable Energy Laboratory, Solar Energy Basics. http://www.nrel.gov/learning/re_solar.html.

[10] J. H. N. van Vucht, Philips Research Reports **18**, 21 (1963).

[11] Energy Information Administration, Official Energy Statistics from the U.S. Government. http://www.eia.doe.gov/kids/infocardnew.html#ELECTRICITY.

[12] A. Züttel, in H2NET SEMINAR (2004).

[13] A. Züttel, Mater. Today **September**, 24 (2003).

[14] A. Råheim, Hydrogen – fremtidens drivstoff? Utfordringer og teknologiske perspektiver. www.ntva.no/seminarer/manus/raaheim-050406%20NTVA.pdf.

[15] A. Züttel, Naturwissenschaften **91**, 157 (2004).

[16] F. Schuth, B. Bogdanovic and M. Felderhoff, Chem. Commun., 2249 (2004).

[17] A. Takasaki, Y. Furuya and Y. Taneda, Mater. Sci. Eng. A **239-240**, 265 (1997).

[18] B. Bogdanović, R. A. Brand, A. Marjanovic, M. Schwickardi and J. Tölle, J. Alloys Compd. **302**, 36 (2000).

[19] T. Ichikawa, N. Hanada, S. Isobe, H. Y. Leng and H. Fujii, J. Phys. Chem. B **108**, 7887 (2004).

[20] J. J. Hu, G. T. Wu, Y. F. Liu, Z. T. Xiong, P. Chen, K. Murata, K. Sakata and G. Wolf, J. Phys. Chem. B **110**, 14688 (2006).

[21] J. J. Hu, Z. T. Xiong, G. T. Wu, P. Chen, K. Murata and K. Sakata, J. Power Sources **159**, 120 (2006).

[22] P. Chen, Z. T. Xiong, G. T. Wu, Y. F. Liu, J. J. Hu and W. F. Luo, Scr. Mater. **56**, 817 (2007).

[23] F. E. Pinkerton, G. P. Meisner, M. S. Meyer, M. P. Balogh and M. D. Kundrat, J. Phys. Chem. B **109**, 6 (2005).

[24] Y. F. Liu, J. J. Hu, Z. T. Xiong, G. T. Wu, P. Chen, K. Murata and K. Sakata, J. Alloys Compd. **432**, 298 (2007).

[25] P. Chen, Z. T. Xiong, J. Z. Luo, J. Y. Lin and K. L. Tan, J. Phys. Chem. B **107**, 10967 (2003).

[26] Z. Xiong, G. Wu, J. Hu and P. Chen, Adv. Mater. **16**, 1522 (2004).

[27] H. Leng, T. Ichikawa and H. Fujii, J. Phys. Chem. B **110**, 12964 (2006).

[28] W. Luo, J. Alloys Compd. **381**, 284 (2004).

[29] T. Ichikawa, H. Y. Leng, S. Isobe, N. Hanada and H. Fujii, J. Power Sources **159**, 126 (2006).

[30] Z. T. Xiong, J. J. Hu, G. T. Wu, Y. F. Liu and P. Chen, Catal. Today **120**, 287 (2007).

[31] Y. Liu, J. Hu, G. Wu, Z. Xiong and P. Chen, J. Phys. Chem. C **111**, 19161 (2007).

[32] Z. T. Xiong, G. T. Wu, H. J. Hu and P. Chen, Adv. Mater. **16**, 1522 (2004).

[33] E. R. Luo, J. Alloys Compd. **404** (2005).

[34] H. Y. Leng, T. Ichikawa, S. Hino, N. Hanada, S. Isobe and H. Fujii, J. Phys. Chem. B **108**, 8763 (2004).

[35] Y. F. Liu, J. J. Hu, G. T. Wu, Z. T. Xiong and P. Chen, J. Phys. Chem. C **112**, 1293 (2008).

[36] H. Jacobs, Z. Anorg. Allg. Chem. **382**, 97 (1971).

[37] M. H. Sørby, Y. Nakamura, H. W. Brinks, T. Ichikawa, S. Hino, H. Fujii and B. C. Hauback, J. Alloys Compd. **428**, 297 (2006).

[38] O. I. Velikokhatnyi and P. N. Kumta, Mater. Sci. Eng. B **140**, 114 (2007).

[39] J. Hafner, Comput. Phys. Comm. **177**, 6 (2007).

[40] G. Karlberg, Catalytic Water Production from First-Principles Calculations, PhD Thesis, Chalmers University of Technology, (2005).

[41] G. Kresse and J. Furthmüller VASP the GUIDE. http://cms.mpi.univie.ac.at/vasp/vasp/.

[42] Scientific Computing & Modeling, ADF - the Power Tool for Quantum Chemists. http://www.scm.com.

[43] P. Hohenberg and W. Kohn, Phys. Rev. B **136**, B864 (1964).

[44] W. Kohn and L. J. Sham, Phys. Rev. **140**, 1133 (1965).

[45] D. J. Griffiths, Introduction to Quantum Mechanics, 2nd edition, (2005).

[46] P. Atkins and R. Friedman, Molecular quantum mechanics, 4th edition, (2005).

[47] C. Broedersz, The Mg-Ti-Ni-H system studied by hydrogenography experiments and density functional calculations, Master Thesis, Vrije Universiteit, Amterdam.

[48] J. P. Perdew, Phys. Rev. Lett. **55**, 1665 (1985).

[49] J. Hafner, Acta Mater. **48**, 71 (2000).

[50] P. Molin, Solid State Storage of Hydrogen in Magnesium Alanate -a Density Functional Study, Master thesis, University of Oslo.

[51] P. Blöchl, Phys. Rev. B **50**, 17953 (1994).

[52] G. Kresse and J. Furthmuller, Comput. Mater. Sci. **6**, 15 (1996).

[53] G. Kresse and D. Joubert, Phys. Rev. B **59**, 1758 (1999).

[54] J. P. Perdew, M. Emzerhof and K. Burke, J. Chem. Phys. **105**, 9982 (1996).

[55] J. P. Perdew, J. A. Chevary, S. H. Vosko, K. A. Jackson, M. R. Pederson, D. J. Singh and C. Fiolhais, Phys. Rev. B **46**, 6671 (1992).

[56] G. T. Velde, F. M. Bickelhaupt, E. J. Baerends, C. F. Guerra, S. J. A. Van Gisbergen, J. G. Snijders and T. Ziegler, J. Comput. Chem. **22**, 931 (2001).

[57] NOTUR - The norwegian metacenter for computational science. http://www.notur.no/.

[58] O. M. Løvvik, S. M. Opalka, H. W. Brinks and B. C. Hauback, Phys. Rev. B **69** (2004).

[59] P. Chen, Z. T. Xiong, L. F. Yang, G. T. Wu and W. F. Luo, J. Phys. Chem. B **110**, 14221 (2006).

[60] V. Fiorentini and M. Methfessel, J. Phys.-Condens. Mat. **8**, 6525 (1996).

[61] J. C. Boettger, J. R. Smith, U. Birkenheuer, N. Rosch, S. B. Trickey, J. R. Sabin and S. P. Apell, J. Phys.-Condens. Mat. **10**, 893 (1998).

[62] J. C. Boettger, Phys. Rev. B **49**, 16798 (1994).

[63] O. M. Løvvik, J. Alloys Compd. **356**, 178 (2003).

[64] T. J. Frankcombe and O. M. Løvvik, J. Phys. Chem. B **110**, 622 (2006).

[65] A. Marashdeh, R. A. Olsen, O. M. Løvvik and G. J. Kroes, Chem. Phys. Lett. **426**, 180 (2006).

[66] A. Marashdeh, R. A. Olsen, O. M. Løvvik and G. J. Kroes, J. Phys. Chem. C **111**, 8206 (2007).

[67] C. H. Christensen, T. Johannessen, R. Z. Sørensen and J. K. Nørskov, Catal. Today **111**, 140 (2006).